GENERATION OF INTENSE HIGH HARMONICS:

i) TO TEST AND IMPROVE RESOLUTION OF ACCUMULATIVE X-RAY STREAK

CAMERA

ii) TO STUDY THE EFFECTS OF CARRIER ENVELOPE PHASE ON XUV SUPER

CONTINUUM GENERATION BY POLARIZATION GATING

by

MAHENDRA MAN SHAKYA

B.Sc.,Tribhuvan University,Nepal,1988
M.Sc.,Tribhuvan University,Nepal,1991
MS, Kansas State University, 2003

AN ABSTRACT OF A DISSERTATION

submitted in partial fulfillment of the requirements for the degree

DOCTOR OF PHILOSOPHY

Department of Physics
College of Arts and Sciences

KANSAS STATE UNIVERSITY
Manhattan, Kansas

2007

Abstract

The first part of this thesis describes our novel design, test, and application of our X-ray streak camera to the pulse duration measurement of soft X-rays. We demonstrated a significant improvement in the resolution of the x-ray streak camera by reducing the electron beam size in the deflection plates. This was accomplished by adding a slit in front of the focusing lens and the deflection plates. The temporal resolution reached 280 fs when the slit width was 5 μm. The camera was operated in an accumulative mode and tested by using a 25 fs laser with 2 kHz repetition rate and 1-2% RMS pulse energy stability. We conclude that deflection aberrations, which limit the resolution of the camera, can be appreciably reduced by eliminating the wide-angle electrons.

We also employed the same streak camera to demonstrate that it is capable of measuring the pulse duration of X-rays. We measured the pulse duration of X-rays emitted from Ni-like Ag and Cd grazing-incidence laser to be ~5ps. The measured value agrees with the prediction made by the model and the measurement made by changing the delay as a function of the pulse duration. The streak camera was also tested with various sources of X-ray such as high harmonics generation of soft x-rays from an argon atom using a high power Ti:sapphire laser source of KLS. The result of the measurement manifests its capability for serving as a detector in the study of ultrafast dynamics in the field of physics, chemistry, biology and medical sciences.

The second part of this thesis describes our design of a spectrometer to study the effect of the Carrier envelope (CE) phase on polarization gated extreme-ultraviolet (XUV) super-continuum generation. Because the challenge of making single shot experiment possible is to generate a sufficient number of photons, our setup has been built to allow generation of high order harmonics at the maximum phase matched pressure. This is the first time to our knowledge that phase matching in the polarization gating process has been studied so far. We measured the maximum phase matching pressure to be ~ 55 Torr which is the pressure above which quadratic increase in intensity of the high harmonics spectrum ceases to appear. At this pressure the number of photons per laser shot was 10^4 which is sufficient for measuring the single shot XUV spectrum in the range 34 to 45 eV. The spectral profile was a super-continuum for some shots

and discrete high harmonics for other shots. It is believed that the shot to shot variation of the spectra is due to the changes of the carrier envelope phase of the few-cycle laser pulses used for the polarization gating.

An improved CE phase stabilization system in KLS further eliminated the statistical noise in our observation by allowing us to integrate data over several laser cycles for each CE phase value. The effect of CE phase on a polarization gated XUV spectrum was tested by changing the CE phase with two different methods. In the first method, the CE phase was changed by changing the thickness of fused silica plates on the beam path, and the result shows the shift in the spectral peak of the XUV when the gate width approached less than one optical cycle. As gate width was made less than half the optical cycle, the spectrum was observed with continuum harmonics separated by π radians. We believe that the presence of continuum and discrete harmonics spectra in the observation is due to single and double attosecond pulses generated in the polarization gating.

In the second method the carrier-envelope phase of pulses from a grating-based chirped pulse amplification laser was varied smoothly to cover a 2π range by controlling the grating separation. The phase is measured simultaneously by an *f*-to-*2f* setup and by the variation of XUV spectra from polarization gated high harmonic generation. A very good similarity between the effect of single and double slits in Yong's experiment and that of CE phase on the XUV spectrum in the polarization gating experiment has been found, giving better agreement with the theory.

The effect of optical properties such as the Gouy phase shift on the polarization gated spectrum has also been studied in the course of investigating the best experimental optimizations to generate the most CE phase sensitive XUV spectrum with less statistical noise. This is the first time to our knowledge experimental study of the effect of the Gouy phase shift on a polarization gated XUV spectrum has been made.

GENERATION OF INTENSE HIGH HARMONICS:

i) TO TEST AND IMPROVE RESOLUTION OF ACCUMULATIVE X-RAY STREAK

CAMERA

ii) TO STUDY THE EFFECTS OF CARRIER ENVELOPE PHASE ON XUV SUPER

CONTINUUM GENERATION BY POLARIZATION GATING

by

MAHENDRA MAN SHAKYA

B.Sc.,Tribhuvan University,Nepal,1988
M.Sc.,Tribhuvan University,Nepal,1991
MS, Kansas State University, 2003

A DISSERTATION

submitted in partial fulfillment of the requirements for the degree

DOCTOR OF PHILOSOPHY

Department of Physics
College of Arts And Sciences

KANSAS STATE UNIVERSITY
Manhattan, Kansas

2007

Approved by:

Major Professor
Prof. Zenghu Chang

Copyright

MAHENDRA MAN SHAKYA

2007

Abstract

The first part of this thesis describes our novel design, test, and application of our X-ray streak camera to the pulse duration measurement of soft X-rays. We demonstrated a significant improvement in the resolution of the x-ray streak camera by reducing the electron beam size in the deflection plates. This was accomplished by adding a slit in front of the focusing lens and the deflection plates. The temporal resolution reached 280 fs when the slit width was 5 μm. The camera was operated in an accumulative mode and tested by using a 25 fs laser with 2 kHz repetition rate and 1-2% RMS pulse energy stability. We conclude that deflection aberrations, which limit the resolution of the camera, can be appreciably reduced by eliminating the wide-angle electrons.

We also employed the same streak camera to demonstrate that it is capable of measuring the pulse duration of X-rays. We measured the pulse duration of X-rays emitted from Ni-like Ag and Cd grazing-incidence laser to be ~5ps. The measured value agrees with the prediction made by the model and the measurement made by changing the delay as a function of the pulse duration. The streak camera was also tested with various sources of X-ray such as high harmonics generation of soft x-rays from an argon atom using a high power Ti:sapphire laser source of KLS. The result of the measurement manifests its capability for serving as a detector in the study of ultrafast dynamics in the field of physics, chemistry, biology and medical sciences.

The second part of this thesis describes our design of a spectrometer to study the effect of the Carrier envelope (CE) phase on polarization gated extreme-ultraviolet (XUV) supercontinuum generation. Because the challenge of making single shot experiment possible is to generate a sufficient number of photons, our setup has been built to allow generation of high order harmonics at the maximum phase matched pressure. This is the first time to our knowledge that phase matching in the polarization gating process has been studied so far. We measured the maximum phase matching pressure to be ~ 55 Torr which is the pressure above which quadratic increase in intensity of the high harmonics spectrum ceases to appear. At this pressure the number of photons per laser shot was 10^4 which is sufficient for measuring the single shot XUV spectrum in the range 34 to 45 eV. The spectral profile was a supercontinuum for some shots and

discrete high harmonics for other shots. It is believed that the shot to shot variation of the spectra is due to the changes of the carrier envelope phase of the few-cycle laser pulses used for the polarization gating.

An improved CE phase stabilization system in KLS further eliminated the statistical noise in our observation by allowing us to integrate data over several laser cycles for each CE phase value. The effect of CE phase on a polarization gated XUV spectrum was tested by changing the CE phase with two different methods. In the first method, the CE phase was changed by changing the thickness of fused silica plates on the beam path, and the result shows the shift in the spectral peak of the XUV when the gate width approached less than one optical cycle. As gate width was made less than half the optical cycle, the spectrum was observed with continuum harmonics separated by π radians. We believe that the presence of continuum and discrete harmonics spectra in the observation is due to single and double attosecond pulses generated in the polarization gating.

In the second method the carrier-envelope phase of pulses from a grating-based chirped pulse amplification laser was varied smoothly to cover a 2π range by controlling the grating separation. The phase is measured simultaneously by an *f*-to-*2f* setup and by the variation of XUV spectra from polarization gated high harmonic generation. A very good similarity between the effect of single and double slits in Yong's experiment and that of CE phase on the XUV spectrum in the polarization gating experiment has been found, giving better agreement with the theory.

The effect of optical properties such as the Gouy phase shift on the polarization gated spectrum has also been studied in the course of investigating the best experimental optimizations to generate the most CE phase sensitive XUV spectrum with less statistical noise. This is the first time to our knowledge experimental study of the effect of the Gouy phase shift on a polarization gated XUV spectrum has been made.

Table of Contents

List of Figures

Acknowledgements

I would like to express my gratitude to all those who gave me the possibility to complete this thesis.

I am deeply indebted to my supervisor Prof. Dr. Zenghu Chang whose help, stimulating suggestions and encouragement helped me in all the time of research for and writing of this thesis. I am deeply grateful for his constructive comments, and for his important support throughout this work. I doubt that I will ever be able to convey my appreciation fully, but I owe him my eternal gratitude.

I am deeply grateful to Former Director of James R. Macdonald Laboratory (JRML) and distinguished professor Patrick Richard for his kind suggestions, help and support in my time of need. I also would like to thank him for giving his time to serve as a member of my PhD committee.

I am grateful to Prof. Brett D. Depaola, for serving as a supervisory committee member in spite of his busy schedule. I would also like to thank Prof. Depaola for his support and help to open new door for my carrier

I would like to thank Prof. Shuttng Lei and external chair Prof. Medhat M. Morcos for giving time to serve as a supervisory committee member.

I would like to express my thanks to the personnel of JRML and Machine shop for their support and willingness to help in every possible in a friendly environment. I would like to express my special thanks to Mike Well for his help to troubleshoot all kinds of problem in the vacuum system. I should not forget tremendous help of Al Rankin anytime I needed without whom this project would have been almost impossible. By serving as a designer, providing innovative idea, helping machine the parts and countless free help, he made me possible to survive against the difficulty.

I would also specially like to acknowledge Vince Needham for his help with computers. What surprised me the most was his tireless willingness and skill to tackle any kinds of problem in computers.

In the lab I had the opportunity to work closely with Steve Gilbertson, Chris Nakamura and Dr. Hiroki. I am grateful to them for supporting and encouraging me by sharing equal amount of pain during the time of difficulty and joy during the time of progress which provided a very friendly and at the same time productive work environment. I am grateful to Eric Moon and Dr. Chenquan Li for their work in the lab and for tolerating the seemingly endless rounds of data taking. I would also like to thank both of them for

staying awake all night and struggling hard during our beam time schedule to stabilize carrier envelope (CE) phase of the laser system. I also like to thank all our group members: Jason Tackett, Dr. Ximao, Sabih Khan, Wang He, Yi Wu and Michael Chini for being very helpful at various points in my work.

I would like to give special thanks to Carol Regehr who has always willing to read my manuscripts and thesis and correct my English.

To my family especially my parents, I owe and will always owe a great debt for giving me whatever good quality I have. Their support and their trust on me regardless of the choice I make never let my feeling lonely with frustration. I owe my loving thanks to my wife Pratibha Shakya. Without her patience, encouragement and understanding it would have been impossible for me to finish this work.

CHAPTER 1 - Introduction

A discovery of a technique for the generation of very monochromatic radiation [1] so called laser has become an indispensable tool with enormous applications in many fields of research. Ever since, the rapid progress toward the technology of a generating the laser with shorter and shorter pulse duration can now deliver intensities up to $\sim 10^{15}$ W/cm^2 at the repetition rate 1 kHz from the table-top laser system. Practically, there are two main reasons for the investigation of a technique to generate a pulse as short as possible. The quest for better ways to understand fast physical, biological and chemical processes is the present area of interest in physics. For event-by-event mapping and monitoring of those time dependent phenomena, there is no other promisingly precise method ever developed than the time-resolved experiment. However, the degree of precision of measurement depends on how fast interaction inducing laser can be exposed to the sample under study. In other words, the shorter the pulse duration, the faster the interaction and the more precise the measurement will be. For precise measurement of fast processes, not only do we require the fastest interacting tool; a detector with faster and faster reading capability becomes equally necessary too. If, for example, the flapping wings of a hummingbird are to be recorded, a camera with a shutter speed faster than the speed of the wing is essential. The image to be studied otherwise will be blurred. Therefore only a detector with speed faster than the fastest process can provide accurate information of that event. Time resolved X-ray diffraction has been a successful method in studying laser-induced disordering of Pb(110) [2] understanding X-ray diffraction from laser-induced coherent acoustic phonons in InSb crystal [3] and studying the structural transition in biology [4]. Since, resolution of the detector available was limited to the picosecond scale, the study of the process taking place in the sub-picosecond remains only the dream. Although, cross-correlation and auto-correlation techniques are capable of measuring extremely fast events at the femtosecond scale, both of them have their limitations. The former require a material with extremely efficient nonlinear effect to use short wavelength. As material of this nature is hard to find, measurement of fast processes with cross-correlation is less practical. Cross-correlation has been ruled out from its application as it is less easy to use, provides only one dimensional information and is not applicable to X-ray pulses. If an x-ray streak camera with the better resolution can be made, all the discrepancies

mentioned above would be eliminated. Because of its necessity for study of the fast processes, the requirement for progress in building a streak camera with better resolution has been felt since its advent in 1975.With the demonstration of sub-picoseconds (800fs) streak camera [5], much progress on experiments using an x-ray streak camera has been reported. The most exciting result first reported from the time-resolved x-ray diffraction method by using an x-ray streak camera is the observation of temporal oscillations in x-ray intensity propagated by a coherently oscillating lattice. Seven years latter, another breakthrough in streak camera design [6] was made by demonstrating 560fs in accumulative mode. The ramp pulse of the deflection plate and the rise time of the photoconductive switch were appreciably improved. Timing jitter, which is the major factor for image broadening, was reduced to 50 fs. This breakthrough in resolution added further encouragement to strive for building a streak camera with better resolution. However, the study of phonons with the time resolved x-ray diffraction method requires a streak camera with at least 100fs resolution. The objective is to study the temporal evolution of the phonon through a pump and probe scheme. In this scheme pump and probe beam are generated by using a Mach-Zehnder interferometer. A broad x-ray probe beam provides structural information of the sample. While relatively short laser pulse used as a pump pulse help to trigger the ultra fast interaction. The delay between the pump and probe beam provides temporal evolution of the optical phonon. However, the present capability of the x-ray streak camera does not permit progress in understanding these ultrafast processes taking place in the solid. But the question is why there is no streak camera with the resolution better than 100 fs is found. In this work, to answer that query, I shall present in detail the study of the factor that affect the resolution of the x-ray streak camera, my design to improve the resolution, the results of the test.

Another reason to investigate the technique to generate a pulse as short as possible is to increase the peak power of the lasers without requiring an increase in the pulse energy. Progress in current laser technology can deliver a pulse as short as 5 fs and intensity as high as $\sim 10^{15}$ W/cm^2. Dilute gas media exposed to such high intensities is partially ionized subjecting to the requirement to cope with the effect of plasma medium. For intensities ranging 10^{14} W/cm^2 and 10^{15} W/cm^2, referred to as the non-relativistic range, laser-matter interaction can safely be treated as a single atom exposed only to an oscillating electric field. In that case, the contributions due to the magnetic field become negligibly smaller. Because, the ionization of an atom through photo-electric effect, under the context mentioned above, requires photon energy

many times higher than single photon energy, process is widely known as a multiphoton process. One well known example of this process is high order harmonic generation. Typically, the harmonics radiation appears with a plateau of same intensity separated by twice the driving laser frequency followed by rapidly dropping intensity so called cut-off intensity. Underlying physics of this process can be explained in a semi-classical three steps model [7]. As an electron is freed from the ionized atom through interaction with the high intensity laser, it falls under the influence of the oscillating electric field of the driving laser. The electron oscillating in unison with the laser oscillation raises the kinetic energy many times higher than original electron binding energy. As the laser electric field reverses, it drives the electron back to the parent ion, which re-collides with it. This process of re-collision and recombination results in the emission of a high energy photon. As all the atoms are exposed to the same highly coherent laser field, emission of radiation known as high harmonic radiation also takes place coherently. Such emission of radiation occurs every half cycle of the driving laser field, producing a train of attosecond pulses in the time domain. Since its discovery in 1987, it has been realized as an extremely useful and unique light source, leading to application in many fields of technology such as spectroscopy, holography, photography etc. The recent capability of routinely delivering ultra short laser pulses, as short as ~5 fs, has drawn attention of experimentalists toward HHG extensively. On one hand, as pulse duration becomes shorter and shorter, it becomes a useful source in connection with higher intensity and faster potency of interaction with the matter. On the other hand, it could be a source of problems unless the different positions of the electric field relative to its envelope are accurately known. For such a short pulse (~5 fs), so called few cycle pulses, the temporal variation of the electric field depends on whether or not peak of the electric field coincides with the peak of its envelope. The relative position of the peak of the carrier wave electric field with respect to peak of the envelope is called carrier-envelope (CE) offset phase or absolute phase. Because of pulse-to-pulse slip in CE phase, the effect of those pulses causing nonlinear processes also varies with time. An extremely non-linear process, such as high order harmonics generation by those pulses, is highly sensitive to the change in CE phase. Generation of many orders of harmonics is in fact caused by the interference of emission caused by the collision of many returning electrons with the parent ions. When the pulse is made shorter than one optical cycle, emission of a high order harmonic can take place either by one electron-ion emission or by two electron-ion emission depending on the CE phase of the pulses. The emission

by two electron-ion re-collision corresponds to interference due to two slits in the spectral domain as in Young's double slit experiment. The result of that interference gives rise to many harmonics orders. On the contrary, if emission takes place by the re-collision of only one returning electron, it will generate a single broad spectrum resembling the single slit diffraction in the spectral domain. This broad band spectrum due to single electron return corresponds to a single attosecond pulse in the time domain. Now it is clear that a key to produce an isolated attosecond XUV pulse is to control the CE phase of the few cycle pulse in such a way that only one electron return is made possible. Moreover, this correlation between CE phase and high order harmonic generation (HHG) could be a potentially valuable means for measuring absolute CE phase if the effect of shot-to-shot change in CE phase on HHG spectra were measured.

Previously, CE phase has been measured by f-to-2f interferometers and phase- meter based above-threshold ionization (ATI) [8, 9]. Although f-2f interferometers have been widely used to stabilize and evaluate the CE phase stability of the laser system, the measured results are in-loop measurement and are subject to the power fluctuation of the laser pulse. It was found that 1% change in power can cause 160 mrad of error in the measurement. Since the RMS fluctuation and long term drift of most laser systems are larger than 1%, the magnitude of the error can be significant. Furthermore, it is almost impossible to measure the absolute value of the CE phase with this approach because of the difficulties in accounting the effects of dispersion and linear effects in the f-to-2f setup. It is worth mentioning that an f-2f interferometer can measure relative CE phase but it cannot be used to measure absolute CE phase. The phase-meter based on ATI is the most powerful technique among the several different methods that has been put forward to measure CE phase. In this method, photo-electrons are ejected by the few cycle pulses from the target. Electron-detectors placed on either side of the target perpendicular to the direction of the polarization of the electric field provide number of photo-electron counts. The number of photo-electron counts on each detector depends on the CE phase. Asymmetric photo-electron distribution on the two detectors provides CE phase information. However, a single shot measurement of CE phase from the stereo ATI method has not yet been found reported. An obvious reason for this is the difficulty caused by the space charge effect.

Another method to study the shot-to-shot correlation of change in CE phase with XUV generated by a few cycle pulse has been used by the French Krauze group [10] using spectral selection of cutoff harmonics. However, the bandwidth in a cutoff was quite limited, which is

about 10eV leading ultimately to 250 attosecond. In order to go beyond this limit, a pulse with duration shorter than one optical cycle is required.

In this work, our method relies on the extreme sensitivity of the HHG process with the polarization of the driving laser field. With linear polarization, electron return is possible according to the three-step model [7]. With circular polarization, no electron returns to the parent ion. If we look at the generation efficiency in more detail as a function of the ellipticity, the efficiency is maximum when the ellipticity is zero which corresponds to linear polarization. High harmonic generation efficiency drops down dramatically [11] when ellipticity increases. Even for the small ellipticity of about 15%, the decrease in the efficiency takes place by a factor of two. The idea first proposed by P.B Corkum [12] was to set a time dependent polarization of the laser field starting with the circular polarization that evolves into linear polarization at the center of the pulse and then evolves back to the circular at the end of the pulse. So, each emission of the XUV takes place only at the time when the polarization of the pulse is close to the linear, resulting in the temporal confinement of XUV emission known as polarization gating. In this work we studied the effect of CE phase on the spectra of the polarization gated high harmonics in order to develop an all optical scheme for determining the carrier envelope phase of laser pulses. When driving laser pulse duration approaches a single optical cycle, polarization gating of high harmonics generation is an effective approach to produce a single, isolated, attosecond pulse [13, 14]. As the linearly polarized portion of the gating pulse is as short as half the optical cycle, the extreme ultraviolet (XUV) spectrum of the attosecond pulse is highly sensitive to the shot-to-shot change in the CE phase of the laser pulse [15, 16]. Furthermore, the phase-matching in the gating process was studied in an attempt to boost the number of XUV photons for single shot CE phase measurement.

CHAPTER 2 - Background

Briefly a streak camera is nothing but a photon-electron transducer. It produces an electron replica of the photon pulses from a photocathode.
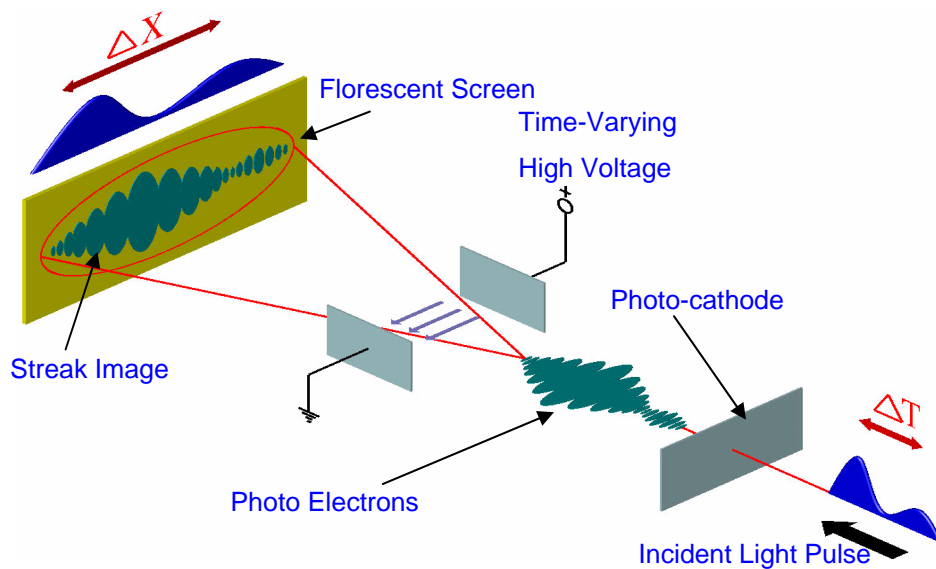
Fig 2.1 Principle of converting time into space with a streak camera

Photon energy incident on the photocathode generates photo-electrons during the life time of the flash of light. Photo-electrons are accelerated toward the florescent screen by high negative voltage applied to the photocathode. On the way toward the screen, before the photo-electrons hit the screen, they are transversely deflected by a field increasing linearly with time. The florescent screen is thus streaked with a line of electron images. Now, the point worth noting here, which of course can also be called the entire principle of the streak camera, is the spatial width of the streak image on the screen, which is proportional to the duration of the light flash. How short a light pulse the camera can measure depends on how fast a time varying field, the deflector can produce. If the time-varying field is very fast, this technique of converting a time dimension into a space dimension can be used to measure the temporal behavior of optical events

at a very short time-scale. Since the spatial dimension of the any image cannot be smaller than the point spread function (PSF) [17], the PSF value provides the limit of the resolution in the imaging process. This is also not an exception in the electron imaging, as electrons emitted simultaneously from a tiny spot of the photocathode never converge to the same point, nor do they reach the image plane at the same time. The limitation to the resolution of the streak camera can therefore be estimated by the so-called technical time resolution, which is expressed as

$$\Delta t_t = \frac{\Delta x}{V_s} \tag{1.1}$$

where, Δx is the FWHM of the PSF and V_s is the sweeping speed. The value of the sweeping speed of the image depends on the rate at which the time varying electric field increases or decreases. So, the relation (1.1) provides the resolution of the streak camera under the best scenario which is limited to the quality of focusing the image and the fast rise and fall time of the driving field. Since other factors limiting the resolution of the detector are not included in the above expression, no streak camera can have resolution better than the value provided by relation (1.1).

2.1. Space charge effect

Due to the space charge effect, a streak camera operating in a single shot mode encounters image broadening, causing negative impact on the resolution of the camera. Mutual repulsion between the charged particles such as electrons within the beam of higher charge density becomes significant for distorting the image. Calculation for electron pulse broadening due to the space charge effect within the photocathode to anode region and the electron drift region have been done by Qian B.L. *et al* [18] by assuming the electron pulse to be a square pulse. The expression for the duration of the electron pulse near the anode, while remaining in their model, shows electron pulse broadening can be greatly reduced by increasing potential at the cathode and decreasing distance between cathode and the anode.

The contribution due to space charge is strong only in the case of a streak camera running in the single shot mode, which requires higher electron density. However, this effect can be eliminated without loss of signal intensity by operating the camera in the accumulation mode.

2.2. Transit time dispersion

Emission of photoelectrons takes place when a photon of energy higher than the work function of the photocathode is shone on it. The work function is the amount of energy an electron must absorb to become free from its bound state. If the photon energy shone on the photocathode is higher than the work function, the excess of energy is converted into kinetic energy of the liberated electron. All the electrons liberated by the process mentioned do not have the same energy. It is therefore very important to be able to estimate the initial energy spread of the photocathode because this is one of the reasons causing the aberration known as chromatic aberration in the electron optics. A rough estimate for the electron spread can be done for any photocathode by neglecting the barrier transmission coefficient for electron of different velocity and the possibility they can be scattered before reaching the surface. Under this assumption, electron distribution n(E) can be expressed as

$$n(E)d(E) \propto \frac{EdE}{\exp\{(E - h\nu + \phi)/kT + 1\}} \tag{1.4}$$

where $h\nu, \phi, k$ and T are the photon energy, work function, Boltzmann constant and the temperature. Plot of the above expression shows the energy distribution of the liberated electrons also varies with the temperature. The typical photo-electron energy spread as a function of electron energy at three different temperatures is shown in Fig.2.2.
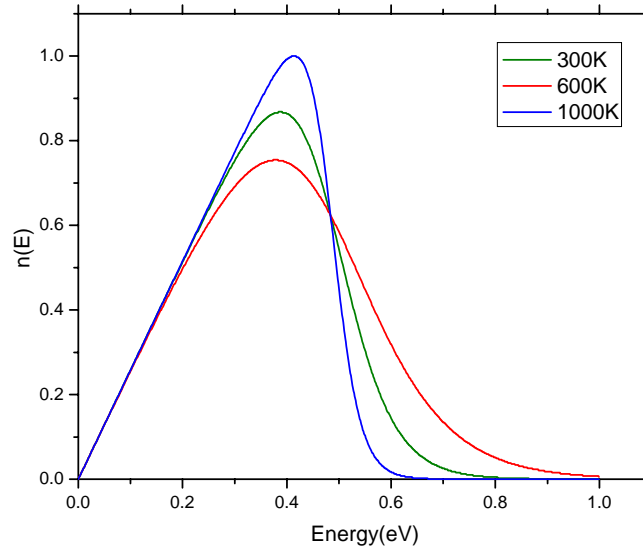
Fig 2.2 Normalized photo-electron energy distribution at different temperature.

The transit-time dispersion in the streak camera is also the result of the initial energy spread of the liberated photo-electrons from the surface of the photocathode. There is no harm assuming the electric field to be uniform in the region between the photocathode and the anode because slit width of the anode is typically less than 1mm.The transit time of photo-electrons in the region of the uniform electric field can be expressed as [19, 20],

$$t_{pa} = \sqrt{\frac{2m}{e}} \frac{\left(\sqrt{V_0 + V_a} - \sqrt{V_0}\right)}{E} \tag{1.5}$$

where V_0 and V_a are the equivalent potential with the initial energy eV_0 and the accelerating potential V_a respectively. m, E and e are mass, extraction field and the charge of an electron. Transit time difference of electrons associated with initial energy eV_0 and initial energy associated with potential, $V_0 = 0$ can be simplified as follows for $V_a \gg V_0$,

$$t^|_{pa} = \sqrt{\frac{2mV_0}{e}} \frac{1}{E} \tag{1.6}$$

The initial energy distribution of a photoelectron generated from the photocathode can be expressed as [20, 21]

$$N(eV_0) \propto \frac{eV_0}{\left(eV_0 + W\right)^4} \tag{1.7}$$

where W is related to the photocathode material. The combination of equations (1.6) and (1.7) boils downs to a simplified expression for the transit time dispersion given by

$$\Delta t_{pa} = \frac{2.63\sqrt{\delta\varepsilon}}{E} \tag{1.8}$$

where $\delta\varepsilon$ is the FWHM of the energy distribution of photoelectrons liberated from the photocathode surface measured in eV. If the extraction field E in eq (1.8) between the cathode

9

and the anode is expressed in kV/mm, Δt_{pa} provides the time in picoseconds. The contribution due to Δt_{pa} in the resolution of the streak camera can therefore be minimized by increasing the electric field between the photocathode and the anode and choosing a material with small $\delta\varepsilon$. The initial energy distribution of gold under 260 nm illuminations is hard to find in the literatures. The polycrystalline Au is not useful for generating photo-electrons, as it has work function 5.1eV, which is higher than the photon energy of UV light (4.7eV) used in the testing. However, the contaminated surface of the photocathode typically has work function varying from 4.2 eV to 4.3 eV, sufficiently lower than the photon energy of UV light. From those photocathode yield $\delta\varepsilon$ = 0.5eV [22] when it is shone with UV photons. In comparison to the spread $\delta\varepsilon$ =1.1 eV from KBr when it is illuminated by an x-ray, the spread from the gold photocathode with UV is half its value. The estimate for the contribution due to transit time dispersion is less for a steak camera tested with UV than for a streak camera tested with x-rays. However, our goal in this work is to study the effect of deflection. It is easier to observe the effect of deflection aberrations if the other factors limiting the resolution are reduced.

It can be seen from the expression (1.8) that by increasing the electric field E between the photocathode and the anode, the transit time dispersion Δt_{pa} can be reduced. Increasing E also reduce the effect of electron energy spread thereby improving temporal resolution. To achieve 100 fs, the electric field should reach 18.6 kV/mm. An obstacle for achieving such a high field is the arcing that takes place between photocathode and the anode. By polishing the photocathode and improving the vacuum, the highest electric field that we were able to reach without arching was 13.75kV/mm at pressure 2×10^{-9} Torr. With this value of the electric field, Δt_{pa} is 136 fs for the gold photocathode illuminated by a UV beam.

2.3. Timing jitter

Timing jitter is the dominant factor limiting the resolution in the x-ray streak camera operating in accumulation mode. Timing jitter is caused by a fluctuation in the laser energy absorbed by the photoconductive switch. Photoconductive switch generates carriers when laser light is incident on it. Resistance of the switch can be expressed as [23]

$$R(E) = \frac{hfL V_{in}}{2V_s e E_{abs}} = \frac{\kappa}{\mathrm{E}_i(\mu J)} \qquad (1.9)$$

where h is Planck's constant, f is the optical frequency, L is the gap width between two electrodes, V_{in} is the voltage across the switch, V_s is the carrier saturation velocity, e is the charge of an electron, E_{abs} is the laser energy absorbed by the switch, κ is the sensitivity coefficient, and E_i is the incident laser energy. The photoconductive switch and the deflection plates of this camera are the same as that used in [24]. The timing jitter is related to κ by the expression [24],

$$\tau_j = t_{ramp} \cdot \frac{\Delta E_i}{E} \cdot \frac{\kappa}{\kappa + Z_{imp} \cdot E_i (\mu J)} \qquad (1.10)$$

where t_{ramp} is a final output ramp pulse due to the combined effect of the ramp due to the switch and the deflection plate. Z_{imp} is the equivalent output impendence and $\Delta E_i / E$ is the pulse-to-pulse fluctuation in laser energy. The photoconductive switch (described in detail in chapter 2) has $Z_{imp} = 50\Omega$ and $\kappa = 25 \ \Omega \mu J$. Liu *et al* measured timing jitter less than 50 fs at the energy [24] ranges 20-160 μJ when shot-to-shot laser fluctuation was 1.2%.
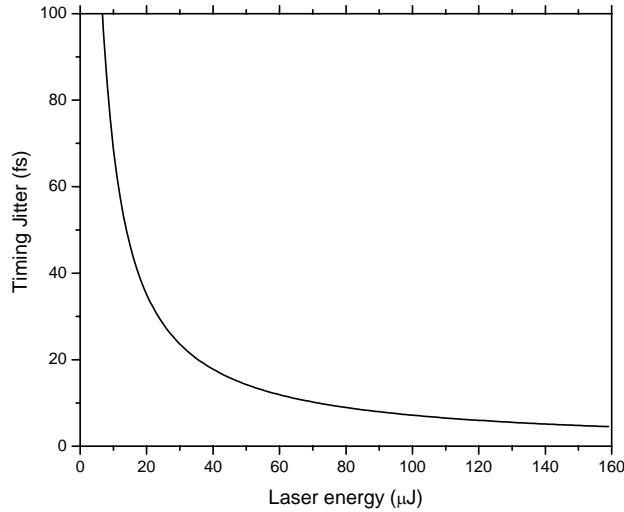
Fig 2.3 Timing jitter as a function of laser energy for laser stability 1.2%

From the expression (1.10), minimum jitter may be expected at higher laser energy and consequently less fluctuation in the sweeping speed. Freedom of using higher laser energy is prevented by the growth of amplified spontaneous emission (ASE) on the leading edge of the

driving pulse. In our photoconductive switch an ASE pulse did not appear until the laser energy was less than $180\,\mu J$ as shown in Fig.2.4. As energy is increased to $200\,\mu J$, it increased linearly as shown in Fig.2.4.
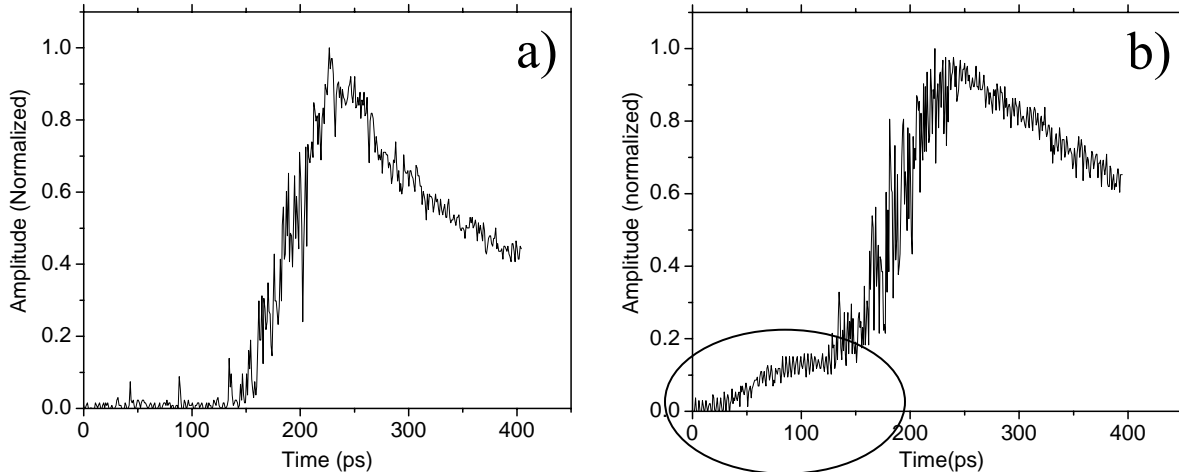
Fig 2.4 Electrical signals at switch output with a) $80\mu J$ and b) $200\mu J$ laser energy illumination.

2.4. Deflection Aberration

Deflection aberration is caused by the finite beam size of the electron. When electrons
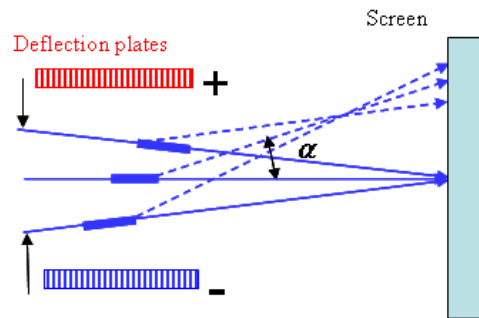
Fig 2.5 Two focal spots, before the screen and at the screen due to finite electron beam size for the same focusing voltage with and without deflecting field.

travel along the deflection plates, electron, near the higher potential speed up faster than the electrons farther from it. Because of the transverse gradient in the speed of electrons due to the transverse variation in the electric field inside the deflector, an electron beam steered by the deflector focuses before reaching the screen as shown in Fig.2.5, thereby causing image broadening. For the same focusing voltage, if the electron beam is not influenced by the

12

deflecting fields, the beam will be focused on the screen with a sharp and narrow image. The effect of the beam size d on the temporal resolution can be estimated by [25],

$$\Delta t_d = \frac{d\alpha}{v_a}$$ (1.11)

where α is the maximum deflection angle in radians in Fig.2.5, and v_a is the average axial velocity.

Fig. 2.6 shows how both the focused images can be formed on the image plane with minimum dispersion by introducing an aperture slit which reduces the electron beam size entering the lens and the deflection plates successively. The temporal resolution therefore can be improved significantly by reducing the electron beam size, d in the focusing lens and in the deflection plates. Fig.2.7 i) and ii) shows the result of the Simion simulation when the beam size inside the quadrupole and the deflection plate is broad and small respectively. When no aperture stop is introduced, the beam is focused before reaching the screen at the focusing voltage ± 104 V and deflecting field ± 60V (Fig 2.7 (a) and (c)). In this case image broadening may be expected due to dispersion known as deflection dispersion. When the deflecting field is zero, the beam is focused on the screen(Fig.2.7 (b)).On the contrary, as the beam diameter just before entering the quadrupole lens is reduced to the size defined by the 100 μm slit, an image is focused on the screen with and without the deflecting field (Fig.2.7 ii)). Evidently, the simulation shows that dispersion can be suppressed by reducing the beam size in the electrostatic lens and deflection plates.
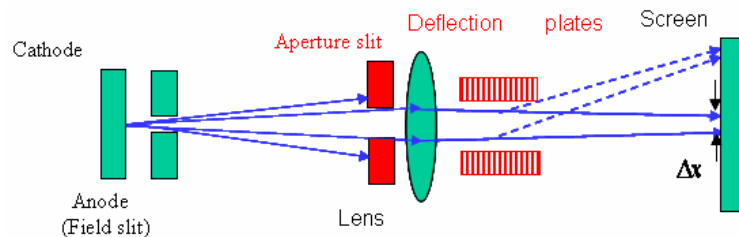
Fig 2.6 Both images with and without deflecting field focused on the image plane when aperture slit is introduced in front of the lens.

13
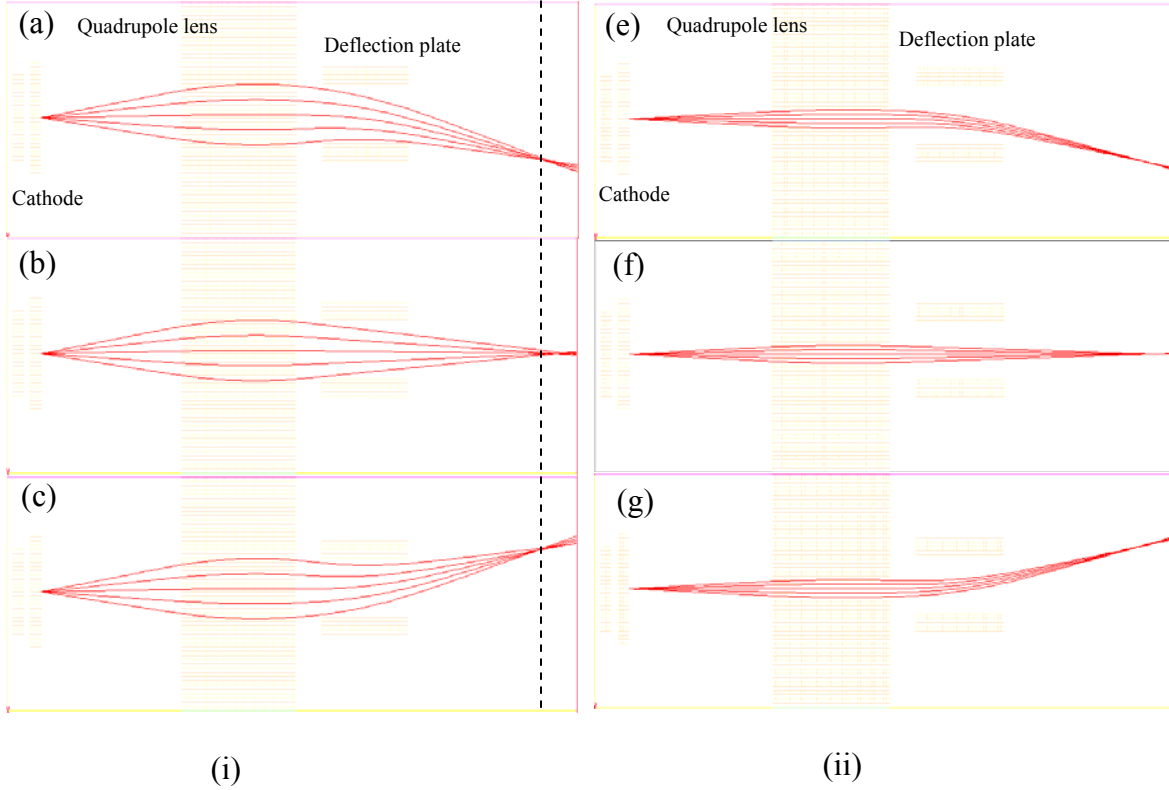
Fig 2.7. i) Beam is focused a) before, b) on and c) before the screen when image is steered by the transverse field of ± 60V, 0V and ± 60 V at focusing voltage 104V. ii) As beam size is reduced defined by 100 µm slit, beam is focused on the screen at both ± 60 V and 0 V indicating reduction in the dispersion.

The total temporal resolution that one can expect from a streak camera when all the factors mentioned above are included can be expressed as

$$\Delta t = \sqrt{t_t^2 + \Delta t_{pa}^2 + \tau_j^2 + \Delta t_d^2 + \Delta t_{sp}^2}$$

(1.12)

As a streak camera which runs in the accumulation mode is negligibly affected by the space charge effect, we can remove Δt_{sp} term from the expression (1.12). The resolution of an accumulative x-ray streak camera can therefore be calculated from the four factors given by

$$\Delta t = \sqrt{t_t^2 + \Delta t_{pa}^2 + \tau_j^2 + \Delta t_d^2}$$

(1.13)

14

CHAPTER 3 - Design and Experimental Set-Up

An x-ray streak camera has uniquely been designed to run in an accumulation mode as the space charge effect in the single shot mode constrains the flexibility of using higher input photon flux. In other words, single shot operation has been undervalued by the tradeoff between better resolution and higher dynamic range. Desire for better resolution and the higher signal intensity will be clear when one tries to measure the ultra-fast interaction in the crystal triggered by an ultra-short laser pulse. Since the alteration of the x-ray diffraction signals, which emerge from ultra-fast reaction in the sample, is typically very weak, it can be detectable only with a detector having high dynamic range and better resolution. Although signal intensity can be increased by operating the streak camera in accumulation mode, degradation in the temporal resolution in this case cannot be eliminated unless timing jitter is reduced. In this chapter I will describe our design of an accumulative streak camera with timing jitter < 100fs and temporal resolution < 300fs.In addition, our design of a photocathode transferable holder, in order to fit into the measurement using a wide rage of spectra from UV to x-ray, will be described.

3.1. Streak Tube

As for any standard streak camera, the streak tube consists of i) a photon-electron transducer (photocathode) ii) focusing lens and deflector and iii) image detector. Typically, the photocathode used in the streak camera is Au, KBr, KI, Al etc. depending on the wavelength of the illuminating beam. As the electron energy spread distribution from the surface of different photocathode is different, a better choice for the photocathode relies on low energy spread distribution (equation (1.8)) of electron and high electron throughput. Due to remarkably high stability in photoemission even under exposure to the atmosphere [26], a gold photocathode has been chosen to test the streak camera. The photocathode is housed in a specially designed cylindrical ceramic holder (Fig.3.1). A 5mm wide ring projected along the inner wall below 12.5 mm from the entry window of the ceramic holder serves as a shelf to stack a 2mm thick copper ring and exchangeable steel spacers. The other end of the cylinder is mounted on a 5.08 cm stainless steel disc which has a 1.5 cm screw hole at the center to mount an anode rod. An anode

is a 1.8 cm hollow stainless steel rod with a base of 2.54 cm diameter and 5mm thick disc. An open hole of 5mm diameter from the center of the base to the other end of anode provides passage for a photo-electron beam. A helical screw thread immediately above the anode base provides access to fasten the anode rod in the ceramic holder and fine tune the distance between its surface and the photocathode. A 3 mm long and 25 µm wide steel slit mounted on the anode surface defines the field of view of the camera. A 2 mm thick copper ring and spacers of thickness 0.5 mm and 0.25 mm are placed directly in contact with the gold-coated face of the photocathode which keeps the surface of the photocathode and the anode 1.05mm apart. When no

ab=spacer1=0.5mm
ad=12.5mm
bc=spacer2=0.25mm
cd=copper ring=2mm
ec=0.3mm
ea=gap=1.05mm
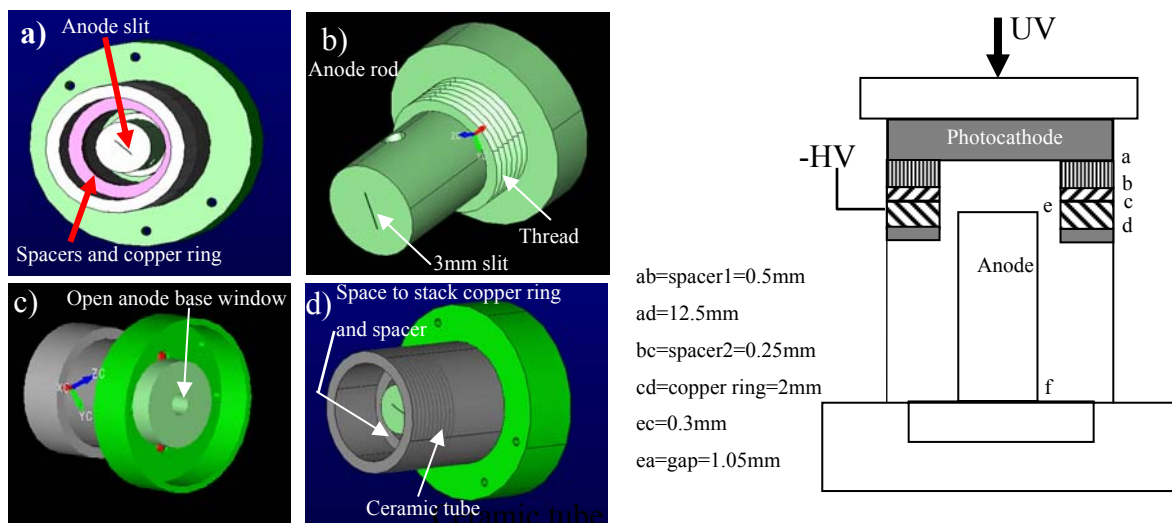
Fig 3.1 Anode and cathode enclosure i) a) Top view b) Anode rod c) closed enclosure d)side view ii) Schematic of anode and cathode enclosure.

spacers are used, the anode and cathode are separated by 0.3mm. The novelty of this design also allows fine tuning of the distance between the cathode and anode by turning the anode rod about its axis. High negative voltage is applied to the copper ring, which produces a high electric field between the grounded anode and the photocathode. The high voltage on the copper ring also provides energy to the electrons generated from the photoelectric effect. In order to minimize transit time dispersion, it is necessary to apply high voltage between cathode and anode. However, electrical breakdown which occurs at the high electric field prevents from the application of high voltage. Threshold electric field for the occurrence of electrical breakdown

was increased in our design by polishing the anode surface and improving vacuum. The highest electric field at which the camera can withstand arcing is 13.75kV/mm while operated at pressure
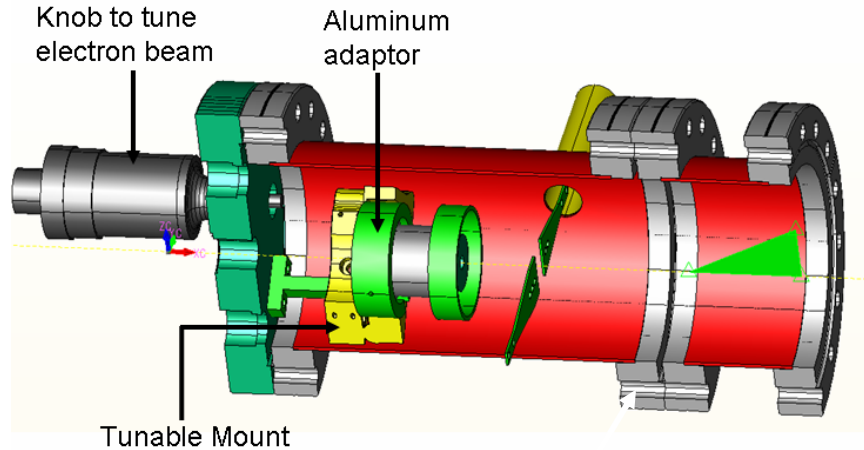
Fig 3.2 An assembly of cathode, anode, spacers and copper rings installed on a tunable mount with external knobs.

2×10^{-9} Torr. The cylinder is closed by a disc of diameter 1.5 inch with a 3mm circular hole at the center. The lid is then wrapped along its circumference by an adaptor of 2 inch diameter in order to fit into a mount tunable externally with two knobs (Fig.3.2). The knobs allow us to align an electron beam with the axis of the streak camera which is very crucial to avoid off-axis aberration. For the test, a view port made of fused silica was used to transmit UV in order to minimize the transmission loss. It has been identified that no other material matches the purity of fused silica or has exceptional transmittance over wide range, especially in the ultraviolet. Our design of the streak camera has been unique so far by the presence of slit mounts. These slit mounts are the unique part of this camera which has five punched holes about the size of 3mm diameter (Fig.3.3). The punched holes are covered by slits of different widths (5μm, 25μm, 10μm, 50μm and 100μm). Those mounts are installed on a pair of feedthroughs which allows movement of the mount perpendicular to the beam direction just in front of the entry window to the electrostatic lens (described shortly). Since the mount carries slits of different widths, the electron beam can be reduced in size along the transverse direction by allowing beam to enter through different slit widths. This mechanism allowed us to study the dependence of the

17

resolution of the camera on the beam size inside the electrostatic lens and the deflector. In order to focus the beam along the transverse direction, an electrostatic quadrupole lens was used. The
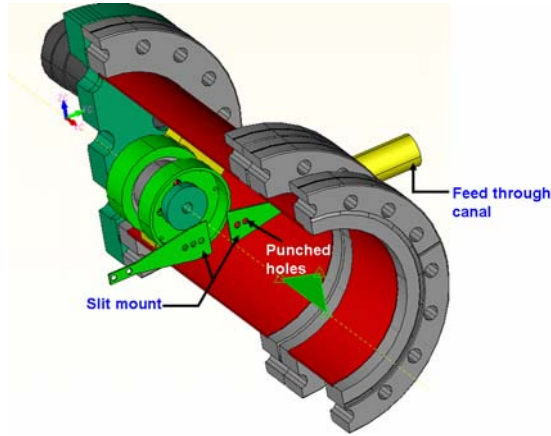
Fig 3.3 Punched holes on the triangular shaped stainless steel flippers. Holes are covered by slits of different width. Flippers are fixed on the feedthrough which passes through the feedthrough canal.

quadrupole lens consists of four half cylinders made of copper which are mounted on the four walls of the stainless steel box. In order to reduce aperture aberration and improve focusing quality,

$$\frac{R_e}{R_O} = 1.148$$
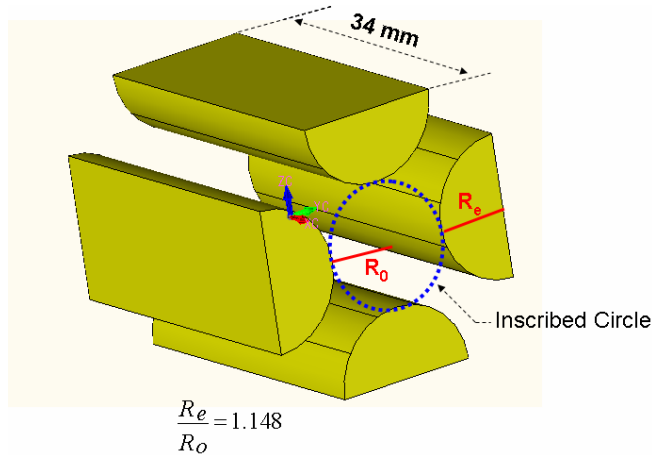
Fig 3.4 Quadrupole lens with electrode rod radius R$_e$ and inscribed circle radius R$_o$

four half cylinders of 34mm long and 15mm diameter are mounted in such a way that it satisfies the condition $R_e = 1.148\,R_O$ [27-29], where R_e and $2\,R_O$ are the radius of the electrode and the spacing between diametrically opposite electrodes(Fig.3.4). To drive the electron beam along the transverse direction, a pair of specially designed deflection plates was used. Those plates are

18

made of a pair of PC boards of area 2.4 inch by 1.6 inch which have printed meander structure on the surface by a thin film of copper(Fig.3.5). The PC plates are also mounted on the same
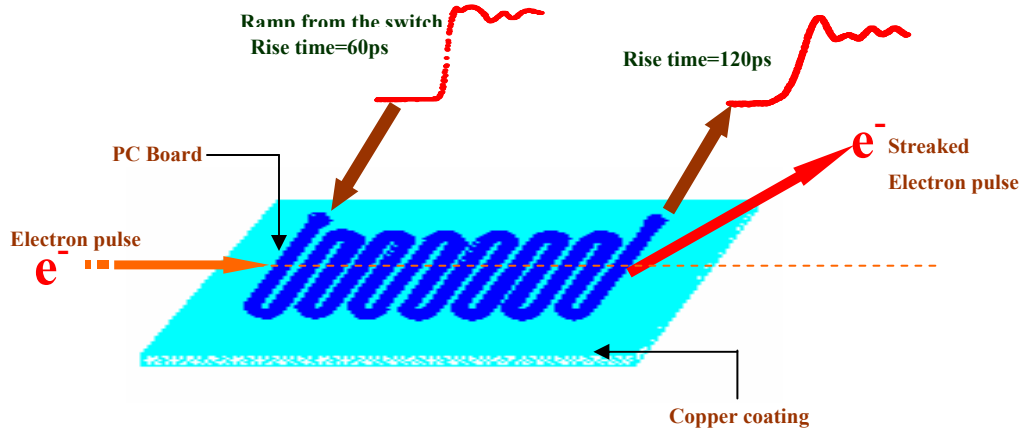
Fig 3.5 Thin film of sinusoidal copper coat on the PC board slows down the input ramp pulse thereby causing repeated interaction of relatively slow speed electron with the transverse field.

steel box where the quadrupole lens was mounted with their meander structure facing the electron beam. As the electron beam travels between the deflection plates, an electric field pulse with fast rising and falling times also co- propagates with the electron pulse. The electrons within the pulse at different times therefore encounter different forces of the electric field which depends on when the electrons arrive with respect to the quickly varying ramp field. The meander conducting pattern in the deflection plate slows down propagation of the ramp pulse which otherwise travels with much faster speed than the electron pulse. The electron pulse traveling within the deflection plate therefore interacts repeatedly with the transverse field giving rise to the large distribution of the transverse velocity. As the transverse velocity is directly proportional to the temporal profile of the electron beam, the beam is streaked along the perpendicular direction to the slit as it exits from the deflector. The meander structure therefore keeps the field constant as long as the electron travels between the pair of deflection plates thereby increasing the scanning speed. A microchannel plate of 25.4 mm diameter is used to intensify the signal and imaged on the phosphor screen. BURLE premium quality microchannel plates with Chevron configuration produce a high gain of 10^7 at maximum voltage 2.4kV. For the best performance under Chevron configuration, a channel plate of bias angle 12^0 was chosen.

As spatial resolution is inversely proportional to the center to center spacing so-called pitch, its fairly low pitch of 6 micron provides high spatial resolution.

3.2 Photoconductive Switch

The timing jitter is the chief cause for producing worse resolution as long as the camera is operated in an accumulative mode. As this camera is also supposed to operate in an accumulative mode, the effort to reduce timing jitter is the primary objective of this work. It is impossible to make timing jitter absolutely zero without making the laser energy fluctuation absolutely zero. Timing jitter however can be reduced to such a small value that its effect can be neglected.
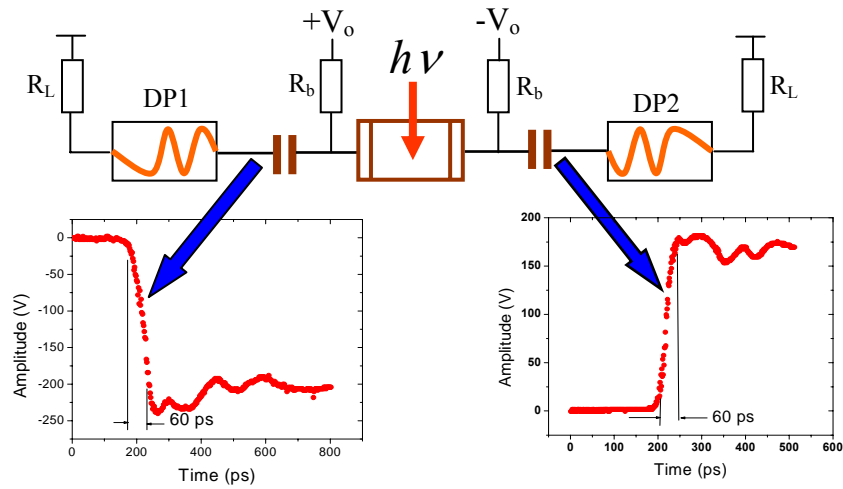
Fig 3.6 Configuration of the photoconductive switch

A photoconductive switch to generate a ramp pulse for driving the deflection plate in this design is similar to that in Liu *et al* [24, 30] except that the 2 GHz connection cables were replaced by one with a 18 GHz bandwidth to reduce the rise time from 90 ps to 60 ps. DP1 and DP2 are the deflection plates. $+V_o$ and $-V_o$ are the DC voltages applied to the switch. The photoconductive switch used in this experiment is made of semiconductor GaAs that has a resistivity of 10^7 Ω-cm. The active zone of this switch has area 0.5 cm^2. Contact resistance was reduced sufficiently by depositing electrodes on the switch with a 2 mm gap between them. The switch was mounted on a circuit board with a 50 Ω transmission line, in an attempt to make response time as fast as possible; and to eliminate the pulse reflection, the capacitance of the DC block is 1000 pf. As laser energy is incident on the switch, it turns on and produces symmetric output to the deflection plates. By operating the camera at the saturation regime, the fluctuation in the output voltage was

20

made less sensitive to the laser energy fluctuation. To test the camera, the laser energy was set at 60 µJ. It was expected that jitter would be less than 100 fs [24].
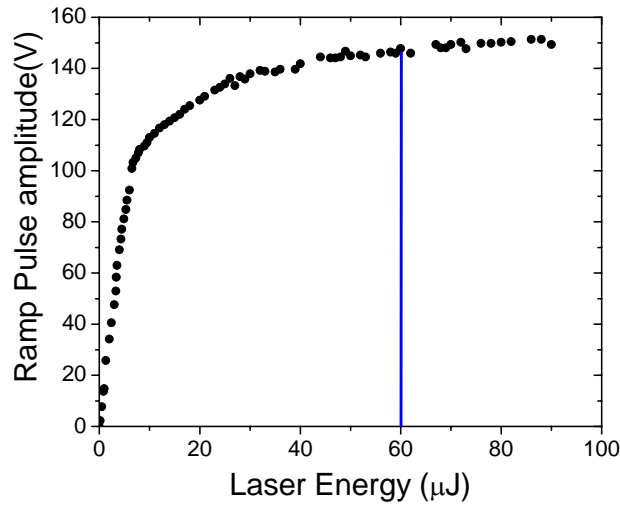
Fig 3.7 The dependence of the pulse amplitude from the GaAs switch on the trigger laser energy.

3.3. Experimental Set-up

To calibrate the scanning speed, a Mach-Zehnder interferometer was used to split a Kansas Light Source laser beam into two beams as shown in Fig.3.8. The laser pulse duration is 30 fs and the center wavelength is ~790 nm. Two mirrors M_1 and M_2 are mounted on a translational stage which permits to setup delay for the experiment. A 50% beam splitter BS_1 transmits and reflects two beams of equal intensity. The reflected beam undergoes further reflections through mirrors M_3 and M_4, while transmitted beam is reflected by the mirrors M_1 and M_2 sitting on the
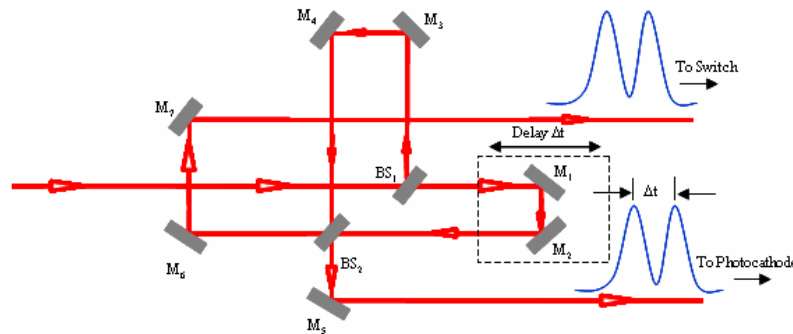
Fig 3.8 Mach-Zehnder interferometer to produce known delay for speed calibration

21

translational stage. The two beams overlap and interfere immediately after they are split by another beam splitter BS$_2$. An optical path difference between two pulses can be introduced by sliding mirrors mounted on the stage.

The system for characterizing the camera is shown in the Fig. 3.9. The Ti:Sapphire laser generates 2 mJ energy at 1kHz repetition rate. 85% of the total output was sent to a Mach-Zehnder interferometer. The interferometer has two laser beams output. Each beam contains two
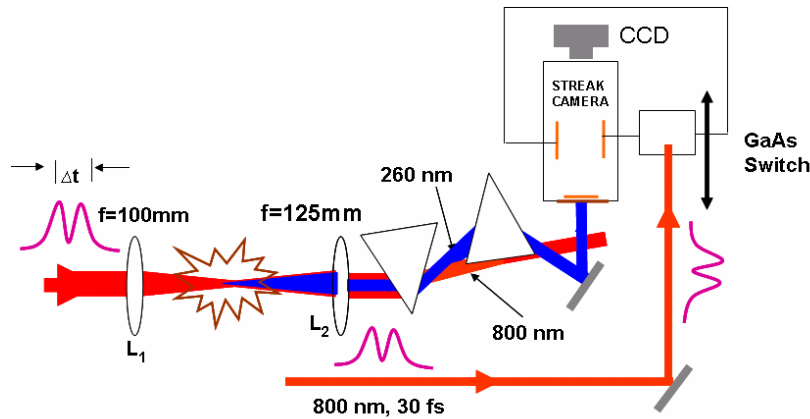
Fig 3.9 The layout of the setup for charterizing the streak camera

pulses with a predetermined time delay per laser shot. One beam from the interferometer was sent on the GaAs switch, which was mounted on the rail. The near infrared laser pulses triggers the switch to generate ramp-voltage pulses for driving the deflection plate. In the meantime the other beam from the interferometer was frequency converted into UV light by focusing near infrared in air by a lens of 100cm focal length. The central wavelength of UV light is ~260 nm that is the third harmonics of the laser. Pulse duration of the UV pulse is expected to be less than 100 fs. Another 125 cm focal length lens was used to collimate the beam. The collimated beam is incident on the prism to separate UV from the infrared, and an extra prism is used to reduce dispersion of the UV beam. Finally, the UV beam is incident on the gold photocathode to generate
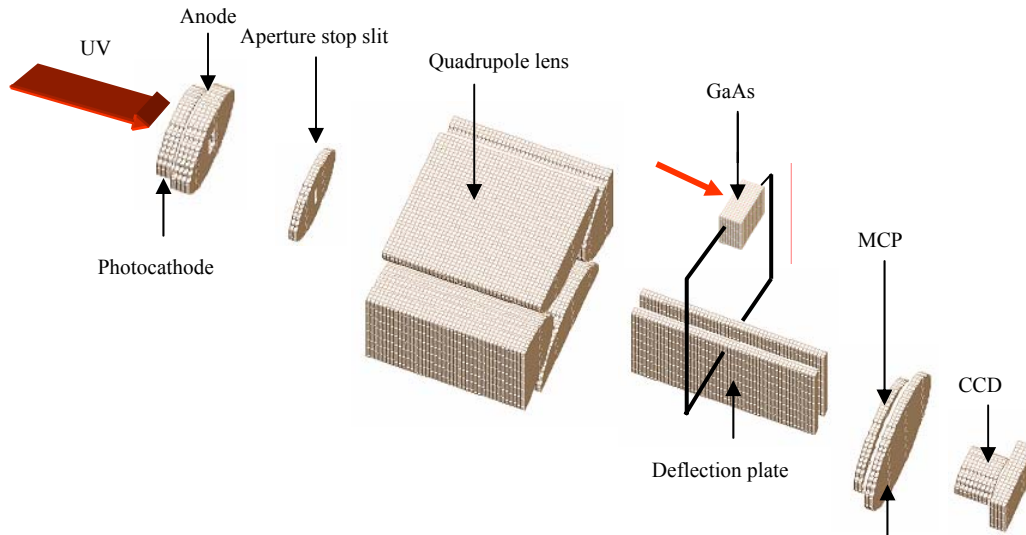
Fig 3.10 Schematic of the streak tube with a slit that serves as the aperture stop.

electrons. The electron beam is collimated by a slit of 25 µm wide and 3 mm long. A second slit in front of the entry window of the quadrupole lens adjusts the transverse beam size. An electrostatic quadrupole lens focuses the beam in the sweeping direction. Spherical aberration of this lens is smaller compared with the lens with axial symmetry. An electron beam deflected by a highly sensitive meander type plate is intensified by a microchannel plate (MCP) and is displayed on a phosphor screen. The final streak image is recorded on charge-coupled-device (CCD) video camera. Using the video rate camera (Cohu 4920) instead of the slow-scan CCD allows real time optimization of the camera operation. The camera is cooled to 5^0 C, which allows signal accumulation up to 1 min.

3.4. Necessary Considerations

The following are the three factors that can severely affect the accuracy of the measurement.

i) External magnetic field ii) Electric field iii) Static Charge

i) External magnetic field

An external magnetic field can modify the paths of the low energy electrons. The image will be shifted out of the phosphor screen if the presence of external magnetic field is not eliminated.

23
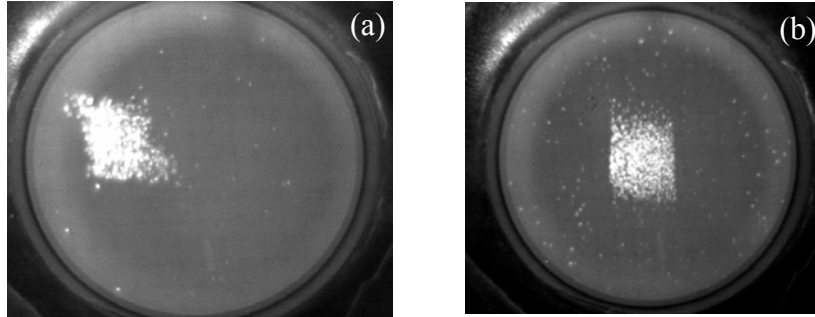
Fig 3.11 Electron image a) before b) after the magnetic shield was used. The presence of external magnetic field influence on the electron beam was manifested by the shift in the image from the center.

The following picture (Fig.3.11a) was taken when the streak tube was not protected from the external magnetic field. By using non-magnetic material and wrapping the streak tube with magnetic sheet, the magnetic field inside the chamber can be completely eliminated (Fig.3.11b).

ii) Electric Field

There are sets of cables which connect the deflection plates and the quadrupole with the external power supply. The magnetic field from those cables therefore can significantly drift the beam from the axis of the electrostatic lens and the deflection plates. That might therefore distort the focused image. The solution to this problem is to pass all the cable outside the internal shield.

iii) Static Charge

As deflection plates are made of PC board and floated, it is very likely that charge can accumulate on the nonconducting surface. Those static charges can destroy the function of the
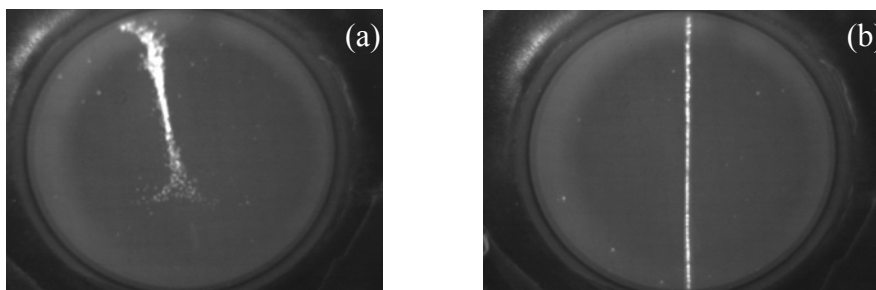
Fig 3.12 Electron image (a) before (b) after anti-static spray.

quadrupole lens. Poor focusing of image by quadrupole lens in Fig.3.12a was caused by the static charge effect on the electron beam. Image was nicely focused into thin vertical line with the same focusing voltage after anti-static spray was used (Fig.3.12b).

CHAPTER 4 - Results and Discussion

4.1 Band width dependence on ramp voltage

Ramp voltage from the GaAs switch and the deflection plate was compared for cables of different bandwidth using a 20 GHz Sampling Head Oscilloscope. The rise time and fall time of the pulses from the switch reduced from 90 ps to 60 ps and these from the deflection plates
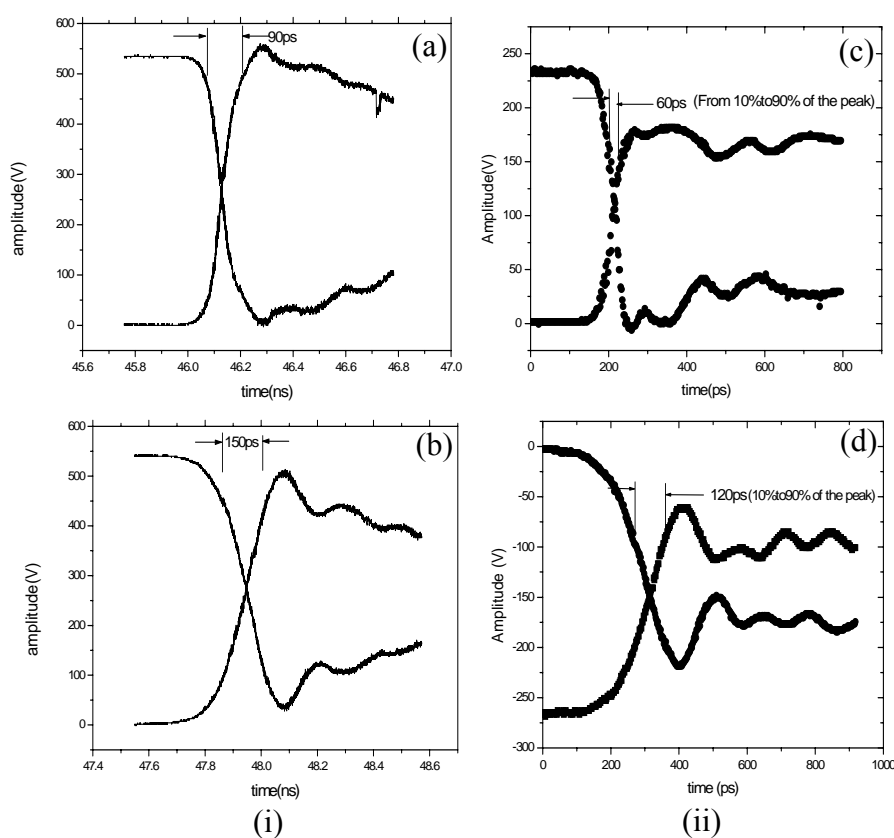
Fig 4.1 (i) Ramp output (a) from the switch (Liu et al) (b) from the deflection plate with 2GHz cable (ii) Ramp output (c) from the switch (d) from the deflection plate with 2GHz cable replaced by 18 GHz cable.

reduced from 150 ps to 120 ps at laser energy incidence 60 µJ, which is sufficiently below the damaging energy of the switch. The rise time and fall time of the pulses are taken at 10% to 90% of the peak. It is very crucial to have response time as fast as possible to increase sweeping

26

speed. It is apparent from our result; scanning speed can be made faster by using the cable with higher bandwidth.

4.2. Dependence of Quadrupole Geometry on Focusing

The quality of focusing from the quadrupole lens set at two different values of ratio r_e/r_o was tested by applying the same focusing voltage $\pm$ 85 V, where, $2r_o$ is diametrically opposite distance between the two quadrupoles. Fig.4.2 (a) and (b) are the two results of measurements of image width obtained for the ratio 1.148 and 1.9 respectively. For ratio 1.9, the static
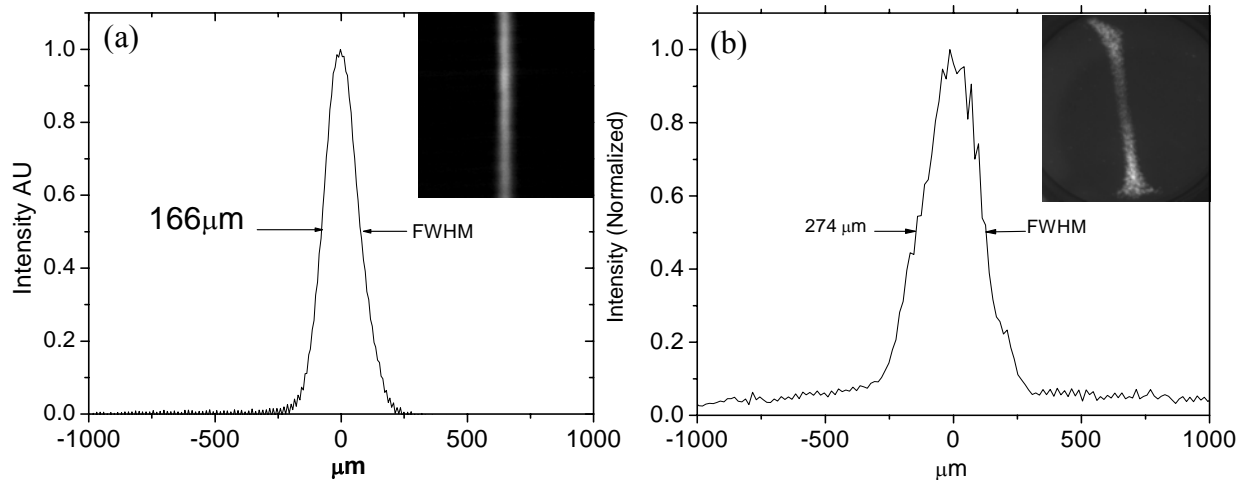
Fig 4.2 Static image and its line out for the value of r_e/r_o (a) 1.148 and (b) 1.9

image width was 274 μm FWHM, which reduced to 166 μm when the ratio was set to 1.148. The result obtained was in better agreement with the assumption made on the lens which would serve as an ideal quadrupole consisting of four parallel electrodes with hyperbolic cross-sections carrying potential $\pm$85V on each [31]. If the static image width is narrow, we can expect better resolution from the camera as the limit of the resolution is set by the ratio between static image and the sweeping speed. About 40% reductions in the width clearly show the geometrical dependence of the quadrupole lens on the resolution of the camera.

4.3 Dependence of cathode and bias voltage.

The effect of cathode and bias voltage on the sweeping speed was studied extensively. The change in sweeping speed with the change in cathode voltage and the bias voltage is shown in

Fig. 4.3 and Fig. 4.4 respectively. By sliding a photoconductive switch through 0.5 mm along the direction of the incident near infrared beam, the sweep speed was estimated. Exposure time of the CCD camera was set to 6 sec during the time of observation. As sweeping distortion began to appear in the measurement at the larger change in the position of the photoconductive switch, the plot was obtained sliding only through a small distance. Since, during the observation, laser energy fluctuation was relatively higher, the corresponding fluctuation in amplitude of the driving ramp produced a random shift in the image per laser shot. Therefore, the average position of the image was taken to estimate the sweep speed for each cathode voltage. A certain amount of deviation of the points from the linear fit in the plot can be understood because of laser energy instability. Within the limit of those energy fluctuations and sweeping distortions, it is apparent from the plot that scanning speed decreases almost linearly with the increase in cathode voltage. Observations were made and presented up to -10kV without any electrical breakdown at pressure $\sim 10^{-10}$ Torr. The gap between the anode and the cathode was 0.8 mm and the bias voltage to the
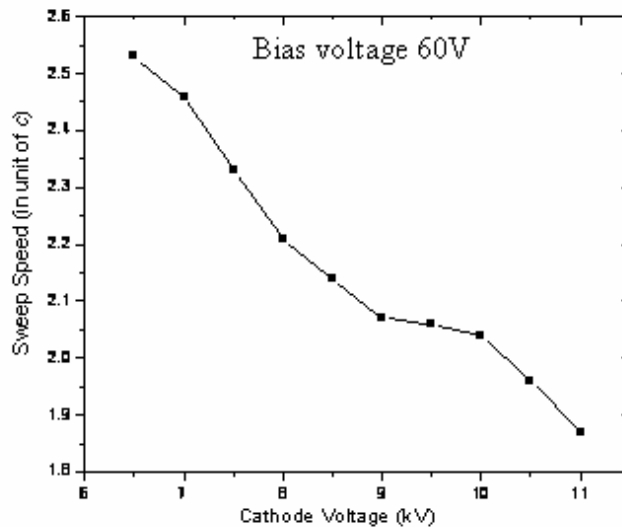
Fig 4.3 Dependence of scanning speed on cathode voltage

deflection was set to 60V. This study gives the idea that the higher sweep speed can be maintained at the same electric field (13.75 kV/mm) by reducing the space between the anode and the cathode while keeping cathode voltage constant at -7kV. However, only a higher vacuum system, less than $\sim 10^{-10}$ Torr, allows us to reduce space to achieve such a high electric field without arcing. The lowest pressure that the current system can give is slightly higher than 10^{-10}

Torr which limits the spacing to 0.8 mm between the cathode and anode at -11kV without electrical breakdown. As speed is not very high at -11kV, the vacuum should be greatly improved in order to be able to reduce the cathode-anode space and the cathode voltage to achieve 100fs resolution.

Since one of the objectives of this experiment is to identify an optimum value of bias voltage which would produce maximum sweep speed without distorting the image, we investigated its effect on the sweep speed. The result of our study is summarized in Fig. 4.3. and Fig.4.4. Dependence of the bias voltage on the sweep speed was linear up to 70 V. Voltage beyond this value no longer shows the linear relationship with the speed. As the electrostatic lens and the deflection plate are very closely installed, the electric fields of the quadrupole and the deflection plates begin to interact at the higher bias voltage. The scattered points in the plot can be attributable to this interaction.
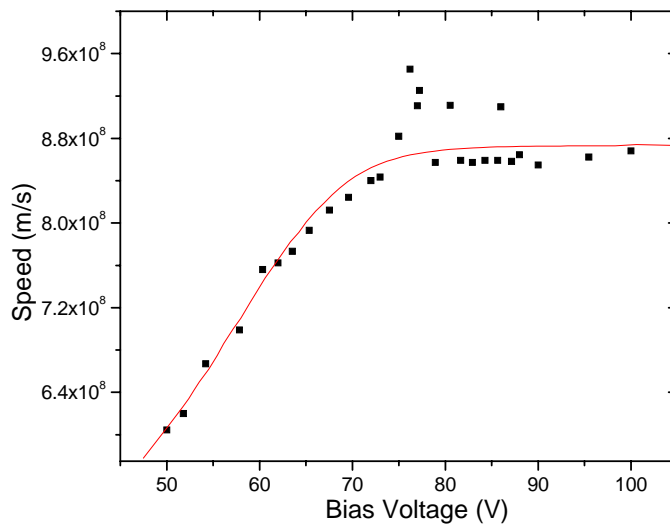
Fig 4.4 Dependence of scanning speed on bias voltage.

Fig. 4.5. is the plot of resolution of the camera as a function of the different anode voltage obtained applying an aperture stop slit 50 μm wide. The space between the anode and cathode was kept the 1.3 mm during the time of measurement. Temporal resolution of 451 fs was obtained at the cathode voltage 8.5 kV which corresponds to the electric field of 6.5 kV/mm in the gap between the anode and the cathode at the focusing and bias voltage ± 85 V and ± 68 V respectively . As sweeping speed decreases with the increase in cathode voltage (Fig.4.3), better

resolution may be expected at lower cathode voltages by remaining at the same extraction field. In this case, the space between the anode and cathode should therefore be decreased in order to retain the extraction field. So, it turns out that much better resolution than that presented in Fig. 4.5. at 8.5 kV can be obtained if the cathode voltage and the space between the cathode and anode is reduced further.
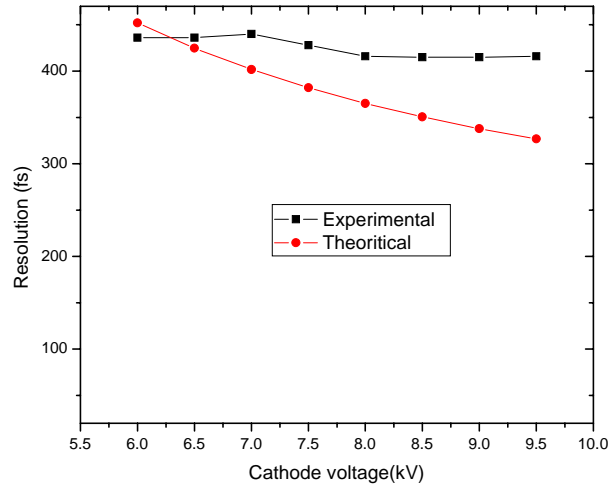
Fig 4.5 Resolution as a function of cathode voltage at bias voltage ± 68 V with 50 µm wide slit.
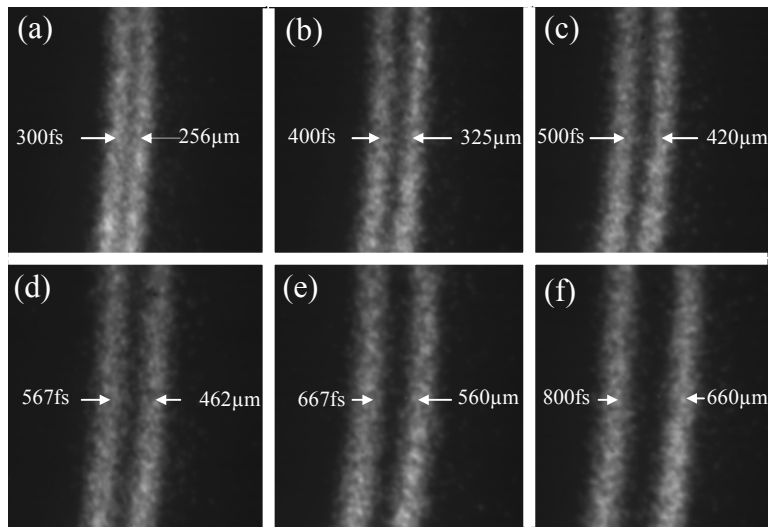
Fig 4.6 Images of two pulses set to different known delays to calibrate sweeping speed.

Since the resolution of 451 fs was obtained from -8.5 kV at 6.5kV/mm, ideal resolution of 200 fs may be expected from -8.5kV and 10kV/mm, which our design allows us to test experimentally, by providing access to exchange or remove the spacer between the anode and the cathode.
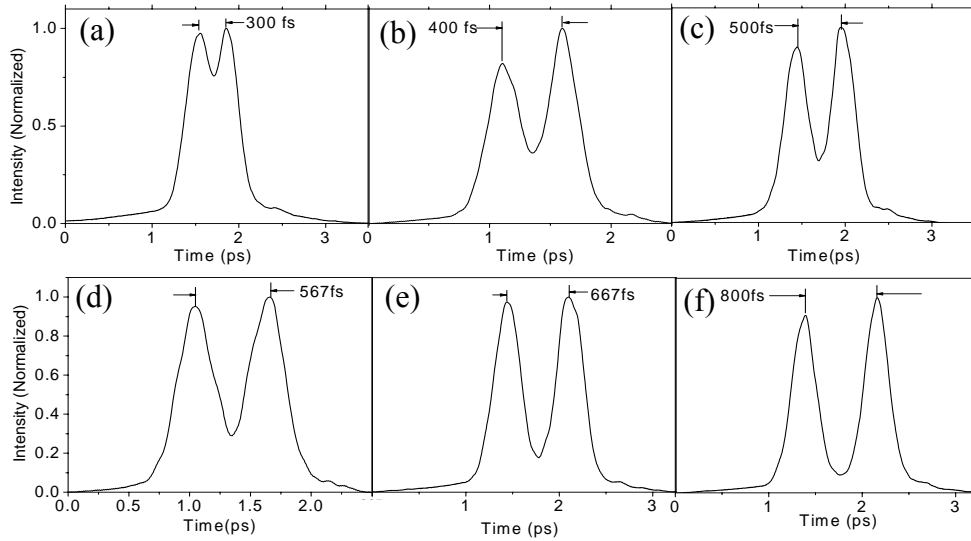
Fig 4.7 Line out of images of Fig. 4.6.

Mach-Zehnder interferometer from our setup generates two identical pulses. In order to calibrate the speed of the camera, the first two beam spots from the two arms of the interferometer were

Speed = 0.84 μm/fs = 2.8c
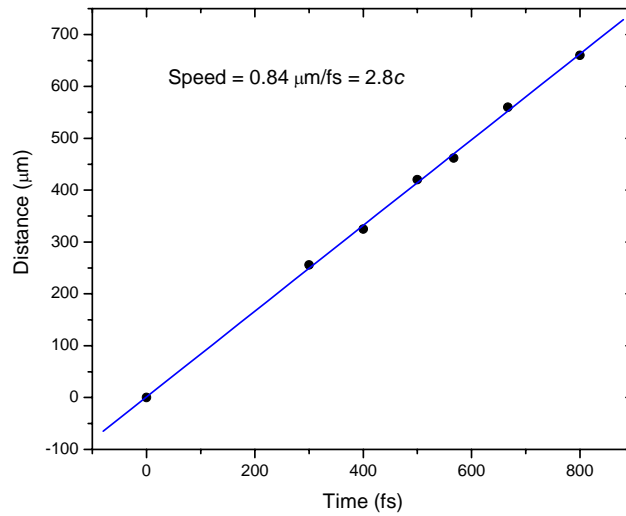
Fig 4.8 Plot of spatial separation against temporal separation of the images.

overlapped near the setup as well as far from the setup. Then, by gently moving the delay stage, the images were overlapped temporally and spatially. Perfect overlapping of the pulses was ensured by having three-fold enhancement in the brightness of the image at a particular position. Referencing that position as a zero delay, known values of delay were introduced between the pulses in order to calibrate the speed of the camera. Fig.4.6. shows the images of two pulses at different known delays. One pixel of the CCD camera image corresponds to 7μm. Spatial separation of the images as a result of delay was estimated simply by multiplying the value per pixel (7μm) and the number of pixels by which the two images were separated. Fig.4.7. is the line out of the images of Fig. 4.6.The temporal separation between two peaks from each plot and corresponding spatial separation of the images provide the average sweeping speed of the camera. Fig.4.8. is the plot of distance between two images against the delay. From the slope of the fitted line in the plot, the speed of the camera was found to be 2.8 times the speed of the light.

4.4 Effect of beam size on the static image

Without the second slit in front of the aperture window of the quadrupole lens, the static image width Δx = 166 μm, as shown in the Fig. 4.2. The width is much larger than the ideal value 52.1 μm, which is the product of the anode slit width and the magnification of the streak
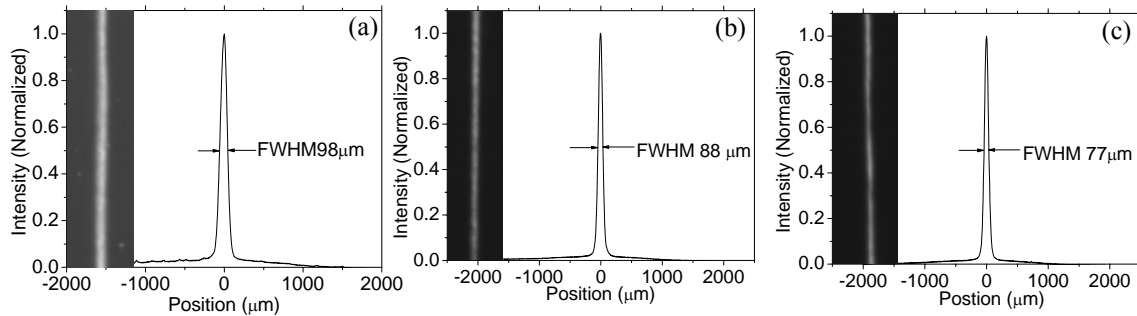
Fig 4.9 Static images and their lineout when 2ⁿᵈ slit width is (a) 50μm (b) 25μm and (c) 5μm.

tube. The broadening of the image width was caused by the aberrations of the quadrupole lens. The aberrations were reduced by reducing the electron beam size in the lens. The narrowing of the image width by the second slit was significant, as shown in Fig. 4.9 [32].The narrowest image is 77μm, obtained when the width of the 2nd slit was 5μm, which is close to the ideal

value. For the image width of 77μm and the scanning speed of 0.84μm/fs, the estimated resolution from equation (1.1) is 92 fs.

4.5. Effect of beam size on the dynamic image resolution

As our design allows us to exchange the aperture stop slit of different width, we investigated the effect of electron beam size on the resolution. In order to measure the transverse profile of the beam, we chose a 25 μm aperture stop, as beam intensity was too low for this measurement with 5 μm slit. However, a slit of width as small as possible was chosen to increase number of data points in the measurement. The measured transverse profile of the electron beam is shown in Fig.4.10 [33], which was measured by scanning a 25μm slit across the electron beam at the entrance of the quadrupole lens. FWHM of the beam is ~1mm, thus, the aperture stop slit significantly reduced the size of the electron beam in the lens. Although the size of the electron beam at the entrance of the deflection plate was not measured, the sizes are expected to be close to the width of the slits. The results obtained by changing the beam size using the aperture stop of
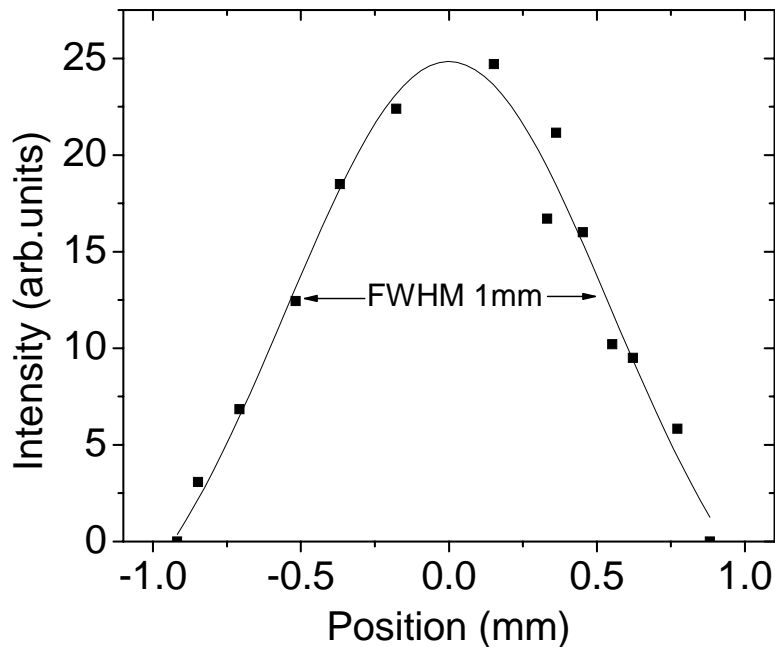
Fig 4.10 The transverse profile of the electron beam at the aperture stop slit. The measured data are indicated by the squares. Solid line is from a curve fitting.

slits of different size are shown in the Fig. 4.11.(a)-(d). Figure (a) was obtained when an aperture stop slit was not used, while (b),(c) and (d) were obtained when the aperture stop slits were 50 µm,25 µm and 5 µm. The corresponding results are summarized in Fig. 4.12.The results of these measurements clearly indicate that the resolution of the camera improves with the decrease in the beam size in the deflection plates. The temporal resolution of 280 fs by the conventional FWHM definition was obtained by using a 5 µm slit, as shown in the Fig.4.11.(d). With such a camera, two pulses separated by 333fs can be well resolved, as shown in Fig.4.11.(d). The ability to control the timing jitter, the transit time dispersion and technical resolution on the order of 100 fs allowed us to study the deflection aberration effectively. The deflection aberration was calculated from equation (1.11). The maximum deflection angle α and the axial velocity v_a are 0.015 rad and 1.6×10^{-3} µm/fs, respectively, for our camera. The calculated dispersions caused by
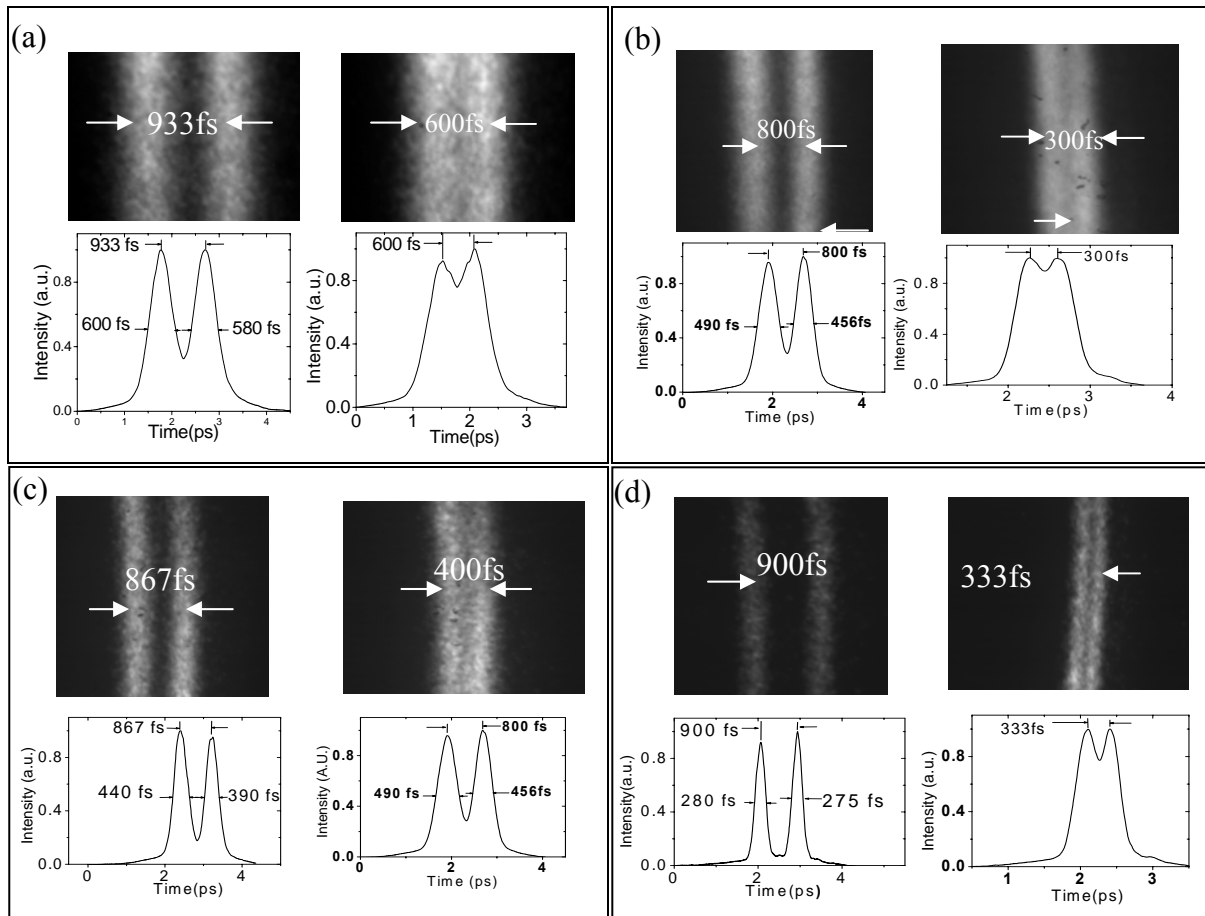
Fig 4.11 Dynamic images when the 2nd slit was set (a) open (b) 50 µm (c) 25µm (d) 5 µm

34

the deflection are 50fs and 500fs for a 5 μm width slit and a 50 μm width slit, respectively. The calculated result with a 50μm width slit is close to the measured value. However, the estimated dispersion due to a beam size of 5 μm is much better than the measures value. This is not surprising since for such resolution other limiting factors take over. The resolution Δt that includes all the previously mentioned effects can be estimated by equation (1.13). The estimated values are indicated in Fig.4.12. The calculated resolution agrees with the measured results.

Just as there is a compromise between the spatial resolution and $f^{\#}$ of a conventional optical imaging system, a compromise between the temporal resolution and the throughput of the streak tube must be made. The calculated relative signal intensities for various slit widths are shown in Fig.4.13. The calculation was based on the transverse profile of the electron beam shown in Fig.4.10 and the slit widths. As a comparison, the signal intensities were measured
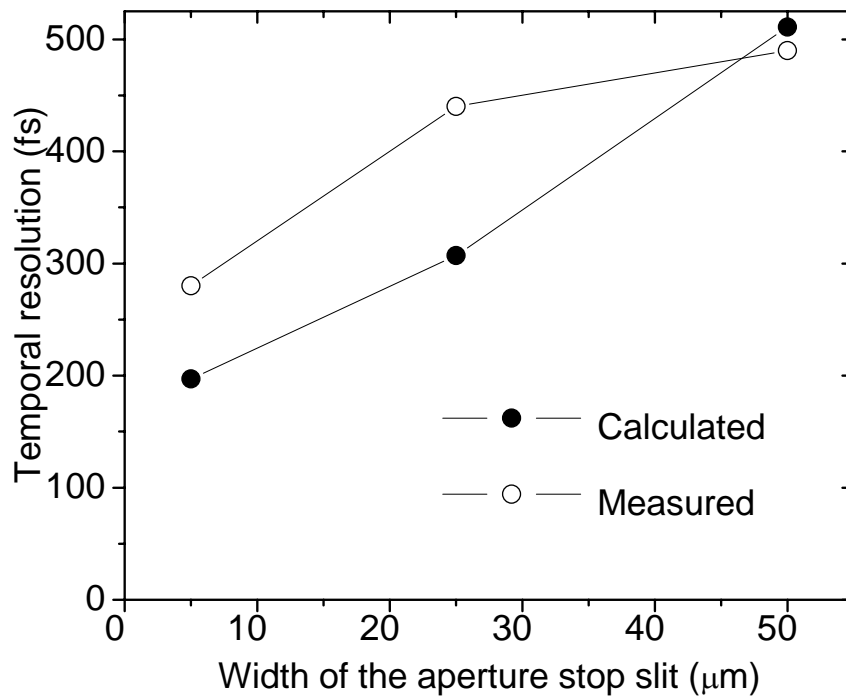
Fig 4.12 Comparison of measured temporal resolution with the calculations.

directly by changing the slit width, as shown in Fig. 4.13.The calculations are in agreement with the measurements. For an accumulative streak camera, a long integration time can compensate the reduction of the throughput.
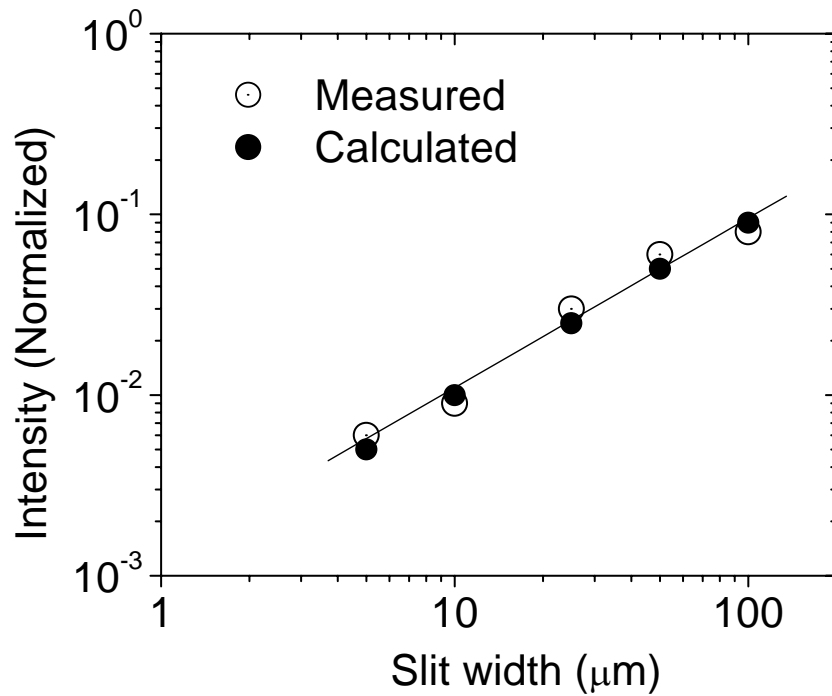
Fig 4.13 Measured and estimated signal intensities as a function of the width of the aperture stop slit. The intensity is normalized to that when the slit is removed. The line is for guiding the eyes only.

CHAPTER 5 - Conclusions

This work was devoted substantially to the design of an accumulative streak camera to improve the resolution. The novelty of our design consists of a uniquely designed slit mount that can be used to control the transverse beam size entering the quadrupole lens and the deflection plate. It is well known that the finite beam size of the electron beam inside the deflection plate causes deflection dispersion. We have shown experimentally that the deflection dispersion is the major limiting factor for streak cameras with resolution approaching 100fs. It is clear that the deflection aberrations can be reduced significantly by reducing the beam size in the deflection plates. With a 5 µm wide slit, resolution of the camera reached 280 fs in an accumulation mode. X-ray streak camera with such a high resolution can not only enhance the research capabilities at a third generation synchrotron facility, but will also impact the development and applications of the fourth generation x-ray source. The camera may also become an important diagnostics for the development of the fourth generation x-ray sources whose pulse duration is on the order of 100fs.

Better technical resolution requires higher scanning speed and a better focusing process. In order to increase the scanning speed of the camera, the time varying field from the switch and the deflection plates should be very fast. In this camera, this was accomplished by replacing lower bandwidth cable by higher bandwidth cable. Rise time of the driving field was reduced to 120ps from 150ps when 2GHz cable was replaced by 18GHz cables, which connects the meander type deflection pates. The scanning speed of the camera with this configuration was measured to be 2.8 times the speed of light.

The quality of focusing for the two different configurations of the quadrupole lenses was compared. The transverse image width (Δx) of 274 µm was obtained with the lens configuration satisfying $r_e = 1.9 r_o$, while 166 µm was achieved by modifying its geometrical configuration to $r_e = 1.14 r_o$, where $2 r_0$ is the diametrically opposite spacing between the quadrupoles and r_e is the radius of the quadrupoles. Consequently, those modifications produced the static image resolution 92 fs when a 5µm aperture stop was used. The value is quite encouraging to strive further toward breaking the limit of 100 fs dynamic resolution.

The measurement of the scanning speed at different cathode voltage shows that the scanning speed decreases with an increase in the cathode voltage (Fig.4.3). The result of this study suggests that attempt to reduce the transit time dispersion by increasing the cathode voltage in turn increases the technical resolution. In other words, an increased extraction field by reducing the space between cathode and the anode would give the better resolution than the same increased in extraction field by increasing cathode voltage. The resolution of 280 fs was demonstrated at $-$ 11kV, which corresponds to the extraction field 13.75kV/mm. It is therefore possible to push the resolution of this camera to 100fs by keeping the extraction field to 13.75kV/mm and reducing the cathode voltage to -7kV. This can be done by exchanging the currently installed 0.5 mm spacer with 0.25 mm spacer, which keeps anode and cathode 0.55 mm apart. The scanning speed within those parameters can still be expected to be 2.8 times the speed of light at the bias voltage $\pm$ 68V (Fig 4.4) applied to the deflection plates. The only obstacle to this scheme is the risk of arcing which may be overcome by improving the vacuum system. We hope that the streak camera with these settings therefore will fulfill our goal to study phonons with the time resolved x-ray diffraction method in near future which requires at least 100fs resolution.

In Chapter 6, I will describe how we used this streak camera to measure the pulse duration of grazing incidence pumped table-top Ni-like Ag and Cd transient soft x-ray lasers and its result.

CHAPTER 6 - A Test of The Streak Camera With XUV

The detailed descriptions of the design of the experimental setup for generating XUV photons will be presented in Chapter 9. In this chapter, an experiment to test the streak camera by using a newly designed setup as a XUV photon generator and the result of the experiment will be described. Since the energy spread of the photo-electrons varies from one photo-cathode material to the other, resolution of the camera also varies accordingly. A photocathode used for the UV illumination cannot be used for XUV illumination to generate photo-electrons. Therefore, the measurement of the resolution based on the UV test may not necessarily be the same if X-ray photons are used for the illumination with a different photocathode. Time resolved X-ray diffraction experiment will be our approach in the near future to investigate the ultrafast dynamics in the solid and the plasma in which the photocathode of the streak camera will be continuously illuminated by an X-ray beam. Therefore, the resolution of streak camera tested with X-ray, instead of that tested with UV should be used for the experiment.

6.1 Experimental Set-up

Schematics of the experimental setup to test the streak camera with XUV illumination is shown in Fig.6.1. XUV photons are generated by focusing a 1 Watt, 30 fs and 790 nm laser from the Kansas Light Source onto an argon gas target. An aluminum filter blocks the infrared beam and transmits XUV photons. The reflected photon beam from a gold mirror placed 45^0 to the beam direction is incident on a 1019 A^0 thick KBr photocathode film deposited onto a 1085 A^0 thick lexan film. As reflectivity of the gold mirror for the XUV energy range that we generate is 2% at an angle of incidence 45^0 (Fig.6.2), the number of photons which takes part in the photoelectric effect is very small. In order to increase photon flux, target pressure was set to the maximum phase matching pressure (describe in detail in Chapter 9).High negative voltage on a copper ring directly in contact with the photo-cathode accelerates the photo-electrons. As mentioned in Chapter 2 section 2.3, slit 1 and slit 2 are used to define the field of view and control transverse beam size respectively inside the quadrupole and the deflection plates. The

deflected beam is incident on a MCP and imaged on the phosphor screen. The GaAs switch and the deflection plates used to generate the time varying field are the same as described in Chapter 2.
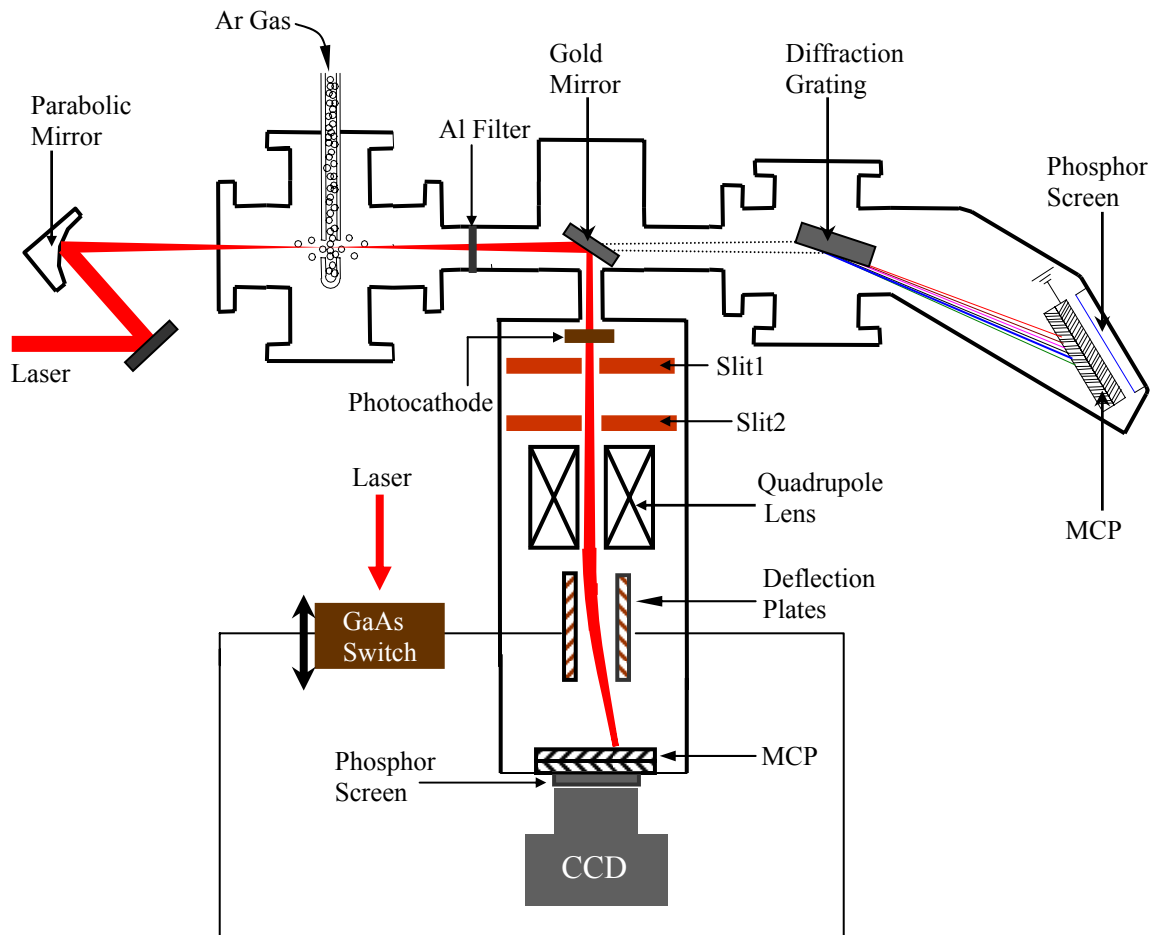
Fig 6.1 Experimental setup to test the streak camera with XUV illumination
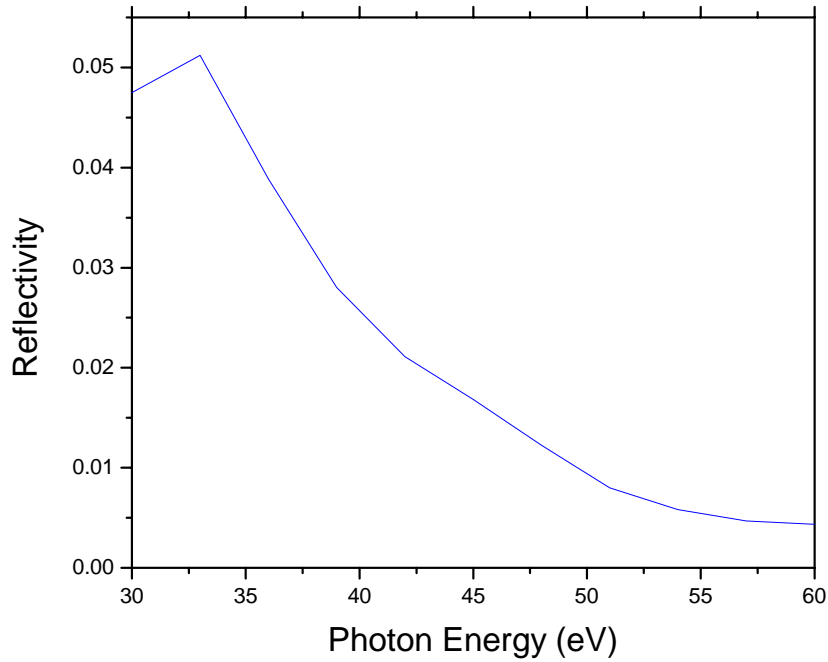
Fig 6.2 Reflectivity of gold for P-Polarized XUV beam at the energy range 30eV -60eV for the angle of incidence 45^0. The photon energy that we generate lies within this range. *Courtesy CXRO*.

6.2 Speed Calibration

10% of the total beam (1watt) was split with a beam splitter and incident on the photoconductive switch. The other 90% was used to generate XUV photons. By synchronizing
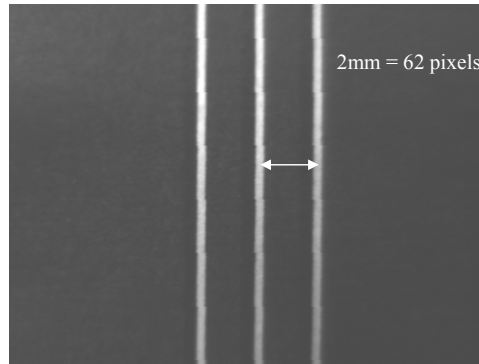
Fig 6.3 Line images of known separation (2mm) which corresponds to 62 pixels (0.032mm/pix).

the propagation of the time varying field and the arrival of the electron pulses precisely, deflection sensitivity was greatly enhanced. An 80 µJ of IR energy from the 10% splitter energy was used to impinge on the photoconductive switch to minimize timing jitter. A photoconductive
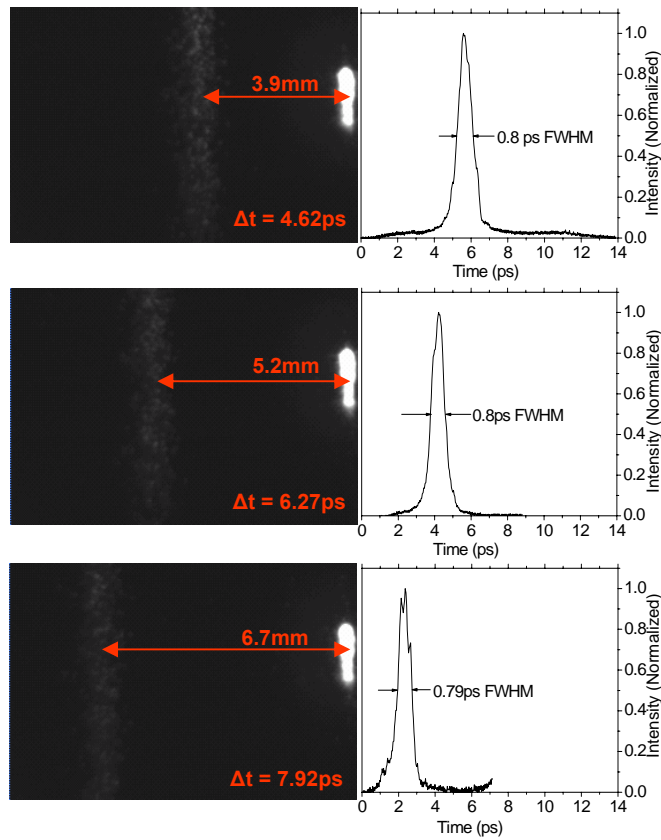
Fig 6.4 (i) Images swept by a GaAs switch as it was slid at the step of 0.5mm along the direction of incident laser. White spot on the right is image of the leaked photons through thin region of the photocathode. (ii) Line out of (i) with temporal width measured at FWHM.
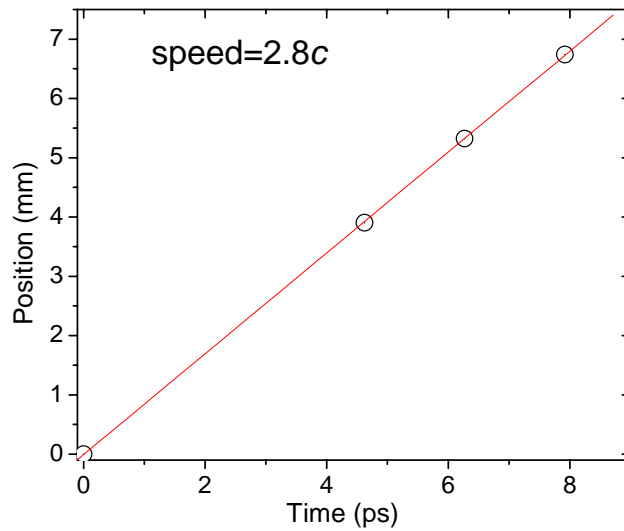
Fig 6.5A plot of the image position vs delay. Slope of the linear fit is the sweeping speed of the camera.

switch mounted on the rail was moved slowly along the direction of the beam, and the corresponding displacement of image from its initial position was recorded. Maximum displacement of image was found at the bias voltage ±68V for the same change in the position of the switch. The scanning speed of the camera with those setting was found to be 2.8 times velocity of the light, which is consistent with the value measured using Mach-Zehnder interferometer. The result of the measurement is illustrated in Fig. 6.4 and Fig.6.5.

6.3 Results and Conclusions

Fig. 6.6 is the static image obtained at the cathode voltage of -6 kV and the focusing voltage of 104 V. The image width at FWHM is 340μm and the corresponding temporal width is 0.4ps. The image was measured without introducing any slits on the beam path. The large reduction in the photon number caused by low reflectivity of the gold mirror (2%) prevented us from introducing a second slit to control the beam size. Only an accumulation of 1000 averaged frames integration can produce a better image quality with high signal to noise ratio. It is therefore clear from this measurement that the effect of dispersion is dominant in this measurement, which caused an image broader than the ideal image size (~2.1×25μm). Since the static image is the best possible resolution that the camera would have if all the other factors affecting the resolution were eliminated, the camera will never approach a resolution better than the static resolution. Fig. 6.4 is a set of dynamic images observed when the position of the GaAs
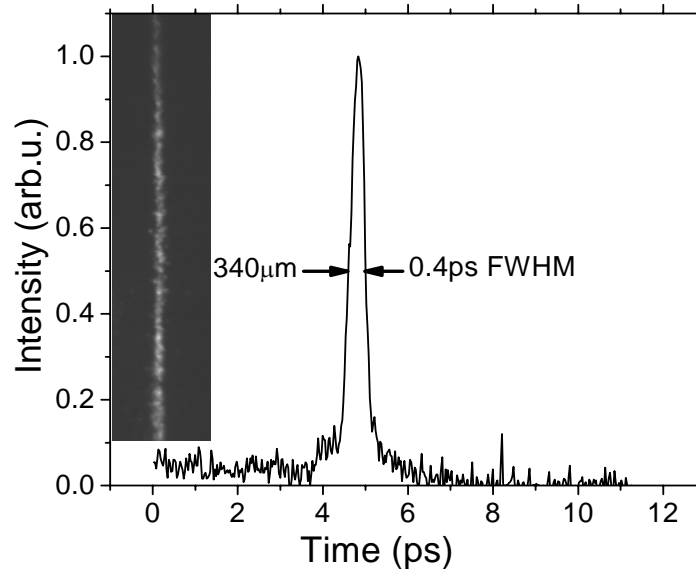
Fig 6.6 Static image obtained using XUV photons without second slit and its line out at -6kV cathode voltage.

photoconductive switch was changed at a step of 0.5mm. This change in the position of the GaAs switch corresponds to the change in delay time of 1.65 ps. The image was found to be swept at an average speed of 0.85mm/ps when the bias voltage to the deflection plates was set to ±68V. For each delay introduced to the switch, the temporal width of the image was measured 0.8ps full width at half maximum. Therefore, the resolution of the camera is 800fs at -6kV photocathode voltage without using the second slit.

As the pressure inside the camera elevated to ~ 10^{-7} torr from ~10^{-9} torr after it was installed into the HHG chamber, the camera had to be tested at the low extraction field of 4.6kV/mm in order to prevent arcing. The transit time dispersion for this operation is therefore very high. In addition to this, as application of the second slit was not possible for such low signal intensity, the effect of deflection aberration could not be minimized. Since the gold photocathode was replaced by a KBr photocathode to generate photoelectrons with XUV illumination, FWHM of the electron energy distribution after they are liberated from the photocathode surface was being increased by about 50%, which is proportional to the time of flight dispersion. It can therefore be concluded that those are the obvious reasons so far for having the resolution poorer than the resolution demonstrated using UV.

6.4 Future Work

As poor vacuum condition limited us from increasing the cathode voltage, focus of our work will primarily be on improving the vacuum in the near future. With this improvement, we would expect to be able to run the experiment at -10kV cathode voltage and~ 0.5mm separation between the cathode and anode. This would increase the extraction field by 77% and consequently, reduce the time of flight dispersion greatly. In order to increase the signal intensity, intensity of the photon beam has been increased by replacing flat mirror with a spherical gold mirror. This would of course break the barrier limiting the application of the second slit to reduce the beam size entering the quadrupole lens and the deflection plates. It is therefore not far from the future that we are likely to witness 100fs resolution, and will be able to investigate ultrafast dynamics in solid and the plasmas.

CHAPTER 7 - Pulse Duration Measurement Of The Soft X-ray

7.1 Introduction

There has been much effort done in the development of a source that produces intense coherent electromagnetic radiation at a wavelength as short as possible for the application. One example of a source is the synchrotron radiation, which can generate extremely bright and very short wavelength soft x-rays. However, due to the high cost and huge space required to build the source of synchrotron radiation, it has become less attractive for applications. Therefore, a compact and practical soft x-ray laser, which fits onto a normal optical table so called table top laser, is today's demand for routine application in science and technology. A few of the numerous advantages of table top x-ray lasers are studies in atomics physics, biological imaging, charatering and processing of the materials, and very high resolution metrology. It can not only open the ways to study nonlinear process in the field of nonlinear optics at ultrashort wavelength but also put forward an experiment on time resolved x-ray diffraction of biology, chemistry and in the medical diagnostics. There had been many records of new developments in science and technology in the past when a practical source of electromagnetic fields was available. It is therefore also not impractical to expect important scientific and technological breakthrough in the near future once a table top intense source of soft x-rays with shorter wavelength radiation is developed. Consequently, progress made in that direction led to remarkable success in the harmonic-up conversion in table-top laser system to generate radiation at wavelengths as short as 2.7nm [20]. Presently, rapid development in improving the conversion efficiency of harmonic conversion has been taking place in an attempt to make high brightness, high average power and high repetition rates routinely available. Although, much progress in harmonic conversion has been made, the conversion efficiency of x-ray generated from this technique must still be improved if it is to replace synchrotron radiation. Among several different techniques, the method of collisional electron excitation for example has been attempted to replace synchrotron radiation. Because of its low repetition rate, it could not provide good alternative to the synchrotron source. Recently, the technique of grazing-incidence-pumping proved to be a reliable method to generate an affordable table top source of intense and short wavelength soft

x-rays[34,35] for application. For wavelengths as short as 13.2nm, this configuration has achieved saturated laser operation at 5 Hz repetition rate with output average powers at the microwatt level. This technique, known as transient electron collisional excitation [36, 37] has an advantage over collisional excitation by having much larger population inversions under rapid transient excitation. These compact lasers have been recognized as a useful source for static and dynamic applications. It is however impossible to use these lasers for the dynamics application without having knowledge of their pulse duration. In this chapter the first experimental measurement of pulse duration of soft X-ray produced by transient electron collisional excitation will be presented.

7.2 Transient electron collisional excitation

Due to the large population inversion that can be achieved with relatively low laser pump energy, the transient electron collisional excitation scheme has been recognized as a promising approach to generate table top intense soft X-ray at low wavelength for the application. Compared to transition in the quasisteady state [38, 39], it has been reported that the gain coefficient is larger by 1-2 orders of magnitude in this scheme. In this scheme, plasma is heated very rapidly for only a short period of time. The process of heating occurs at a much faster rate than the rate at which relaxation of the excited state takes place. As collisional excitation occurs much more rapidly before the population redistribution takes place due to collisions, the upper level population becomes much higher. Overheating of plasma also increases the rate of the excitation of electron and reduces the rate of collisional mixing between the closely spaced active levels. Preferably, Ag target is chosen to generate plasma by heating, because 19 electrons out of 47 electrons of Ag can be removed from its shell to produce Nickel like electronic configuration (28). The nickel- like ions which are very stable, closed-shell and less or non-ionizable, therefore increase the relative abundance of the lasing ions during the plasma heating process. Fig.7.1 shows the simplified energy level diagram of Ni-like Ag illustrating the laser transitions. Two pump pulses of different pulse durations are used to populate the 4d upper level. The first one, called the pre-pulse, of longer pulse duration, is used to produce a sufficiently high abundance of lasant ions. Then the plasma undergoes hydrodynamic expansion, thereby reducing the electrical density gradients. The relatively higher intensity ($\sim 10^{15}$ W.cm^{-2}) and shorter duration of the picosecond pulse rapidly heats plasma to the temperature of the electron, which

corresponds to energy over 500 eV. In transient electron collisional excitation, population inversion is achieved as a result of the difference in the rate of excitation of the laser upper and the lower level.
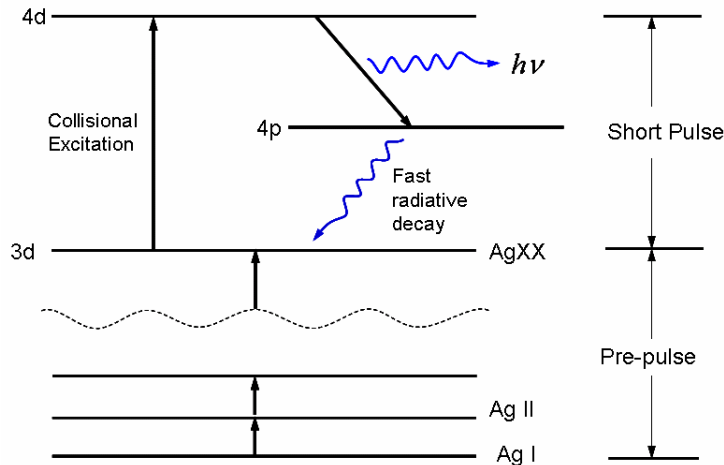
Fig 7.1 Simplified energy level diagram of Ni-like Ag

7.3 Experimental Set-up

A technique of grazing incident pumping (GRIP) used in CSU lab to generate a soft X-ray laser is described here briefly. An advantage of GRIP over other techniques is the great reduction in pump energy required to achieve the large gain. The GRIP method takes the benefit of refraction of the short laser pump in the pre-formed plasma to supply laser energy into the selected region with particular electron density where the population inversion takes place. A grazing incident angle was optimized to increase the path length and deliver maximum laser energy in the gain region of the plasma. This optimization is very important because if the grazing incident angle is larger, the short pulse will travel through the higher plasma density region thereby increasing the angle of refraction of the laser beam. Consequently, the pump beam will escape quickly from the gain region of plasma allowing very short time for the region to absorb pump energy. If grazing incident angle is small, pump beam will miss the region to be heated. It has been demonstrated that an angle of incidence between 14^0 and 23^0 with the target surface led to gain-saturation of a 5Hz repetition rate at wavelength 13.2 nm for Ni-like Cd [40, 41].

The CSU Lab generates 2 J, 120 ps laser at 5 Hz repetition rate. A 20% of the total output was used to create pre-formed plasma, while the rest was compressed to 6-8 ps. A 4 mm long polished slab target of lasing material (Ag or Cd) was irradiated by focusing, an uncompressed ~350mJ (120 ps) pulse to a 4.1mm×30 μm wide line at near normal incidence. This irradiation by
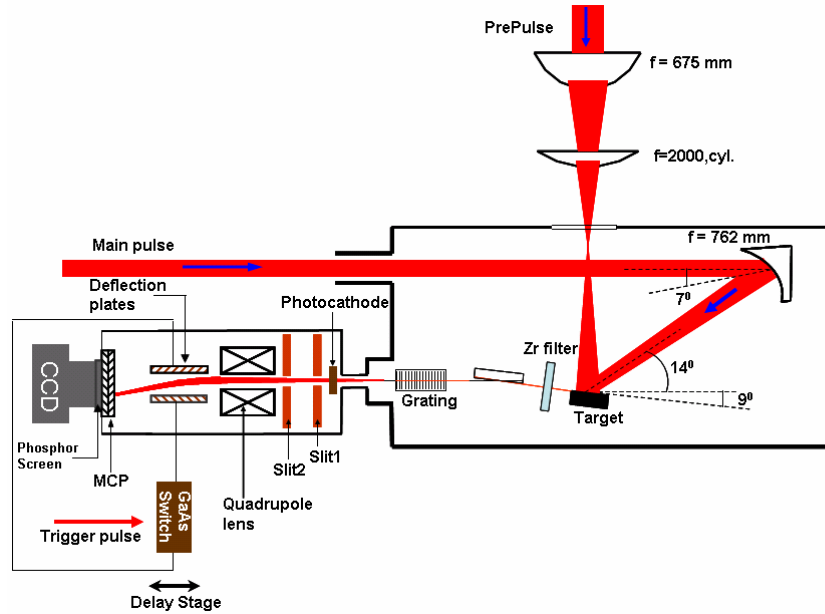
Fig 7.2 Schematic of experimental setup representing the measurement of the pulses duration of soft x-ray pumped at a grazing incident with x-ray streak camera.

the pre-pulse creates the plasma. This uncompressed 120 ps pre-pulse was preceded by 5.6 ns by ~10 mJ pre-pulse of the same duration (120 ps) in order to allow plasma expansion to reduce the density gradient. The ~ 10 mJ pulses, which are lagging 5.6 ns behind the main pulse, help enhance the soft x-ray laser output. After a few hundred picoseconds of irradiation at normal incidence, the plasma was heated rapidly by a pulse of ~1J and 6-8 ps impinged at a grazing incident angle of 23^0. A parabolic mirror of focal length 76.2 cm placed at 7^0 to the normal incidence was used to focus the short pulse into a line focus of the same size. The reason for this off axis placement of the parabolic mirror is to produce an astigmatic focus. The astigmatic focus was further elongated as it is incident on the target at the grazing incident angle. A schematic of the setup is shown in Fig.7.2. A pair of adjustable cylindrical mirrors placed in front of the compressor allows keeping the astigmatic focus to 4.1mm FWHM length.

Filtering of the plasma emission was performed with a 1500 Å thick filter. A borosilicate flat reflects the emission at the grazing incidence and incident on a 1200 l/mm gold-coated variably spaced ruling spherical grating. Dispersed light from the grating is then incident on the 1019Å thick KBr photocathode film deposited onto a 1085 Å thick lexan film. Photocathode generates photoelectrons as explained in the section 6.1.

7.4 Calibration of Streak Camera

The streak camera was tested using the Kansas Light Source with the parameters set exactly the same as that used to measure the pulse duration of the soft x-ray in Colorado State University (CSU). Since, one terminal of the bias supply was disconnected while the pulse duration of the soft x-ray was measured in the CSU lab, the speed of the streak camera was also calibrated under the same conditions. When the gap between the cathode and anode was 1.3 mm and the acceleration voltage was -7 kV, the speed of the camera was measured to be 0.53 µm/fs with one of the bias terminals disconnected. Fig. 7.3 shows the static image width obtained using a high harmonics pulse of 30 fs pulse duration. A width of 288 µm corresponding to temporal
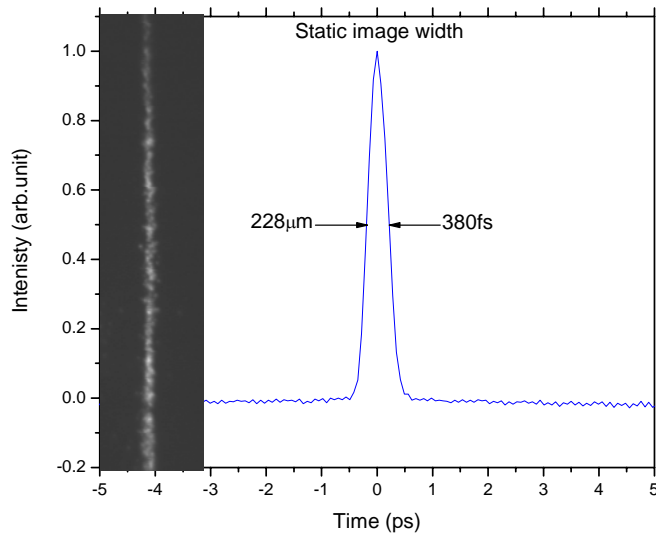
Fig 7.3 Static image width obtained without second slit at -7kV acceleration voltage.

resolution 380 fs implies that the temporal resolution of the dynamic image cannot be better than 380 fs in the absence of the second slit. Corresponding dynamic resolution obtained are illustrated in Fig. 7.4 and Fig.7.5. Fig. 7.4 is the line out of six streaked images each obtained by

operating with the accumulation of 100 average frame, 60V bias voltage and ±104 V focusing voltage of. Fig. 7.5 is the average of all six images, which gives the measured FWHM temporal width of 1.8 ps. In conclusion, the resolution of the camera without the supply from one of the bias terminal can reach 1.8 ps at the accelerating voltage -7kV.
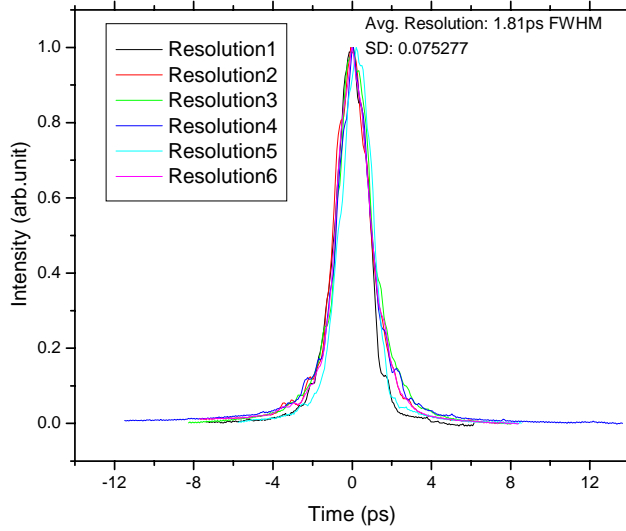
Fig 7.4 Line out of six dynamic images obtained at focusing voltage ± 104 V and +60 V bias
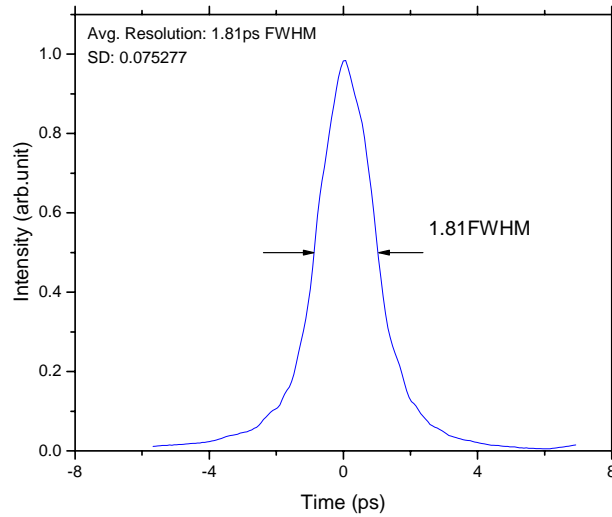
Fig 7.5 Average FWHM of Fig. 7.4

7.5 Results and Discussion

In order to measure the pulse duration of a soft x-ray produced by pumping at the grazing incidence of a short pulse, jitter due to laser fluctuation was minimized by operating the photoconductive switch at the saturation energy of 0.2mJ and 50 fs duration Ti-sapphire laser. The soft x-ray generated from the Ni-like Ag target was illuminated on the photocathode. A 350 mJ pre-pulse and short pulse of 6.7 ps was delayed by 250 ps in order to create maximum soft x-ray
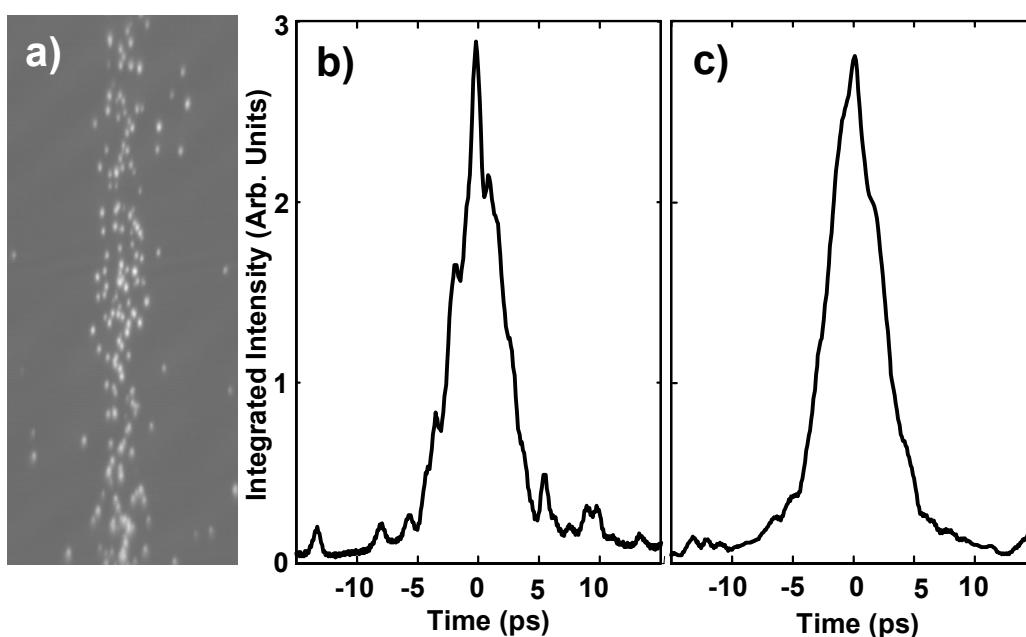
Fig 7.6 (a) Streaked single-shot image of 13.9 nm from x-ray streak camera (b) Line out of the image (a) and (c) the line out from the average six shots with FWHM 4.9 ps.

laser output energy. The image in Fig 7.6 is a single streak image when the Ni-like Ag target was irradiated at optimum pumping conditions for maximum soft x-ray laser output pulse energy generation. Fig.7.6 a) is an image of a laser pulse streaked along the horizontal direction by the streak camera at -7kV and ±104 V accelerating and focusing voltage respectively. The CCD image of each dot on the phosphor screen of the streak camera is an amplified single photoelectron from the internal microchannel plates. Fig .7.6 b) is the line out of an image. FWHM of (4.9 ± 1.0) ps obtained from the line out of average six shots shown in Fig.7.6 c) conclusively provides measured value of the pulse duration. The measured pulse duration as a

function of delay between the pre-pulse and the short pump pulse, along the full range of operation of the laser [42] shown in Fig. 7.7 is also consistent with this measurement. In the measurement, within the range of 150 and 450ps delays, the pulse duration was almost constant.
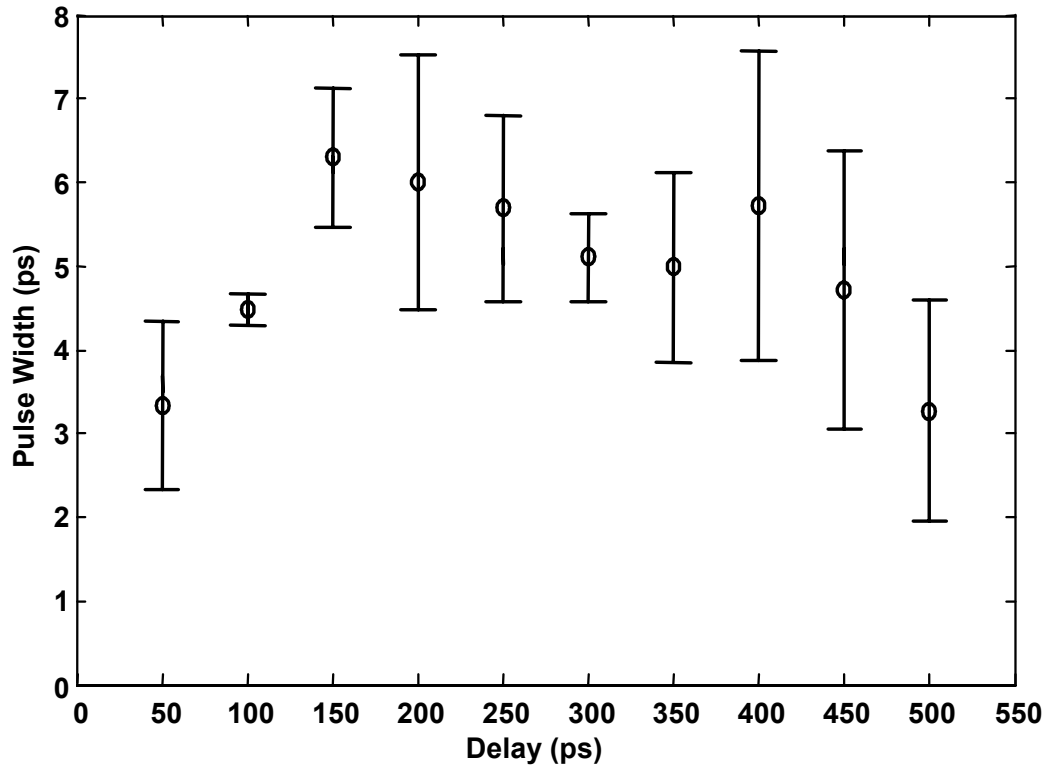
Fig 7.7 Plot of measured pulse width of 13.9 nm Ni-like Ag laser as a function of time delay between the 350mJ pre-pulse and 1J, 6.7 ps pump pulse.

Variation outside this range however is caused by a shorter duration of the gain for nonoptimum delays. The x-ray streak camera was also used to measure pulse duration of the soft x-ray pulse generated from the Ni-like Cd target at 13.2 nm by impinging short pulse at the optimized grazing incident angle.Fig. 7.8 a) and b) shows a single temporal profile and average of six streak-camera traces respectively obtained when rapid heating short pulse of 6.7 ps was delayed 100 ps behind the pre-pulse of 120ps. The FWHM measurement of the average line out of the
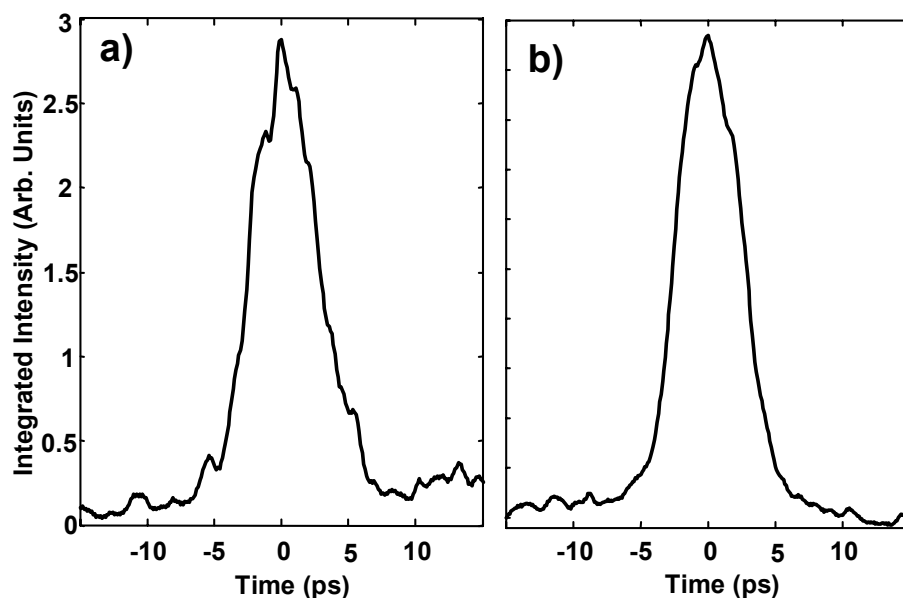
Fig 7.8 Line out of (a) single shot streaked image (b) average of six shots with FWHM 5.2 ps of 13.2 nm Ni-like Cd soft x-ray laser pulse. The target was pumped by a 1J and 6.7 ps pulse by impinging at grazing incidence angle of 23^0 with the target surface. The pump pulse was delayed by 100 ps from the pre-pulse.

image gives the pulse duration of (5.5 ± 0.3) ps of the x-ray laser from 13.2 nm Ni-like Cd grazing-incidence x-ray laser.

7.8. Conclusions

We demonstrated that the x-ray streak camera we designed is capable of measuring the pulse duration of the x-ray. The experimentally measured pulse duration of the soft x-ray with the streak camera agrees with the prediction made by the model and the measurement made by changing the delay as a function of the pulse duration (Fig. 7.7). We measured the pulse duration of emitted from Ni-like Ag and Cd grazing-incidence laser to be ~5ps. Measurement of this kind is very essential for dynamic applications of the x-ray source, which can lead to new scientific and technological breakthroughs. Application of the camera for the various sources of x-ray at different wavelengths proved that the camera has potential capability for serving as a detector in the study of ultrafast dynamics in the fields of physics, chemistry, biology and medical science.

CHAPTER 8 - High-Order Harmonics

8.1. Introduction

In this chapter, I will present an investigation of harmonic generation of soft x-rays using an intense ultrafast laser. It has been demonstrated that harmonic emission, which takes place upon interaction of a gas medium with an intense and ultrashort laser pulse, lies in the extreme ultraviolet (XUV) and soft x-ray spectral range. Typically, high harmonic emission appears with three distinguishable regions in the spectral domain; a) a small region where harmonic intensity drops rapidly, b) then followed by an approximately constant and extended intensity region so-called plateau, and c) a cut-off where the plateau disappears abruptly (Fig.8.1). The high order harmonics generation (HHG) consists of a train of attosecond pulses, which has been found to be
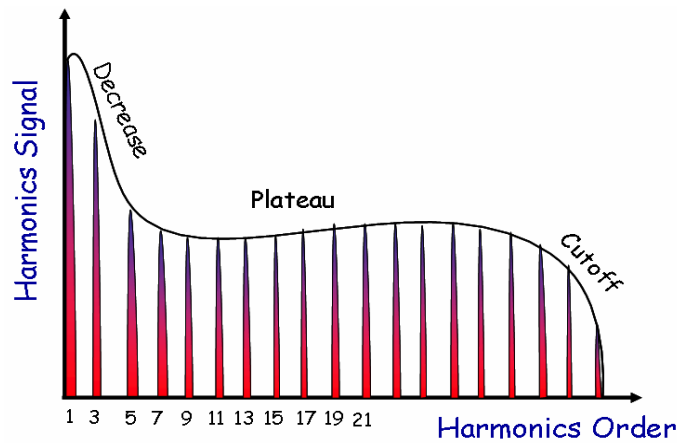
Fig 8.1 Typical spectrum of high harmonics as a function of the harmonic order $\left(q = \dfrac{\omega_q}{\omega_0} \right)$.

dependent on time and the frequency of the driving laser pulse. Another feature to note is that the HHG spectrum consists of lines separated by twice the fundamental frequency of the laser field (ω_0), and only odd harmonics are present. Highly coherent emission with the requirement of moderate pump-energy makes high harmonic emission a promising source of XUV with the

possibility of controlling an attosecond pulse train as well as individual harmonics by skillfully managing the driving laser field.

8.2. Harmonics Generation And Ionization

It was after Harris [48], who first noted that harmonic generation and ionization are linked together, that it was realized that better knowledge on ionization is required to gain insight into the problem of harmonic generation. An explanation harmonic generation had been attempted to explain with the knowledge of perturbation theory before McPherson [49] and Ferry [50], who obtained the 17th order in Ne and 33rd order in argon respectively. As both persistently observed the existence of an extended plateau out to a cutoff and did not find a decrease in harmonic intensity with increasing harmonic order, which runs contrary to perturbation theory, the perturbation theory has been abandoned to explain the harmonic generation.

In a strong laser field, the number of photons required to ionize atom increases for an atom with a given ionization potential. The extra energy for the ionization in the strong electric field comes from the amount required to introduce an ionized electron into the applied field. This requirement of extra energy can be attributable to the Stark shift of the Rydberg and continuum states due to the presence of the strong time varying field $E\cos\omega t$, which can be given by the electron ponderomotive energy U_p expressed as

$$U_p = \frac{e^2 E^2}{4m\omega^2}$$
(8.1)

The ponderomotive energy U_p is defined as the cycle-averaged kinetic energy of a free electron oscillating in a laser field at frequency ω. U_p may be calculated as $U_p = 9.34 \times 10^{-14} I \lambda^2$ in eV when I and λ are expressed in W/cm^2 and μm respectively. Because of the energies of the Rydberg and the continuum states which shift upward relative to the lower bound state by an amount equal to U_p, the ionization potential, $I_p(I)$, also scales up in the strong field with the relation $I_p(I) \approx I_p + U_p$,where I_p is the ionization potential of the field-free initial energy state. In other words, the minimum number of photons necessary to ionize an atom scales up with the integer multiple of $U_p / \hbar\omega$ in order to counterbalance the shift in ionization potential in the strong field. This ratio $U_p / \hbar\omega$ is the parameter which determines whether or not perturbation theory breaks down. The different regimes of the multiphoton process can be identified from the

values of three important quantities: I_p, U_p and $\hbar\omega$. Three different regimes determined by the relations a) $I_p > \hbar\omega > U_p$, b) $I_p > U_p = \hbar\omega$, and c) $U_p \geq I_p \gg \hbar\omega$ are defined as a) perturbative regime, b) ATI regime, and c) tunneling regime respectively. In order to remain in the tunneling regime according to Keldysh [51], the laser frequency should be low. He defined tunneling time τ as the ratio of the barrier thickness $x_0 = I_p/eE$ and the average velocity of the electron, $V = \sqrt{I_p/m}$, which boils down to the parameter known as the Keldysh parameter γ given by

$$\omega\tau = \gamma = \sqrt{\frac{I_p}{2U_p}} \tag{8.2}$$

As the field varies very fast for $\gamma \gg 1$, ionization through tunneling never takes place under that condition. However, ionization takes place through the process known as the multiphoton process for values γ greater than unity. If the field changes very slowly such that $\gamma \ll 1$, ionization takes place through tunneling. Ionization through tunneling dominates when the intensity of the laser of wavelength 800 nm exceeds 10^{14} W/cm^2. As the laser intensity increases further, the barrier potential suppress below the ground state. Electrons under this condition no longer remain bound and can be ionized very easily. This process of ionization is called over-the-barrier ionization. The threshold intensity for over-the-barrier ionization can be calculated by the relation given by [52]

$$I\left(\frac{W}{cm^2}\right) = 4 \times 10^9 \times \frac{I_p^4(eV)}{Z^2} \tag{8.3}$$

where Z is the charge state of an atom.
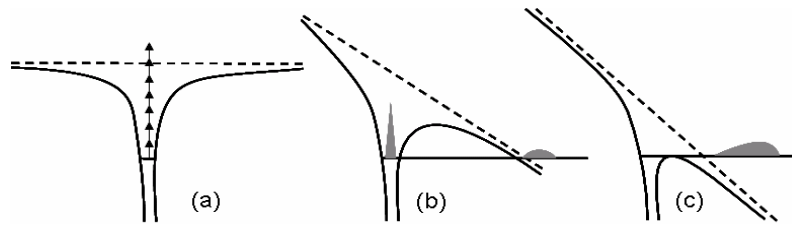
Fig 8.2 Schematic representation of ionization through the process of a) multiphoton, b) tunneling, c) Over–the-barrier ionization

In our case, we use a laser of 0.8Watt, 30 fs pulse duration at 1kHz repetition rate and 0.8 μm central wavelength to ionize argon. The ionization potential I_p of argon is 15.75 eV, which gives ponderomotive energy Up = 70 eV at 2mm from the focal spot. Keldysh parameter γ for these values from equation (8.2) gives 0.33, which implies that the ionization process takes place through tunneling ionization at those parameters. As long as the ionization process lies in the tunneling regime, the ionization yield for different laser intensities can be calculated from the ADK model. According to the model, ionization takes place only in the fraction of an optical cycle when an intense laser interacts with an atom. The average ionization rate over one complete cycle can be calculated as follows.

$$\text{Rate(t)} = R_c \left[\frac{2(2E)^{\frac{3}{2}}}{|F_0(t)|} \right]^X Exp \left[\frac{-2(2E)^{\frac{3}{2}}}{3|F_0(t)|} \right] fs^{-1} \tag{8.4}$$

Where for angular frequency ω_0, wave length λ_0, pulse width (FWHM) τ_0 and peak intensity I_0, $F_0(t)$, the time dependent electric field amplitude in atomic unit is given by

$$F_0(t) = 5.338 \times 10^{-8} \times \sqrt{I_0} \times \left[Exp[-2\ln(2) \times \left(\frac{t}{\tau_0} \right)^2 \times Cos(\omega_0 t)] \right] \tag{8.5}$$

Since the electronic structure for Ar is $1s^2 2s^2 2p^6 3s^2 3p^6$, the valence electron is in p orbital. Hence, defining quantum numbers for the ionization of the outer most electron which is on p orbital, $l = 1$, $m = 0$ and ionization potential $I_P = 15.76$ eV, which is equivalent to $I_P/27.212$ in atomic unit. If we consider ionization from the ground state to the 1st ionization state then ionization state Z_s can be written as $Z_s = 1$ and effective principal quantum number n_s as

$$n_S = \frac{Z_s}{\sqrt{2E}} \tag{8.6}$$

Where E is the ionization potential in atomic unit i.e. $E = I_P/27.212$. We can calculate effective orbital quantum number l_S from expression (8.6) using the relation $l_S = n_S - 1$. Further more, R_c in equation (8.4) is given by,

$$R_c = \frac{Cnl \times E \times Glm}{2.4189 \times 10^{-2}} \tag{8.7}$$

Where,

$$Cnl = \frac{2^{2n_s}}{n_s\,\Gamma(n_s + l_s + 1) \times \Gamma(n_s - l_s)} \quad \text{and}$$

$$Glm = \frac{(2l + 1) \times (l + |m|)}{2^{|m|}\,|m|! \times (1 - |m|)!} \quad \text{and } X \text{ is given by}$$

$$X = 2\,n_S - |m| - 1$$

Which gives $R_C = 295.621\,fs^{-1}$ from (8.7)

.
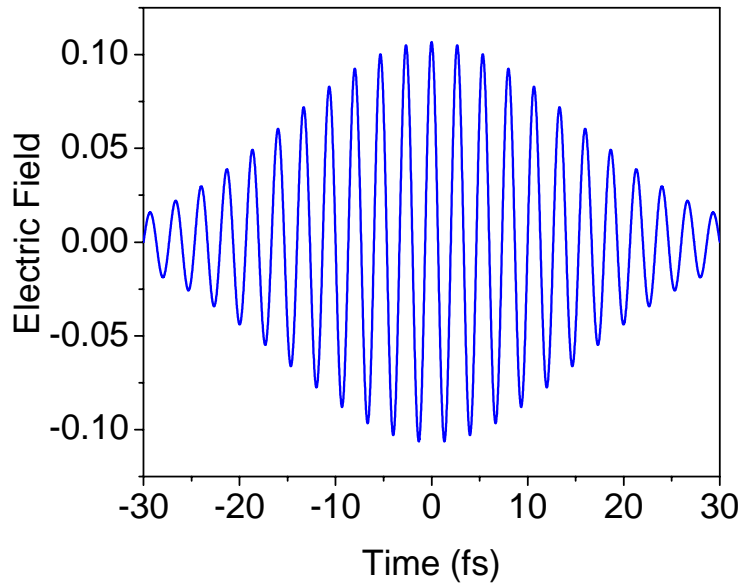
Fig 8.3. Laser field of pulse duration 25fs in atomic unit
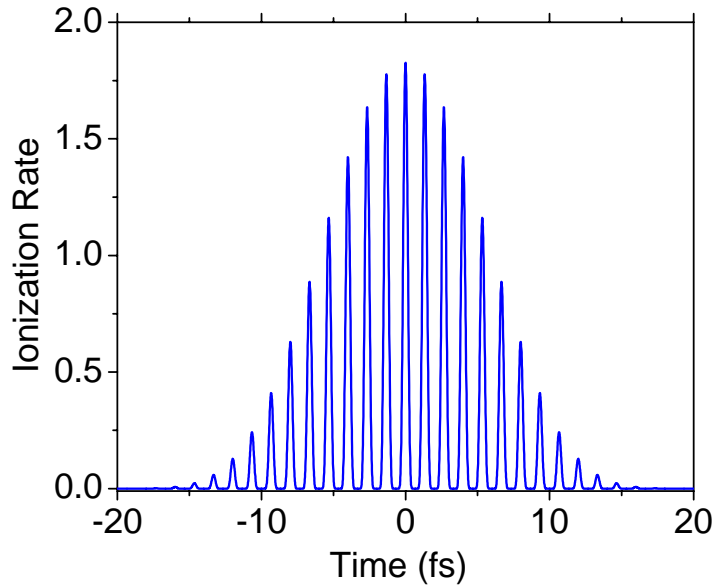
Fig 8.4 Ionization rate in argon in fs^{-1} due to laser field given in fig.8.3

Fig.8.3 is the plot of laser field in atomic unit for $\tau_0 = 25$ fs, $\lambda_0 = 0.8\,\mu m$ and Fig 8.4 is the corresponding ionization rate in argon in fs^{-1} unit due to the field given by the expression in (8.4) Ionization probability $P(\tau)$ from the expression (8.4) can be written as,

$$P(\tau) = 1 - Exp[\int_{-T_{max}}^{t} Rate(\tau)d\tau] \tag{8.8}$$

Where T_{max} is the time window for the calculation. For the calculation in Fig.8.5, value of T_{max} has been chosen 30 fs in order to include all the values of ionization probabilities within the pulse of duration 25fs.

For fixed pulse duration, the probability of ionization scales up with the intensity up to a certain value. Since the ionization probability of an atom cannot exceed 1.0; a high intensity laser can fully ionize the atom before the pulse is over. We define the intensity as the saturation intensity at which the ionization probability reaches 98%. At this intensity all the neutral atoms are used up .Fig. 8.5 shows the ionization probability for argon at the intensity 4×10^{14} W/cm^2 and 6×10^{14} W/cm^2. At intensity 4×10^{14} W/cm^2 ionization process just saturates at the peak of the electric field while at 6×10^{14} W/cm^2 saturation occurs before reaching the peak field. In order to
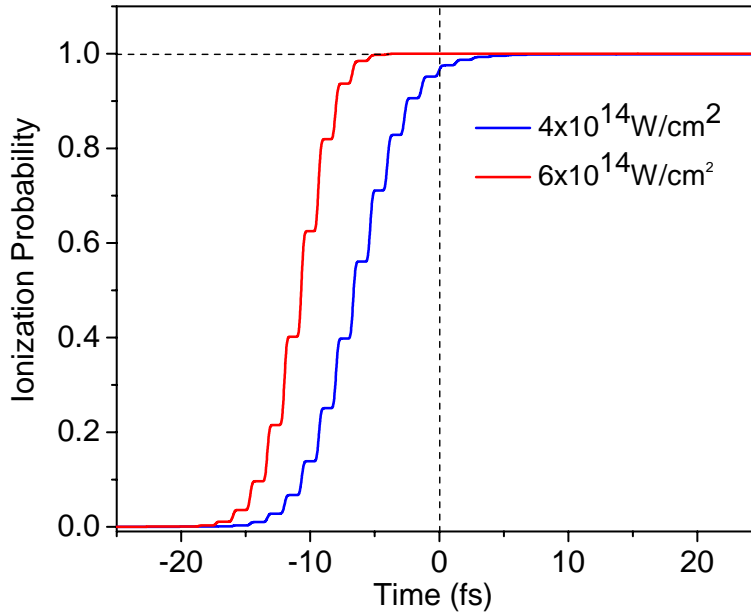
Fig 8.5.Ionization probability of argon atom at intensities 4×1014 W/cm2 (blue curve) and 6×1014 W/cm2 with laser field of duration 25fs.

allow the process to take place in the tunneling regime without exceeding saturation intensity, the intensity was maintained between those two intensities, while working with the long pulse of duration 30fs. Increasing the probability of ionization does not increase the high order harmonics efficiency, but decrease the signal intensity due to plasma defocusing as it increases density of plasma in the medium. The measured diameter of the focal spot from this pulse through the z-scan technique is shown in Fig. 8.6. The focal spot diameter can be estimated from the value of FWHM obtained from the plot of intensity as a function of space which is 74 μm in Fig. 8.6 (b). For a laser of 400 μJ, 30fs and 1kHz, peak intensity is $\sim 7 \times 10^{14}$ W/cm^2 ($\gamma = 0.4$) at the focus. However, at 2mm from the focus and considering gas density, intensity is less than the saturation intensity of Ar gas.
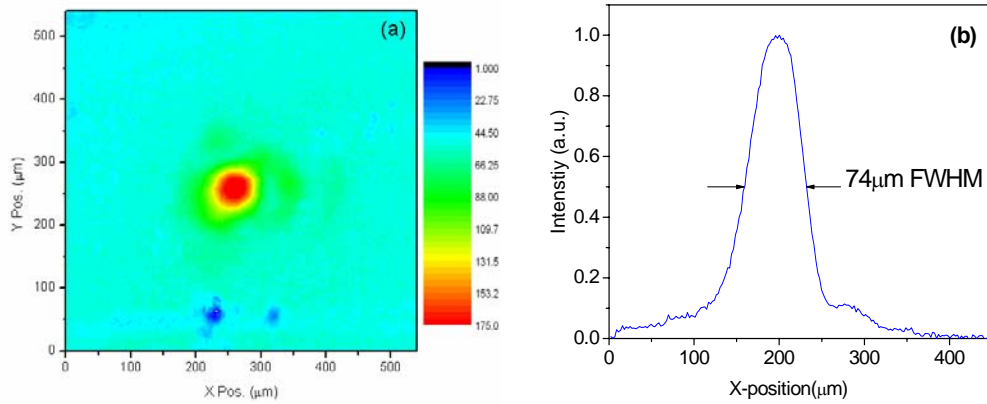
Fig 8.6 (a) CCD image of the focal spot, (b) the lineout of (a) with 74 μm FWHM.

8.3 Physical Picture Of High Order Harmonic Generation

The high order harmonic process is a very complicated process which provides no useful insight if one tries to explain it in terms of perturbation theory. It was however realized that the harmonic generation process has something to do with how an electron returns to the ground state. Although an explanation for high order harmonic generation requires quantum mechanical treatment, it can also be well understood from the simple semi-classical theory known as the simple man model[53,54] as long as the process takes place in the tunneling regime constrained by $\gamma \ll 1$ in equation (8.2). In this model, also popularly known as the three steps model, an atom is treated as an ionic core surrounded by electrons. As the atom is irradiated by a strong

laser electric field, the Coulomb barrier created by the ionic core is suppressed giving rise to the probability for the electron to escape from the barrier by tunneling. The escaped electron, the so-called free electron, accelerates in the laser electric field. As the laser field is oscillating, there is another probability that the electron can return depending on the phase of the laser field at the instant of its birth. The returning electron can either scatter or recombine with the ion core. The former produces a high energetic free electron; and the latter emits high-order odd harmonics of the fundamental. Schematics of the suppressed potential barrier of the ion core and the re-collision of the tunneled electron after the laser electric field changes its sign are illustrated in the Fig.8.7. The probability of ionization through tunneling is given by relation (8.8). The tunneling
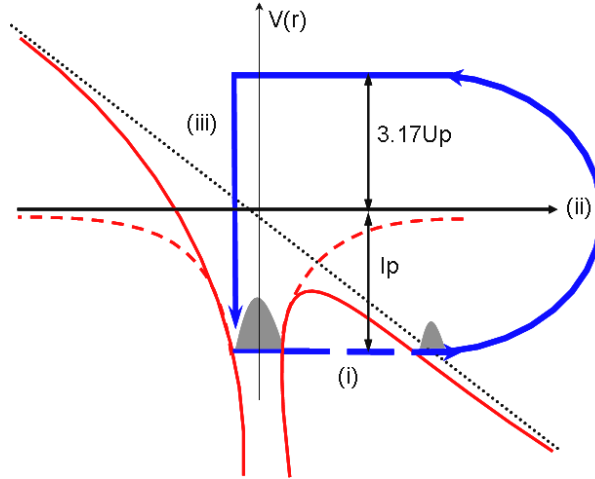
Fig 8.7 Schematics of the three steps of HHG: (i) Ionization; (ii) acceleration by the electric field; (iii) radiative recombination

probability of the electron depends on the ionization potential Ip and the thickness of the barrier. The barrier width of the potential in turn depends on the field strength of the laser electric field $E = \sqrt{2I/\varepsilon_0 c}$. The three steps model allows us to calculate the cutoff energy of the harmonics, expressed as

$$\hbar \omega_c = I_p + E_{max} \tag{8.9}$$

where E_{max} is the maximum kinetic energy of an electron when collision occurs. E_{max} can be estimated by treating the electron classically after it tunnels through the barrier. Once the

electron is freed from the strong core attraction, its classical equation of motion in atomic units (e=1 and m=1) can be written as

$$\frac{d^2 x}{d t^2} = E_0 \cos(\omega t) \tag{8.10}$$

Integrating twice gives the equation of motion for the velocity

$$v(t) = \frac{E_0}{\omega} \sin \omega t + v_0 \tag{8.11a}$$

$$x(t) = -\frac{E_0}{\omega^2} \cos \omega t + v_0 t + x_0 \tag{8.11b}$$

At time $t = t_0$, time during the cycle, when the electron is born, $v(t_0) = 0$, which leads to the electron drift velocity given by,

$$v_0 = -\frac{E_0}{\omega} \sin \omega t_0 \tag{8.12}$$

Hence the velocity of the electron at any time t can be written as

$$v(t) = \frac{E_0}{\omega} \left(\sin \omega t - \sin \omega t_0 \right) \tag{8.13}$$

At $t = t_0$, time during the cycle the electron is born, $x(t_0) = 0$, which will yield

$$x_0 = \frac{E_0}{\omega^2} \cos \omega t - v_0 t_0 \tag{8.14}$$

Hence the electron position at any time t can be written as

$$x(t) = \frac{E_0}{\omega^2} \left(\cos \omega t_0 - \cos \omega t \right) + \frac{E_0}{\omega} (t_0 - t) \sin \omega t_0 \tag{8.15}$$

Now we are in a position to evaluate the kinetic energy when the electron is driven back to the ion by the field, from equation (8.15), for which we can impose the boundary conditions for re-collision time $t_r > t_0$ and $x(t_r) = 0$. It immediately follows that

$$\cos \omega t_0 + \omega t_0 \sin \omega t_0 = \cos \omega t_r + \omega t_r \sin \omega t_0 \tag{8.16}$$

where t_0 and t_r are the birth time and the return time respectively. We can simplify equation (8.16) by assigning Φ_0 and Φ_r for ωt_0 and ωt_r respectively which gives

$$\cos \Phi_0 + \Phi_0 \sin \Phi_0 = \cos \Phi_r + \Phi_r \sin \Phi_0 \tag{8.17}$$

For fixed value of birth phase Φ_0, we can determine return time t_r by solving equation (8.17) graphically. Fig. 8.8. shows the plot of return phase Φ_r as a function of release phase Φ_0. As seen from Fig.8.6., no re-collision occurs before the 0^0 angle, which corresponds to the peak of the electric field. In other words, if an electron is born before the optical field reaches maximum, no re-collision takes place. The maximum energy that can be converted to a photon
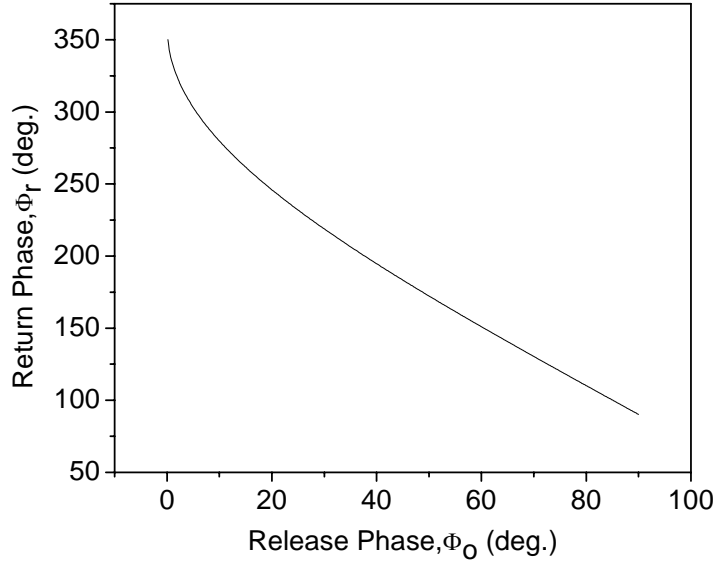
Fig 8.8 Re-collision phase Φ_r as a function of birth phase, Φ_0
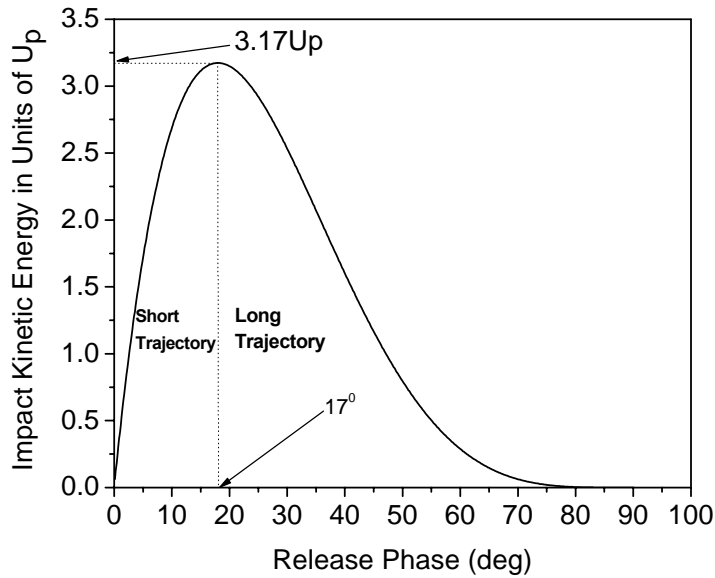
Fig 8.9 Kinetic energy of the electron at the recollision as a function of the release phase

should be the kinetic energy of the electron near the ion. It is straightforward from expression (8.13) that the kinetic energy at the return is

$$K.E. = \frac{1}{2}v(t_r)^2 = 2U_p(\sin\Phi - \sin\Phi_0)^2 \qquad (8.18)$$

Where $U_P = E_0^2/4\omega^2$ is the ponderomotive energy .

Clearly from Fig. 8.9, the maximum kinetic energy that the electron can have is 3.17 U_P when it is born at phase 17^0. It then turns out from equation (8.9) that the cutoff energy is

$$\hbar\omega_c = I_p + 3.17U_p \qquad (8.19)$$

Since the saturation intensity of Ar for a 30 fs Gausian pulse at 800 nm is 4.6×10^{14} W/cm^2, cutoff energy for Ar is 102 eV from (8.19), which corresponds to harmonics order 68 . A noteworthy point in Fig.8.6 is that there is no value of energy plotted for $\Phi_0 < 0$, as the electron drifts away from the ion and never returns to the origin. Electrons on the other hand released at or after the peak of the driving field return with the energy defined by the plot shown in Fig.8.9.
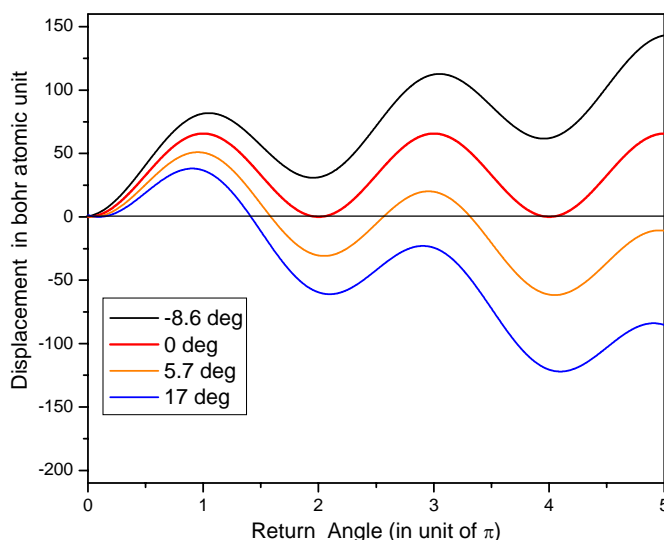
Fig 8.10 Classical trajectory of electron as a function of release phase angle

The factor 3.17 for the peak value of energy in expression (8.19) is the same as that which appeared in Becker's model [55], in which he treated the electron trajectory quantum mechanically. It is therefore not far from reasonable to say that Becker's model is the quantum-

mechanical analog of the classical problem. Another point to note in Fig.8.9 is that there are two phase angles where electron will return to the origin with the same kinetic energy. An electron which returns with the energy less than 3.17U_p has two trajectories, the so-called long and short trajectories. Fig. 8.10 shows the trajectories of an electron when it is released with zero velocity for different release phase Φ_0. The calculation was made for a laser of 800 nm, intensity $\sim 10^{14}$ W/cm^2 and ionization potential 15.75 eV. The Keldesh parameter γ is 0.6. From the classical model, if the electron releases at time t_0 such that the release phase $\Phi_0 < 0$, the electron will never be driven back to its initial position. In order for the electron to re-collide or re-scatter, the electron should therefore release at phase angle $\Phi_0 > 0$. The maximum excursion distance can be estimated by imposing the condition $v(t_m) = 0$ in expression (8.13), which leads to

$$\Phi = \pi - \Phi_m \qquad (8.20)$$

where t_m is the time required for an electron to reach the maximum distance. Hence, equation (8.15) boils downs to

$$x_m = \frac{E_0}{\omega^2}[2\cos\Phi_0 + (2\Phi_0 - \pi)\sin\Phi_0] \qquad (8.21)$$

where x_m is the maximum excursion and Φ_0 is the birth phase angle. Fig.8.11 shows the excursion distance of the electron at wavelength 800 nm and intensity 4×10^{14} W/cm^2 at different release phase angles.
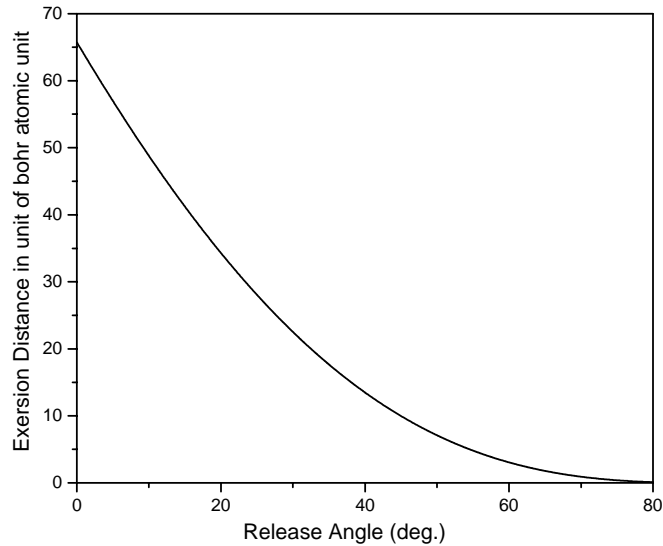
Fig 8.11 Excursion distance of the electron for trajectories that lead to re-collision.

Some of the important parameters to be noted, which account for producing high order harmonics of different efficiencies and cutoff extensions, are the ionization potential of the target I_p, pulse duration τ, peak intensity I_{max} and the frequency of the driving laser field ω_0. In general, one may observe higher extension in cutoff from the species with the higher ionization potential I_p, shorter pulse duration τ and smaller fundamental frequency ω_0 of the driving laser field. Smaller ω_0 also results in low efficiency for a given wavelength and target. Efficiency of high-order harmonic generation scales up rapidly with increase in the intensity up to a certain value, and levels off beyond that value, the so-called saturation intensity. As at this intensity all the atoms are ionized, the number of electrons which generate high harmonics cannot increase further

8.4. Dependence On Ellipticity

It has been demonstrated that high harmonics generation is extremely sensitive to the ellipticity of the fundamental pulses[16,56]. Strong suppression in high harmonics generation has been observed when the fundamental pulse becomes slightly elliptical. The reason for strong sensitivity on the polarization of the driving field has been plausibly explained with the three steps model.

We define ellipticity ε as the ratio between the x component E_x and the y component E_y of the elliptically polarized electric field. The field is defined as purely linear when one of the
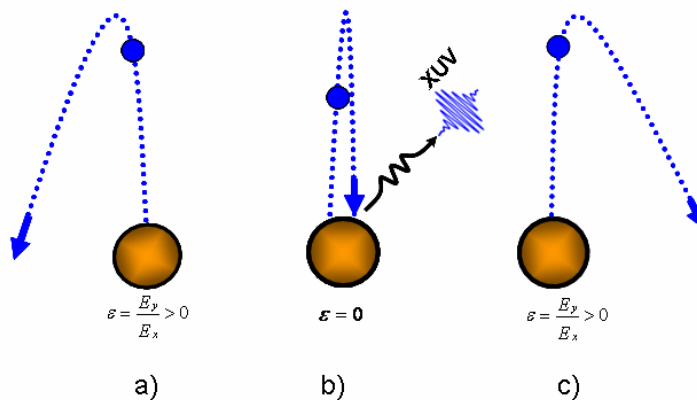
Fig 8.12 The three step process in a) elliptically; b) linearly; c) elliptically polarized laser pulse. When $\varepsilon > 0$, the electron misses the parent ion, and no harmonic emission occurs. At $\varepsilon = 0$, the pulse is linearly polarized and the electron re-collides with the parent ion, thereby emitting high order harmonics.

components is zero, i.e. $\varepsilon = 0$. A slight ellipticity, i.e. a small value of ε, can reduce the probability of the re-collision with the parent ion, as the transverse component drives the free electron packet away from it. Since free electron wave packet has to return and recombine with the core to generate high harmonics, efficiency of high harmonics will be greatly reduced even with the small value of the ellipticity (Fig.8.11). The influence of ellipticity on high order harmonics has been extensively studied [11, 57, 16]. Each of these independent studies shows that a small fraction of the circularly polarized electric field is sufficient to eliminate the harmonic generation process, by preventing electron from returning to the parent ion. This is the key point which allows selection of the single attosecond pulse out of a train of attosecond pulses contained in HHG by the method of polarization gating discussed in the next section.
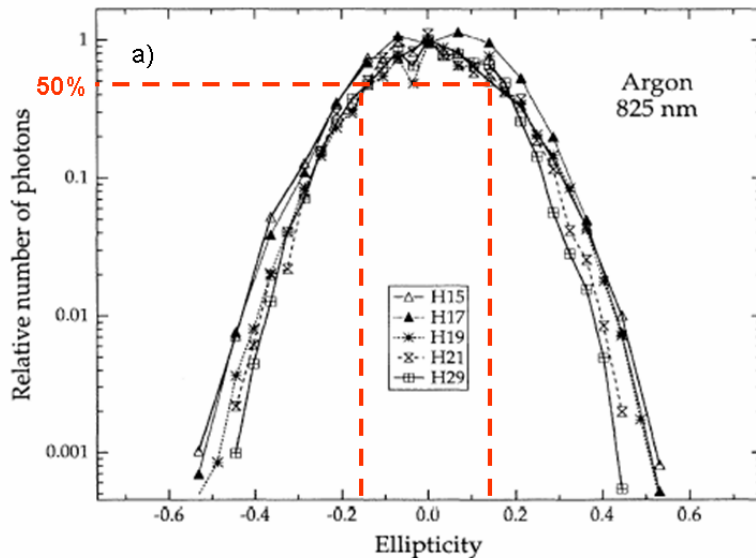
Fig 8.13 High and slow sensitivity of high-order harmonic generation to polarization and the harmonic order. 10% ellipticity reduces the efficiency of harmonics by a factor of 2. Courtesy: K.S.Budil *et al.*, PRA 48, R3437(1993).

8.4. Cutoff and Isolated Attosecond Pulse

A key idea for selecting a single attosecond pulse is to prevent a train of attosecond pulses in the harmonics generation process, and confine the high harmonic emission process to a time shorter than half the optical cycle of the fundamental pulse, i.e. 1.3 fs. One simple method to do this is to use a pulse as short as 5 fs to generate harmonics. Since within such a pulse, the electric field amplitude varies quickly with time, the ponderomotive energy U_p also changes with time.

The highest order harmonic emission, which results from the maximum ponderomotive energy U_{pmax}, can take place only at a well-defined time. By careful filtering of the harmonics generated other than the cut off by a few cycle laser pulse can therefore lead to single attosecond pulse [45]. In other words, if harmonic emission takes place near the peak intensity of the few cycle pulse, harmonics are emitted only during the half optical cycle producing a single attosecond pulse. Since, the cut-off position (defined by $q_{cutoff}=I_p+3.2U_p$) depends on the laser intensity and the absolute phase (described in the next section) of the fundamental pulse, a change in either one of these parameters would obviously give rise to a change in the different cut-off position. Although the technique is very simple, the drawback in this method is that it requires intense extremely short pulses and can use only cutoff harmonics at the expense of many laser shots.

8.5. Polarization Gating

Extreme sensitivity of high harmonics with the ellipticity (Fig.8.11) of the fundamental pulse is the key point in this method of extracting single attosecond pulse. This method generates
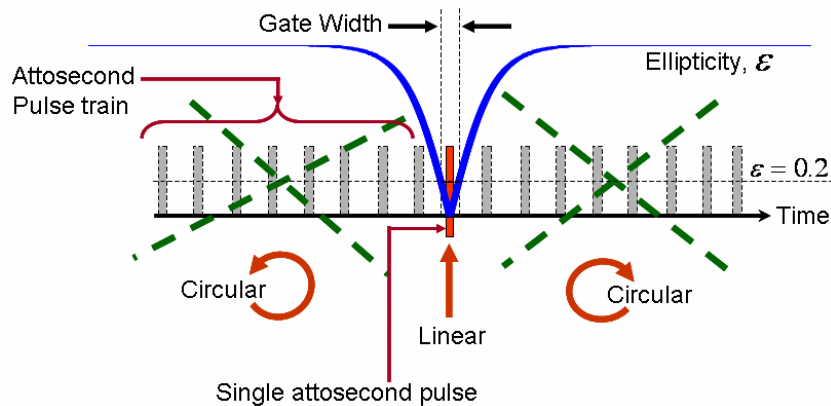
Fig 8.14 Temporal confinement of a single attosecond pulse within a time scale of less than one optical cycle. As the leading and trailing edges of the time dependent ellipticity pulse are circular, they kill the whole pulse train. The middle portion of the pulse has ellipticity ε less than 0.2, which allows emission of an attosecond pulse. Since the width of this region is shorter than one optical cycle, this leads to emission of an isolated single attosecond pulse.

time dependent ellipticity, which has on its leading and trailing edges circularly polarized light, while at the center it consists of a narrow quasi-linear portion, the so-called polarization gate. Typically, the temporal width of the gate is less than one optical cycle. The whole point of

68

producing such a pulse is to kill the whole train of attosecond pulses by leading and trailing edges except at the central region where the ellipticity is not large enough to prevent the harmonic generation process [12, 46]. There are several different ways proposed to generate a time-dependent ellipticity pulse. The simplest way is to split a linearly polarized pulse into two orthogonal pulses with a certain amount of delay, and then recombine them. Though this might be possible with the Mach-zehnder interferometer, with one arm carrying the right circularly polarized pulse and the other arm carrying the left circularly polarized pulse, it is very difficult and takes much work to overlap both the pulses. Worse still, half of the pulse is lost, thereby resulting in a 50% reduction in the intensity. Our method consists of a linearly polarized pulse which is incident on a birefringent plate of a certain thickness at an angle 45^0 to its optics axis. This produces two orthogonal linearly polarized pulses with a certain amount of delay defined by the thickness of the birefringent plate. The two orthogonal pulses are known as the extraordinary pulse (e-ray) and the ordinary pulse (o-ray). An o-ray has spherical o-wavelets [17] and an e-ray has ellipsoidal e-wavelets. The material of the birefringent and the orientation of the E-field of the e-ray and o-ray with respect to the optics axis determine the speed of the wavelet enhancement. For the material quartz, the speed of the o-wavelet expansion v_0 is greater than that of the e-wavelet, v_e. Consequently, the refractive index $n_0 = c/v_0 < n_e = c/v_e$. Hence, the o-ray leads the e-ray when a quartz plate is used to split the pulse (Fig.8.14). These two orthogonal pulses are then superposed with a quarter wave plate with its axis 45^0 to both the orthogonal pulses. This will lead to a time-dependent ellipticity pulse because it has leading and trailing edges circularly polarized and the central region quasilinearly polarized.
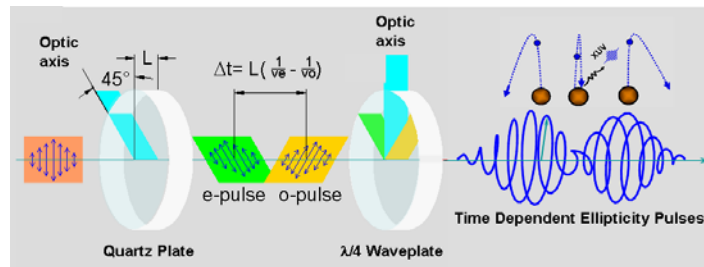
Fig 8.15 Polarization gating of XUV pulses generating time dependent ellipticity pulse.

Since only the narrow central portion has ellipticity less than the value allowed for harmonics generation, which corresponds to a temporal width well below one optical cycle, only one or two

electrons can return to the parent ion, leading to the re-collision of single or double electrton-ion re-collision. The emission due to one electron-ion re-collision results in a single attosecond pulse, while the emission due to two electron-ion re-collision gives rise to two attosecond pulses. In this section, we will first derive a simplified expression and look into the factors which affect the gate width.

We assume that the superposing Gaussian pulses have identical peak field amplitude E_0, carrier frequency ω, pulse duration τ, and carrier-envelope phase ϕ. If the time delay between the two pulses is an integral number, n, of optical periods represented by T_d, the electric fields of the left and right circularly polarized pulses E_L and E_R can be expressed as

$$E_L = E_o \, e^{-2\ln 2\left(\frac{t - T_d/2}{\tau}\right)^2} \left[\hat{x}\cos(\omega t + \phi) + \hat{y}\sin(\omega t + \phi)\right] \times (-1)^n \qquad (8.22a)$$

$$E_R = E_o \, e^{-2\ln 2\left(\frac{t + T_d/2}{\tau}\right)^2} \left[\hat{x}\cos(\omega t + \phi) - \hat{y}\sin(\omega t + \phi)\right] \times (-1)^n \qquad (8.22b)$$

where $\hat{x}$ and $\hat{y}$ are the unit vectors along the x and y directions respectively. The electric field of the combined pulse can therefore be written as

$$E(t) = E_O \{\hat{x}[e^{-2\ln 2\left(\frac{t - T_d/2}{\tau}\right)^2} + e^{-2\ln 2\left(\frac{t + T_d/2}{\tau}\right)^2}] \times \cos(\omega t + \phi)$$

$$+ \hat{y}[e^{-2\ln 2\left(\frac{t - T_d/2}{\tau}\right)^2} - e^{-2\ln 2\left(\frac{t + T_d/2}{\tau}\right)^2}] \times \sin(\omega t + \phi) \} \, (-1)^n \quad (8.23)$$

and the time dependent ellipticity $\xi(t)$ is defined as

$$\xi(t) = -\frac{\left|e^{-2\ln 2\left(\frac{t-T_d/2}{\tau}\right)^2} - e^{-2\ln 2\left(\frac{t+T_d/2}{\tau}\right)^2}\right|}{e^{-2\ln 2\left(\frac{t-T_d/2}{\tau}\right)^2} + e^{-2\ln 2\left(\frac{t+T_d/2}{\tau}\right)^2}} = \frac{\left|1 - e^{-2\ln 2\left(\frac{t+T_d/2}{\tau}\right)^2} \times e^{2\ln 2\left(\frac{t-T_d/2}{\tau}\right)^2}\right|}{1 + e^{-2\ln 2\left(\frac{t+T_d/2}{\tau}\right)^2} \times e^{2\ln 2\left(\frac{t-T_d/2}{\tau}\right)^2}} \tag{8.24}$$

From the identity, $(a-b)^2 - (a+b)^2 = -4ab$, equation (8.25) boils down to

$$\xi(t) = \frac{\left|1 - e^{-\frac{2\ln 2}{\tau^2} * 4 * t * \frac{T_d}{2}}\right|}{1 + e^{-\frac{2\ln 2}{\tau^2} * 4 * t * \frac{T_d}{2}}} = \frac{\left|1 - e^{-\frac{4\ln 2}{\tau^2} * T_d * t}\right|}{1 + e^{-\frac{4\ln 2}{\tau^2} * T_d * t}} \tag{8.25}$$

For $T_d = \tau$, equation (8.25) reduces to

$$\xi(t) = \frac{\left|1 - e^{-\frac{4\ln 2}{\tau} * t}\right|}{1 + e^{-\frac{4\ln 2}{\tau} * t}} \tag{8.26}$$

A plot of $\xi(t)$ against t of equation (8.26) shows $\xi(t)$ varies linearly with t within values close to $t = 0$. As $t \to 0$, ellipticity $\xi(t) \to 0$, which means the portion near $t = 0$ is almost linear. Therefore, for $\xi(t)$ to be very small, i.e. the portion within the temporal range to be a linearly polarized field, the required condition is $(4\ln 2/\tau^2) * T_d * t \ll 1$. Hence from the identity, $e^{-x} = 1 - x$ for $x \ll 1$, expression (8.25) can be approximated as

$$\xi(t) = \frac{\left|1 - 1 + \frac{4\ln 2}{\tau^2} * T_d * t\right|}{1 + 1 - \frac{4\ln 2}{\tau^2} * T_d * t} = \frac{\left|\frac{4\ln 2}{\tau^2} * T_d * t\right|}{2}$$

$$\left(\because \frac{4\ln 2}{\tau^2} * T_d * t \ll 1\right)$$

$$\xi(t) = \left|2\ln(2) * \frac{T_d}{\tau^2} * t\right| \tag{8.27}$$

Hence, ellipticity of the polarization gated pulse approximately varies linearly with time when

$\frac{4\ln 2}{\tau^2} * T_d * t << 1$. Fig. 8.16 shows the plot of real and approximated values of ellipticity $\xi(t)$ with time. Ellipticity is linear near t=0 and better fits the real value into the approximated value within
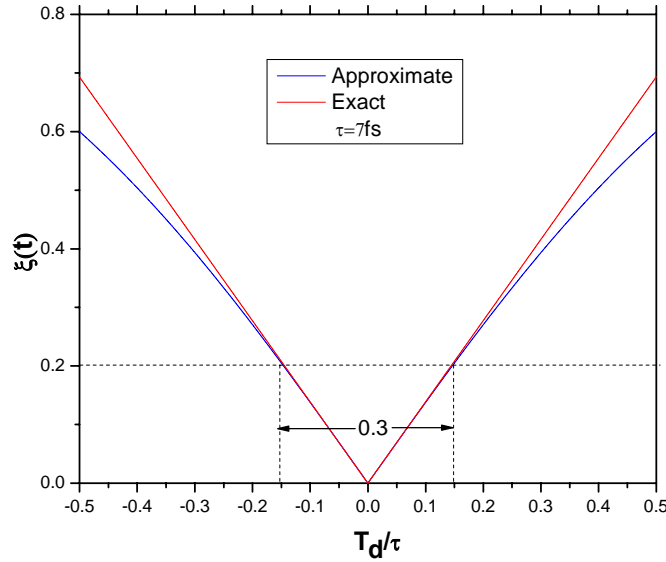
Fig 8.16 A plot of time dependent ellipticity vs T_d/τ for τ fs.
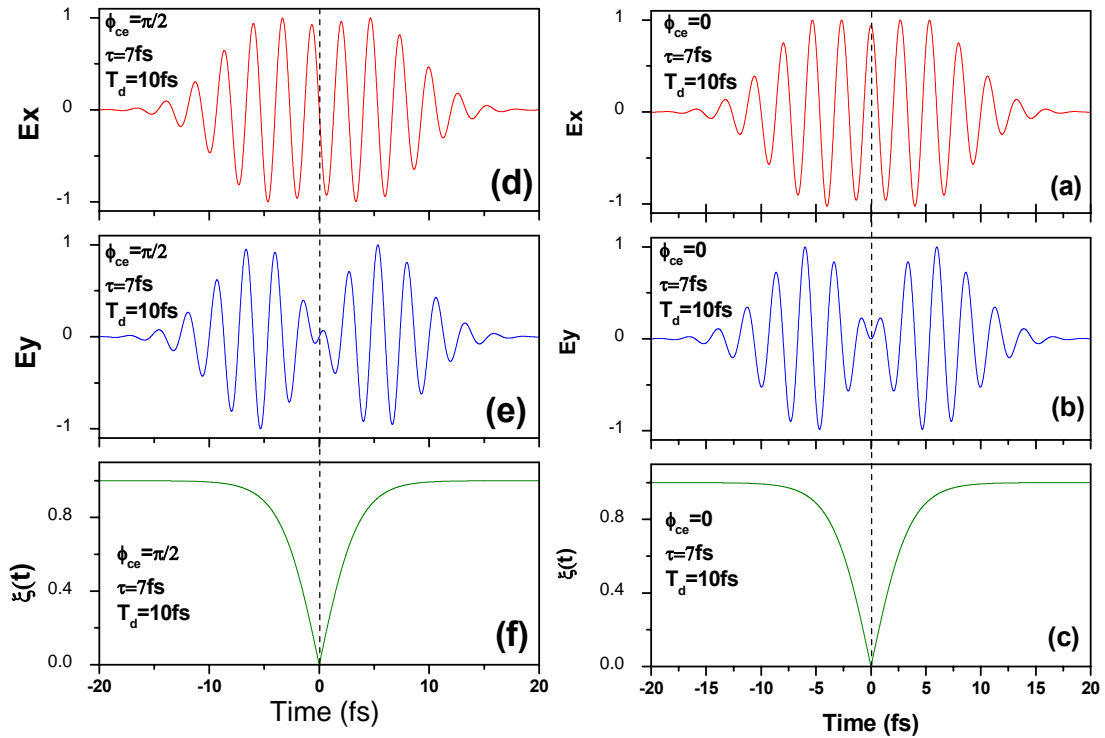
Fig 8.17 Polarization gated x and y components of electric field when CE phase is (a) 0, (b) 0 (d) $\pi/2$,(e) $\pi/2$ respectively. (c) and (f) are the ellipticity at CE phase 0 and $\pi/2$ respectively.

72

the range $\dfrac{T_d}{\tau} = 0.3$. The value corresponds to the ellipticity $\xi(t)$ equal to 0.2 for the pulse

duration $\tau = 7\,\text{fs}$, which our argon fiber can routinely provide. It has been experimentally observed that the yield of harmonic order higher than the 21$^{\text{st}}$ harmonics decreases by an order of magnitude when ellipticity changes from 0 to 0.2 [11]. We define the polarization gate as the narrow temporal region in the Fig.8.16 within which elliticity is negligibly small or less than 0.2. Figs. 8.17 (a), 8.17 (b) are the x component and the y component of the electric field of the polarization gated pulse generated from the laser field of duration 7 fs and carrier envelope phase $\varphi_{\text{CE}} = 0$. Thickness of the birefringent quartz plate was 0.33 mm, which leads to the delay of 10fs between the counter-rotating circularly polarized pulses. Fig. 8.17(c) is the plot of time dependent ellipticity with time. Figs. 8.17 (d) and (e) are the plots of x and y components of the electric field when the carrier envelope phase of the driving laser is $\varphi_{\text{CE}} = \pi/2$. Fig. 8.17 (f) is the resulting ellipticity. In both cases, the x-component of the electric field has higher amplitude than the y-component. The amplitude of the electric field of the y-component is zero at t=0. So, at t=0, the pulse is linearly polarized, and harmonic generation in this region is more efficient. On either sides of this region, ellipticity is not equal to zero. However, within the narrow region near t = 0, the ellipticity is quite smaller than the value required to drive the electron away from the parent ion. This narrow region where the pulses are quasi-linearly polarized can therefore drive the electron back to the parent ion thereby producing the emission of high order harmonics. The temporal width of that region defined as the gate width can be estimated from relation (8.28).We can re-write equation (8.27) as

$$t = \left| \frac{1}{2\ln(2)} * \xi(t) * \frac{\tau^2}{T_d} \right| \tag{8.28}$$

Hence, from Fig.8.16 the temporal width T_G for a particular value of ξ can be written as

$$T_G = 2t = 2 * \left| \frac{1}{2\ln(2)} * \xi * \frac{\tau^2}{T_d} \right| = \left| \frac{1}{\ln(2)} * \xi * \frac{\tau^2}{T_d} \right| \tag{8.29}$$

Hence, for $\xi = 0.2$, relation (8.29) boils down to

$$T_G \approx 0.3 * \frac{\tau^2}{T_d} \tag{8.30}$$

where T_d is the delay between the two circularly polarized pulses. For quartz plate of thickness L, T_d can be written as

$$T_d = L * \left(\frac{1}{V_e} - \frac{1}{V_0} \right) \qquad (8.31)$$

where V_e and V_0 are the group velocities of two orthogonal extra-ordinary and ordinary pulses. Amplitude of the linear portion of the electric field of the polarization gated pulse at t=0 for a given value of pulse duration and delay from relation (8.23) can be written as

$$E(0) = 2 E_0 e[-\ln(2)/2](T_d/\tau)^2 \qquad (8.32)$$

The amplitude of the electric field of the linear portion for a given τ therefore decreases as the delay between the pulses T_d increases. Relation (8.31) shows that the gate width T_G can be reduced either by increasing delay T_d or by reducing the pulse duration of the driving laser. If one tries to reduce T_G by increasing T_d, it will reduce the electric field strength of the linear portion thereby reducing the efficiency of the harmonic emission. Moreover, since the leading circularly polarized pulse does not produce high harmonics, but depletes the ground state population of the atom; harmonic generation will be greatly suppressed in this case. It therefore turns out that a good alternative to this is to use the driving pulse as short as possible, as T_G is proportional to the square of the pulse duration, However, there is still a limit set by the system (hollow core fiber) for the minimum achievable pulse duration which prevents us from using a
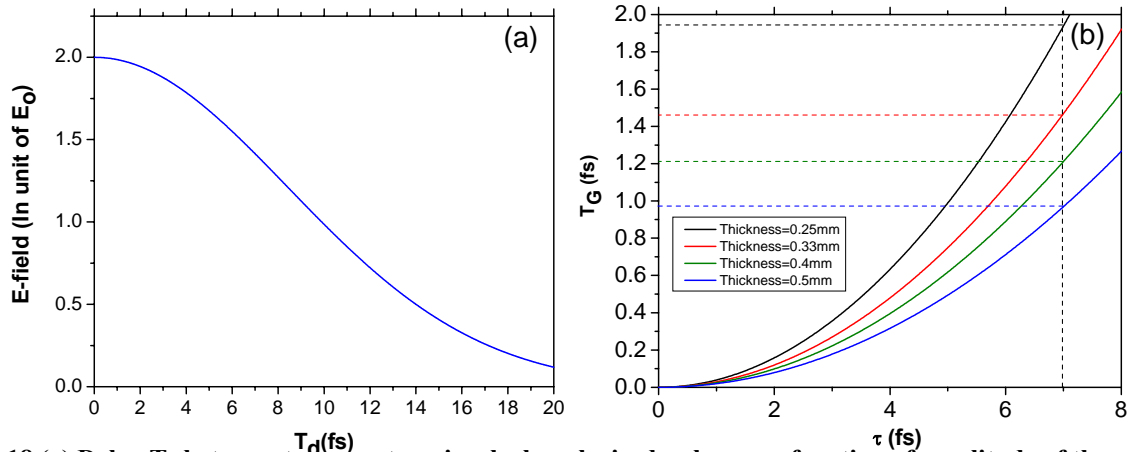
Fig 8.18 (a) Delay T_d between two counter–circularly polarized pulses as a function of amplitude of the electric field when t=0. (b) Gate width T_G as a function of the pulses duration τ for different quartz plate thickness.

pulse duration as short as we want. With the appropriate thickness of the quartz plate (0.5mm) and routinely available pulse duration (7fs), the gate width has been successfully reduced to a temporal width less than half the optical cycle. Harmonic generation from this configuration has successfully been used for single shot measurement of the carrier envelope phase, which I will be discussing in the next few chapters.
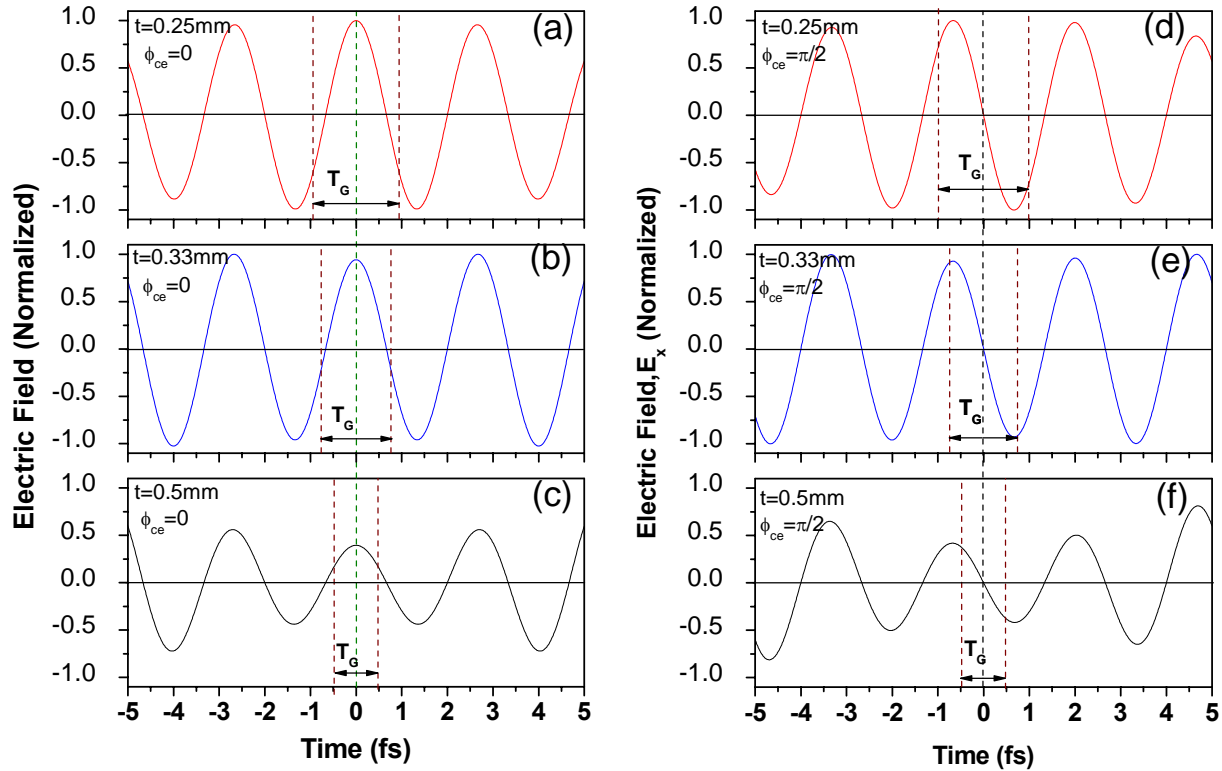
Fig 8.19 x-component of polarization gated electric field amplitude when quartz thickness is (a) 0.25mm (b) 0.33 mm (c) 0.5 mm at CE phase $\phi_{ce} = 0$ and (d) 0.25mm, (e) 0.33 mm, (f) 0.5 mm at CE phase $\phi_{ce} = \pi/2$.

As can be seen from the plot of Fig. 8.18 (a), the electric field of a linearly polarized pulse at the center of the polarization gated pulse, where t = 0, decreases with the delay between the two counter-circularly polarized pulses. Fig.8.18 (b) is the plot of polarization gate width as a function of the pulse duration for quartz thicknesses 0.25 mm, 0.33 mm, 0.4 mm, and 0.5 mm. Those are the thicknesses available in our laboratory. From the plot it is clear that all the above-mentioned thicknesses can generate a polarization gate width less than one optical cycle (2.6 fs) with a laser of pulse duration ~7 fs, which our hollow core fiber can deliver most of the time. If.
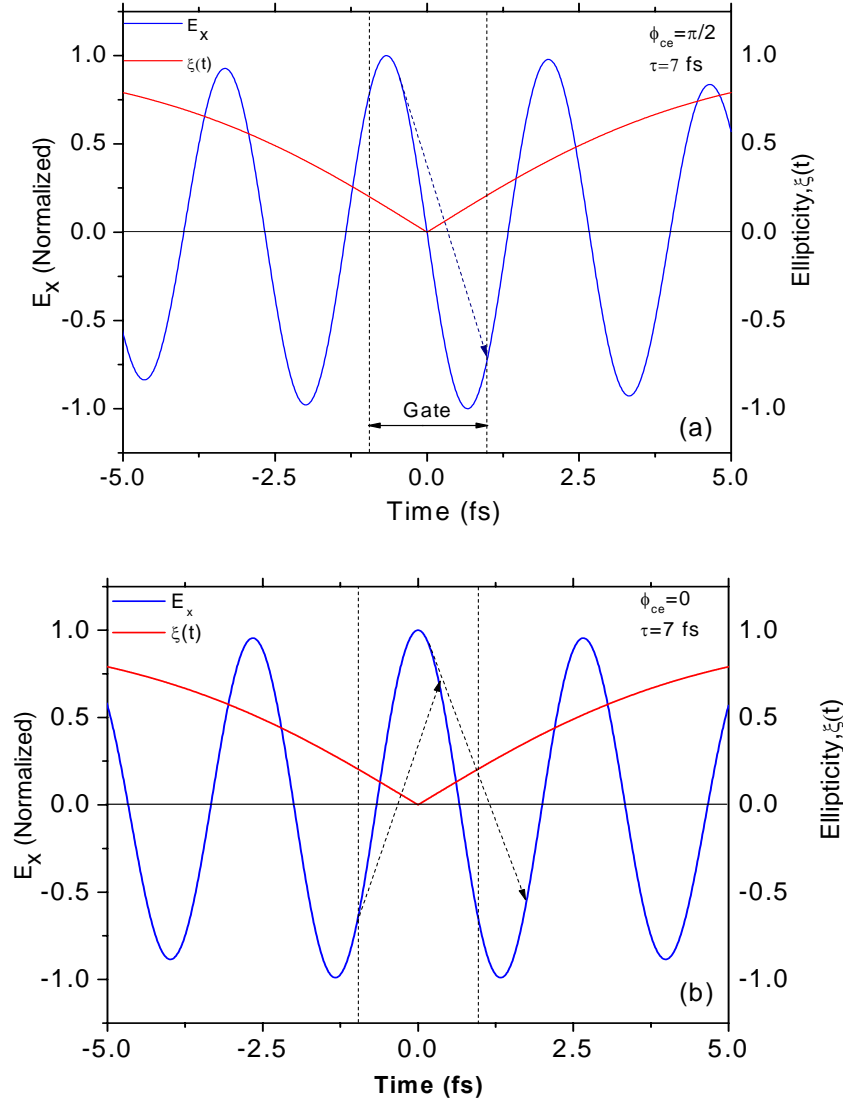
Fig 8.20 The effect of the carrier-envelope phase of the driving laser pulse on the returning of the ionizing electron within the polarization gate. The carrier envelope phase is 90 degree in (a) and is 0 degree in (b). The solid line is the electric field of one component of the laser pulse. The dashed line is the ellipticity. The range within the two vertical dotted lines is the polarization gate width.

the pulse duration is around 8 fs, the quartz of 0.25 fs is no longer useful to generate a polarization gate width less than one optical cycle. In order to have the gate width T_G less than half the optical cycle from the polarization gating of laser with pulse duration ~7 fs, the thickness of the quartz should be increased. The 0.25 mm and 0.33 mm quartz plates cannot produce T_G less than half the optical cycle (~1.3 fs). Only the thicknesses of 0.4 mm and 0.5 mm can generate temporal width T_G less than half an optical cycle. A gate width T_G less than one optical cycle (2.6 fs) is necessary in order to see the effect of the carrier envelope phase on the high

harmonic spectrum, while a gate width T_G less than half the optical cycle (1.3 fs) is essential to extract a single attosecond pulse Fig.8.20 shows the plot of the x-component of the electric field produced by polarization gating with quartz plates of different thicknesses. As the thickness of the quartz plate is increased, the polarization gate width T_G and the electric field amplitude E_x within the gate also decrease. Hence, the price to pay in order to reduce the gate width to less than half the optical cycle is to lose intensity of the linear electric field in the polarization gating. Fig.8.20 (a) and (b) is the plot of the x-component of the electric field and the ellipticity of the polarization gated pulse. This is the component of the electric field which contributes to the
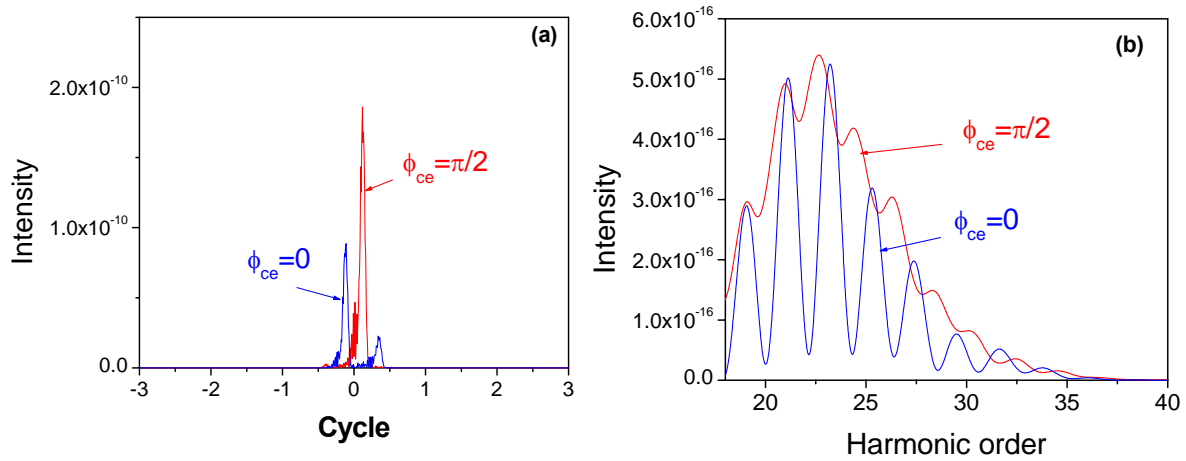
Fig 8.21 (a) Theoretical calculation of intensities of attosecond pulses when CE phase $\phi_{ce} = 0$ and $\phi_{ce} = \pi/2$ and (b) corresponding harmonic spectra in the spectral domain. From [Z.Chang PRA] .

a harmonic generation process. The other component, i.e. the y-component, has small amplitude and is zero at t = 0. The pulse duration and the delay between the two circular pulses are 7 fs and 7.5 fs generated by using a quartz plate of thickness 0.25 mm. We define the carrier envelope phase (CE phase) as the offset of the peak of the electric field from the time t=0 where ellipticity $\xi(0)$ =0. The central narrow region near t = 0, where ellipticity $\xi(t)$ is negligibly small, is known as gate width. At CE phase $\phi_{ce} = \pi/2$, only electrons released between t=-0.125 fs to t=0 can return within the gate as indicated by the arrow leading to the emission of one attosecond pulse. In the spectral domain this corresponds to the super-continuum. On the contrary, at CE phase $\phi_{ce} = 0$, as shown in Fig.8.20 (b), two groups of electrons with short trajectories are released
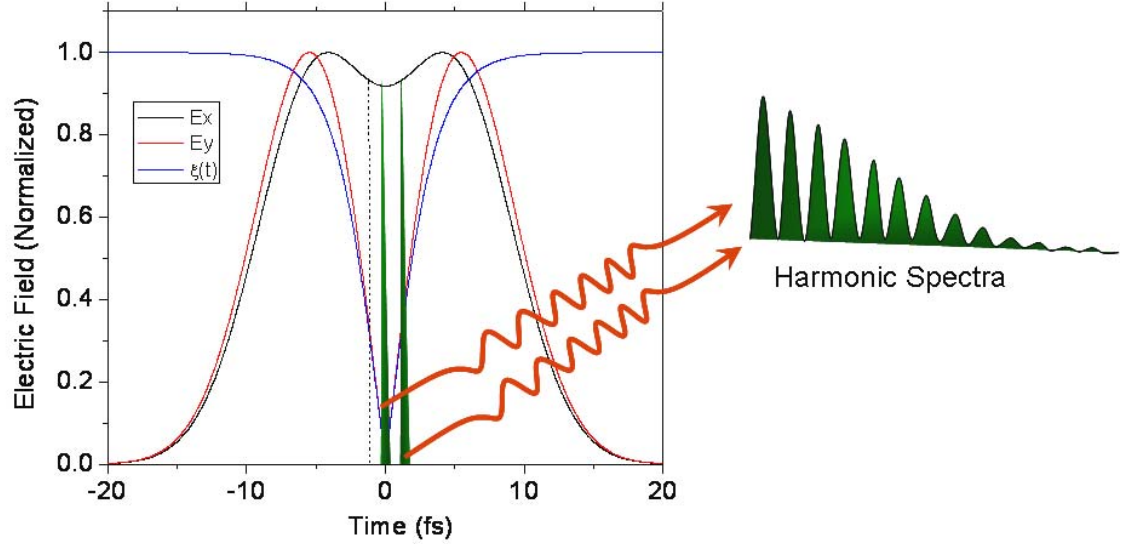
Fig 8.22 X (black) and y (blue) component of the polarization gated pulses. The blue curve is the time dependent ellipticity, $\xi(t)$. The pulse duration is 7 fs and the pulse was synthesized by using a quartz plate of the thickness 0.33 mm at CE phase $\phi_{CE} = 0$. Two thin green lines within the gate represent two attosecond pulses with two different intensities. Two pulses changes their position within the gate as the CE phase is changed, resulting the decrease in the modulation depth and shift in the harmonics spectra. The green curve on the right represents the interference of the attosecond pulses in the spectral domain, so called harmonics.

within the gate. One returns within the gate, and the other returns outside the gate but the ellipticity is still small. In this case, two attosecond pulses are produced and the second one is weaker as shown in Fig. 8.21 (a) shows the theoretical plot of attosecond pulses at two different carrier envelope phases. At CE phase $\phi_{ce} = 0$, there is emission of two attosecond pulses (blue curve in (a)) leading to the discrete harmonics (blue spectra in (b)) in the spectral domain. At CE phase $\phi_{ce} = \pi/2$, only one ttosecond pulse (red curve in (a)) was emitted leading to the super continuum spectra (red spectrum in (b)) in the spectral domain. Fig.8.21 is a plot of the x (black) and y (red) components of the polarization gated electric field and the corresponding ellipticity $\xi(t)$ (blue) when CE phase was zero. The pulse duration τ was assumed to be 7 fs, and a 0.33 mm thick quartz plate was used. The corresponding delay T_G is 10 fs. Two thin blue lines within the gate represent the burst of two attosecond pulses with two different intensities, one weak and the other strong. The interference between these two pulses yields modulated harmonic spectra (green spectra on the right). As the CE phase changes from 0 to 90 degrees, the pulse within the gate also moves, resulting in the decrease in amplitude of the one of the pulses. Thus the spectral

modulation depth also decreases till the spectrum evolves into the super continuum. Fig.8.23 is the harmonics spectra plotted at different carrier envelope phases. As the CE phase is changed, the modulation depth of the harmonics also decreases and eventually evolves into the super-continuum when the CE phase becomes 90 degrees. So, if the XUV spectrum can be measured and analyzed for every laser shot, then it is possible to determine the shot-to-shot variation of the CE phase effect in many experiments when the CE phase of the few-cycle laser pulses are not locked. Previously, CE phase has been measured by f-to-2f interferometers and phase meters based on above-threshold ionization [47]. Although f-to-2f interferometers havebeen used to
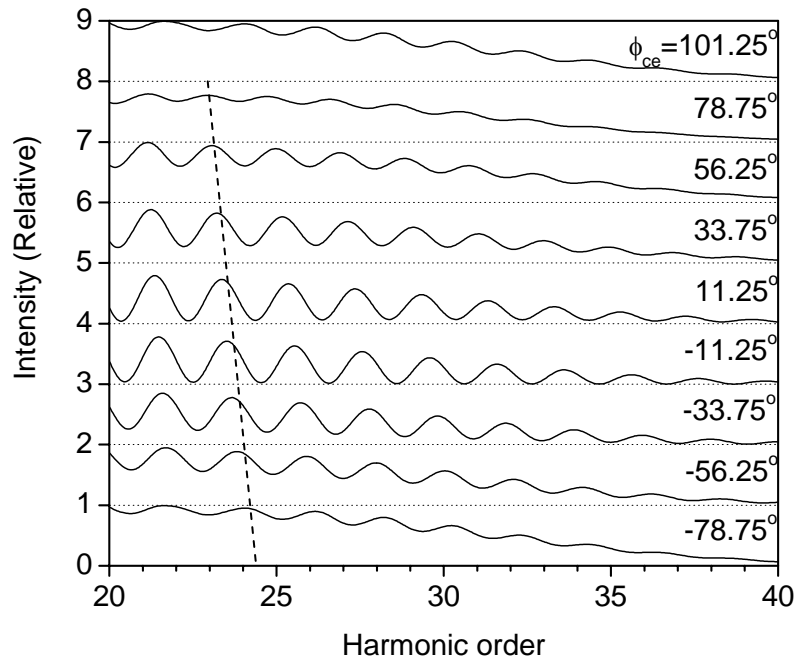
Fig 8.23 Numerically simulated high order harmonic spectra for different carrier envelope phases. Modulation depth of the spectra decreases as the CE phase is increased from 0 degree to 90 degrees. The XUV spectra also shifts as the CE phase is changed. Dotted lines in the plot are a guide to the eye.

stabilize and evaluate the CE phase stability of laser system, the measured results are in-loop measurement and are subject to the power fluctuation of the laser pulses. It was found that the 1% of the power change can cause 160 mrad of measurement error. Since the RMS fluctuation and long term drift of most laser systems are larger than 1%, the magnitude of the error can be significant. Furthermore, it is almost impossible to measure the absolute value of the. CE phase with this approach because of difficulties in accounting for the effects of dispersion and linear effects in the f-to-2f setup. Stereo-ATI is a powerful method to measure the CE phase, however,

it requires 30-100 laser shot accumulation. Measuring the single shot phase is difficult due to space charge effects. The major challenge however for the measuring single shot absolute CE phase with the XUV spectrum is to obtain enough XUV photon counts per laser shot. Every effort has been made to increase the number of photon counts, which I will be describing in the next chapter.

CHAPTER 9 - Design of XUV Spectrometer and Single Shot Measurement

In order to record the shot-to-shot effect of CE phase on the XUV spectrum, the experimental set up should be designed in such a way that it can generate sufficient extreme ultraviolet (XUV) photons. As the number of photons that can be produced is limited, the next step for better measurement of the single shot CE phase should be finding a way to prevent photons from being lost during the experiment. We know that the highest harmonics follow the cutoff rule, which is the ionization potential of the gas and kinetic energy of the electron in the field $(q_{cutoff} = I_p + 3.2I\lambda^2)$. It therefore seems at first sight that the harmonics energy can be increased just by increasing the laser intensity. However, it is not going to work that way because it is known well that the highest laser energy that makes sense to use is the saturation intensity. Saturation intensity of the laser is the intensity which ionizes and use up all the neutral atoms. By
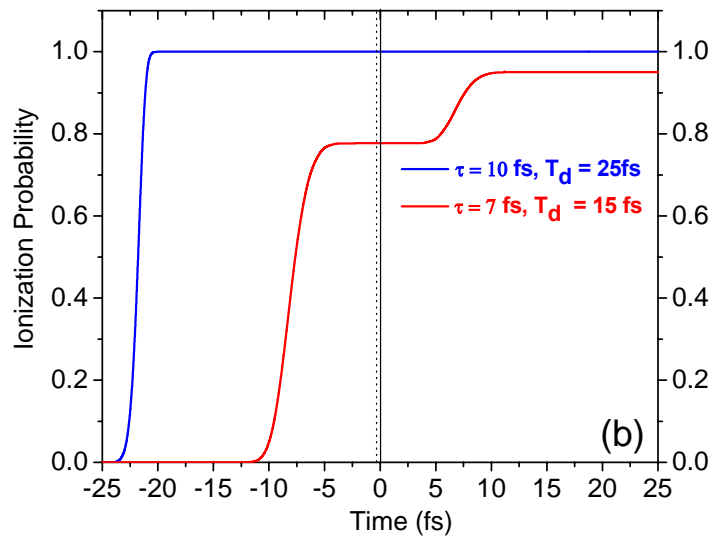
Fig 9.1 The ionization probability of argon atom in laser fields with time dependent elasticity . Blue line:both circular pulses are 10fs and the delay between them is 25 fs. Red line: both circular pulses are 7fs and the delay between them is 15 fs.

ionizing all the neutral atoms also does not lead to efficient harmonics. One reason for this is the plasma induced defocusing, because the plasma has negative refractive index and acts like a negative lens. As one tries to focus the laser, it would defocus immediately. The other reason is that phase matching is very difficult at higher intensity, which I will be discussing later.

Fig.9.1 shows the ionization probability of an argon atom calculated by ADK theory [65]. Laser intensities are the same for both pulses at t = 0 fs where laser is linearly polarized. Harmonics generation takes place only within the interval shown in Fig 9.1 by two dashed lines. The ionization probability at t = 0 is 83% for 7 fs pulses which is less than with 10 fs pulses (100%). For this reason, intensity of the harmonics generated by 7fs pulses will be higher than that produced by 10 fs pulses. The ionization probabilies with 7fs and 10 fs were compared here because routinely available pulse with argon hollow fiber is 7fs in our lab. The result of gating with this pulses delayed by 15 fs will be presented in the next few pages. Here, I will present our effort to build an XUV spectrometer to generate high harmonics as efficiently as possible by optimizing all these critical parameters.

In order to generate harmonics, the argon atom was taken as the microscopic nonlinear medium in this entire work. The reason for making this choice was the requirement of lower energy for generating harmonics, which polarization gating with a thicker quartz plate can deliver. The experimental arrangement is shown in Fig. 9.2. Briefly, to avoid dispersion and chromatic aberration, an off-axis parabolic mirror of focal length 250 mm was used to focus the laser pulses to the target. A gas cell inside the chamber is a thin-wall tube which has two pinholes drilled in it by the laser itself, allowing the beam to pass through the gas inside, but confining the gas to a length about that of the tube's internal diameter 1.44 mm. The diameter of the hole is comparable to the focal spot size, ~ 60 μm diameter. The gas inside the tube can be varied from 0 Torr to 200 Torr with less than 200 mT in the background vacuum chamber when at the highest target pressure. At about 10 inches from the focus, an aluminum filter of 100 nm thick is mounted on the stainless steel gate valve (Mini UHV Gate Valve Series 010) to prevent it from damage by laser heating. At this distance the laser beam has diverged to a low intensity, and damage to the filter is very unlikely. Since, the laser spot size at this distance is ~4.4 mm, which is quite smaller than the diameter (10 mm) of the filter, beam clipping therefore never occurs for a well-centered beam. The Al filter therefore never reduces the throughput of the spectrometer by blocking photons from reaching the grating surface. On the contrary, aluminum filter blocks the laser and

low order harmonics (only high order can be used for polarization gating), and serves as a shield to prevent gas flow from the interaction chamber to the detector chamber. This is essential in order to maintain pressure as low as 10^{-8} Torr, thereby preventing electrical breakdown of the MCP detector and reducing absorption of photons by the gas. A silver mirror placed slightly
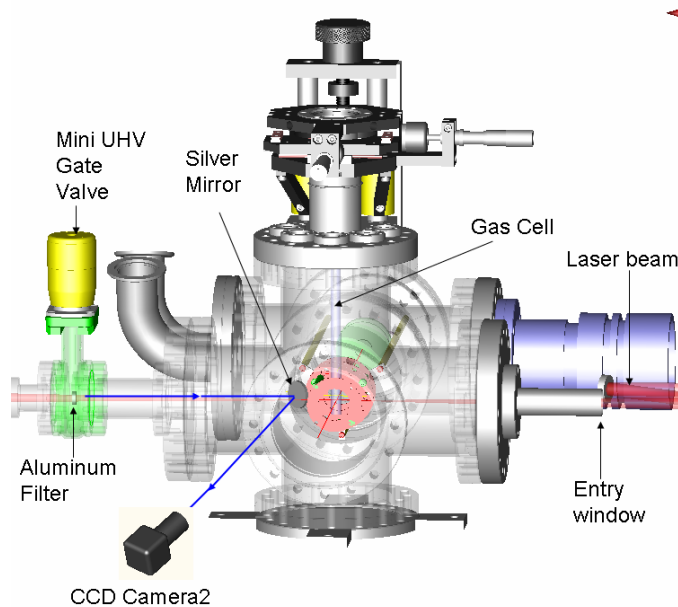
Fig 9.2 Laser-Gas interaction chamber. A laser spot on the surface of the aluminum filter mounted on the Mini UHV Gate Valve can be viewed through the silver mirror with a CCD camera coupled to the monitor.

off the beam path and at a 45^0 angle to the laser direction provides a complte view of the surface of an aluminum filter mounted on the gate valve inside the chamber (Fig.9.2). This aluminum filter also serves as a reference iris to align the beam. The beam spot on the surface of the aluminum filter can be monitored with the help of a CCD camera. An aluminum rod with a 0.5 mm aperture is the second reference iris to align the beam (Fig 9.3). Two sets of right angle clamps have been used to fix this aperture rod at the correct position. The first clamp is attached to a stainless steel post to set the fixed height from the table surface. The second clamp holds the aperture rod aligned with the laser beam propagating at 5 inch height from the experimental table. The laser beam which passes through the hole and hits the center of the Al filter ensures perfect alignment because this is the only path that the beam can travel and be incident on the grating surface at the prescribed glancing angle (3.73^0) without clipping (Fig. 9.5). During the
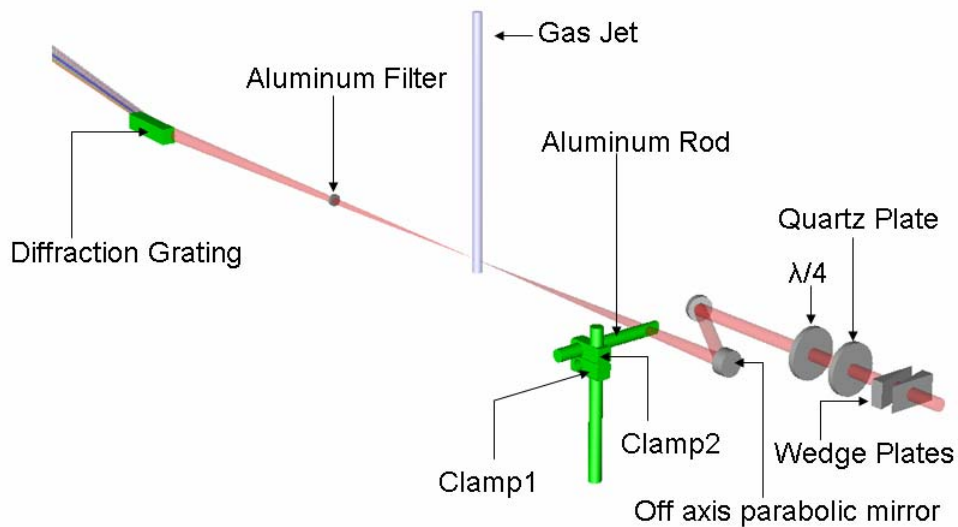
Fig 9.3 Aluminum rod with 0.5 mm aperture and the aluminum filter serving as two reference points for aligning the beam. Clamp1 rigidly fixed to the vertical rod keeps aluminum rod at a fixed height from the table while Clamp2 rigidly fixed to the horizontal aluminum rod and pass through the vertical rod, allows Al rod to rotate away from the beam path during the experiment.

experiment, after the beam is aligned, the aperture rod can be rotated out of the beam path. For the alignment of the pin hole on the gas cell with reference to the aligned beam, laser power is reduced by using neutral density (ND) filter to protect gas cell from damaging by ablation. Pin hole (~60 µm) on the gas cell is moved around the beam diameter near the focus with the help of XYZ manipulator until the aligned beam passes through that hole. Once the beam spot is visible on the Al filter surface through CCD camera2 (Fig.9.2) focused on the silver mirror, gas cell is moved slightly back and forth vertically and horizontally perpendicular to the beam direction. If spot on the Al filter disappeared when the cell is moved in either directions, it is confirmed that beam is passing through the pin hole.

The generated XUV beam is incident at an incident angle 86.262^0 on the high efficiency, flat field XUV toroidal grating (JOBIN YVON HORIBA) placed 23 inches away from the focus, which serves as an image distance. The grating is 7.3 cm long and 1.3 cm wide with 384 grooves/mm, providing a wavelength range from 11nm to 35nm (35 eV-110 eV). The vertical
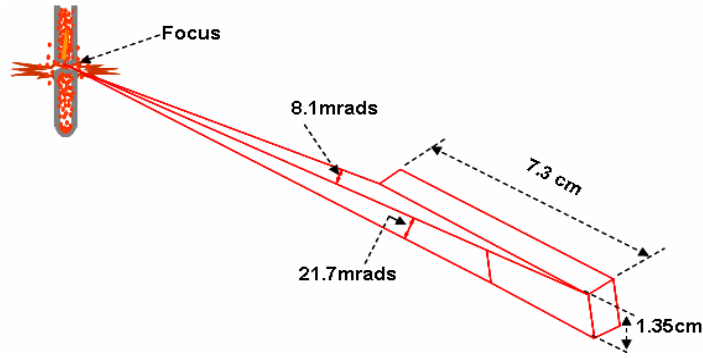
Fig 9.4 Sketch of toroidal diffraction grating at 585.9 mm distance from the focus. The XUV beam is incident at a glancing angle 3.7^0 with the surface. The horizantal and vertical acceptance angles are 8.1mrads and 21.7 mrads respectively, while the divergence angle of XUV is 3.5 mrads.

Grating Reference: 541 00 120		
Toroidal Flat Field Grating: OPTION1		
LA(mm): 585.90	α(deg):	- 86.262
LH (mm): 685.19	βH(deg):	135.512
Length of the spectrum (mm) B1B2 : 83.5		

Grating Size: 18×78×15 mm
Effective Area: 13×73 mm
Collect Area: 13×73*Cos(86.262)

Note : For clarity, the grating is not to the given scale

Scale: 1:9 VM Date: JUNE 11, 2003.
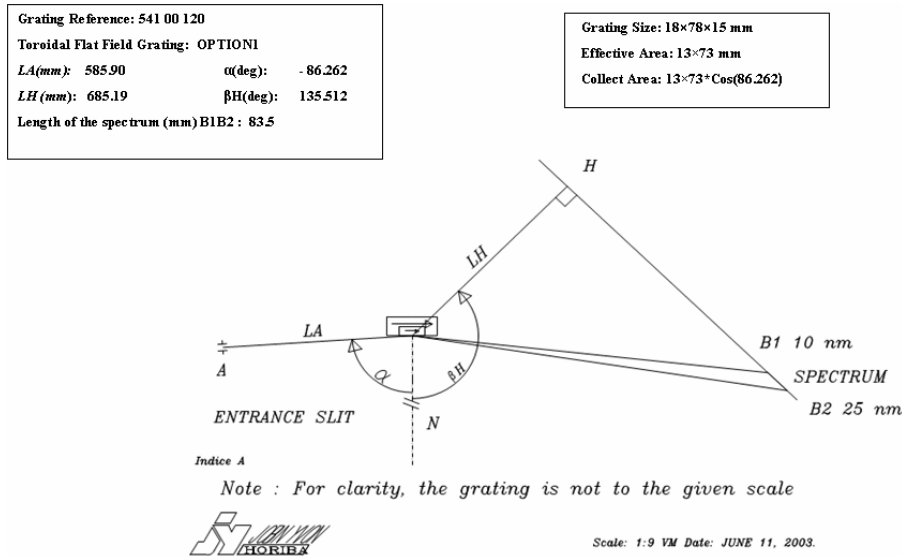
Fig 9.5 Grating optical layout. (Courtesy: Jobin Yvon Horiba)

and horizontal acceptance angles of the grating from the focus are therefore 8.1mrads and 21.7 mrads respectively (Fig.9.4). In order to match this acceptance angle with the divergence angle of the laser, the incident beam size on the focusing mirror was made 6.8 mm diameter, which expands to 10 mm as it reaches the grating surface.

This value was obtained by solving the expression given by equation (9.1) for w_0. Where, w_0 is the focal spot size at a distance z =584.2 mm from the grating surface.

$$\frac{1}{w_0} \times \sqrt{w_0{}^4 + a^2 z^2} - w = 0 \tag{9.1}$$

The value of a in the expression is λ/π and λ =790 nm for the Ti:Sapphire laser. From the

value of w_0, we can therefore estimate the spot size required on the surface of the parabolic.
mirror, which would expand to the size without clipping, while incident on the grating surface.
For adjustment of the beam to the required size on the surface of the off-axis parabolic mirror,
the spherical mirror of focal length 150 cm placed after the exit window of the hollow core fiber
can be moved to the desired distance. The parabolic mirror focuses the beam to the diameter
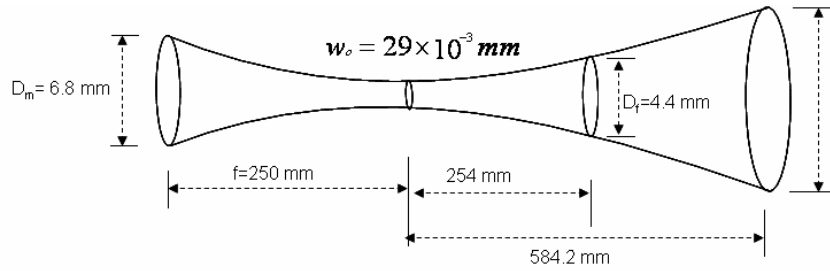
Fig 9.6 Laser beam profile between off-axis parabolic mirror and the diffraction grating surface. A diameter, Dm =6.8 mm on the parabolic mirror surface expands to a diameter D_f =4.4 mm and D_g=10 mm as it reaches the Al filter surface (diameter =10 mm) and grating surface respectively. The Al filter and the diffraction grating are at 254 mm and 585.9 mm away from the focus respectively.

w_0 =59.4 mm at a focal distance 250 mm. XUV photons transmitted from the aluminum filter
can also be reflected at an angle of 45^0 by a retractable bare gold mirror into the second
microchannel plate. This allows us to estimate the divergence angle of the XUV beam. Fig.9.7
shows the far field image and the intensity profile of the harmonic spot image on the second
microchannel plate detector. The grid pattern in the image is from the mesh that supports the thin
aluminum filter. The spot has a half angular width of 3.5 mrad at the $1/e^2$ criterion and was
calculated from the divergence of the harmonic beam assuming a Gaussian intensity distribution.
The divergence angle matches well with the acceptance angle of the diffraction grating which is
8.1 mrad in the horizontal direction and 27.1 mrad in the vertical direction. Since the number of

photons per laser shot is low, it is important to match the angles to reduce the detection loss for suppressing the statistical noise of the measured single shot harmonic spectrum. The divergence angle of the harmonic beam is much smaller than that of the laser beam 8.1 mrad. The ratio is a useful number for designing beam lines that use the harmonic pulses for pump probe experiments.
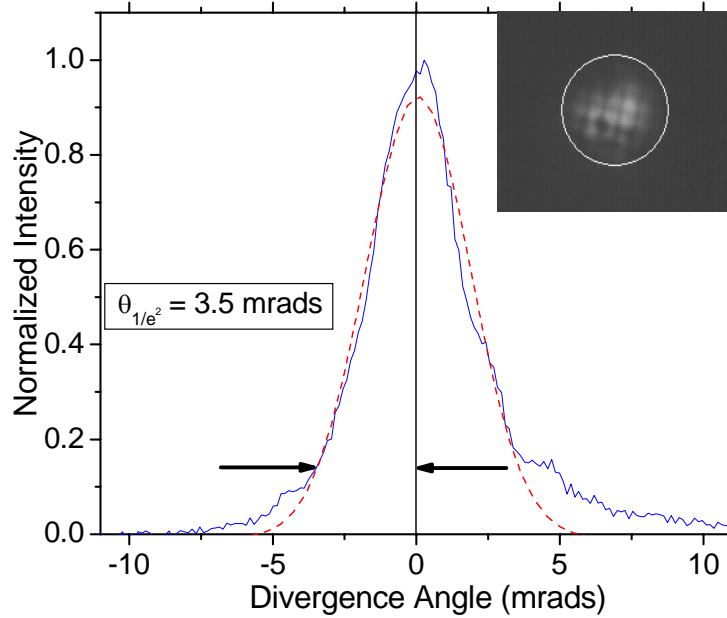
Fig 9.7 Far field image of XUV and its lineout. Divergence angle at $1/e^2$ criterion is 3.5 mrad which matches with the acceptance angle of the grating used.
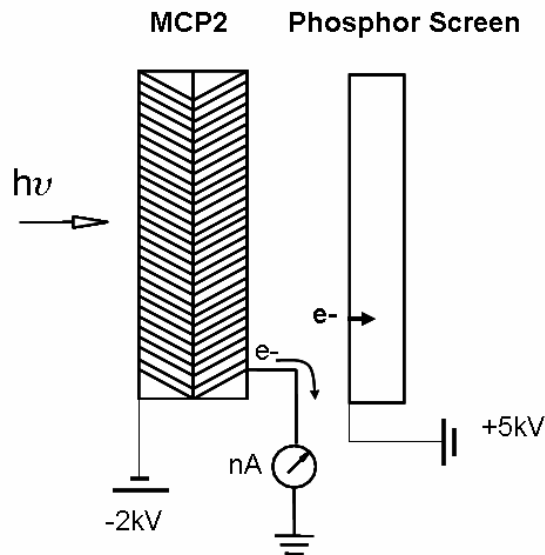
Fig 9.8 Schematic of the second microchannel plate wiring. Nano ammeter connecting the rear of the MCP and the ground provides an estimate of high harmonic photons per laser shot.

The number of harmonic photons per laser shot can also be estimated by using the same microchannel plate. An ammeter which connects the MCP rear and the ground reads the difference between the current with and without the presence of XUV on the MCP as shown in Fig.9.8. If number of photons per laser shot generated is N, it can be written as

$$N = \frac{\Delta I}{Ge f_{rep} R_{Au} Q T_{Al}} \tag{9.2}$$

where ΔI is the difference in current with and without the presence of XUV on the MCP. $G, e, f_{rep}, R_{Au}, Q,$ and T_{Al} are MCP gain, charge of an electron, repetition rate of the laser, reflectivity of the gold mirror, quantum efficiency of MCP and transmissivity of the aluminum filter respectively. When the MCP voltage was 1.8 kV, ΔI was $0.04 \, \mu A$. The values of G, e, f_{rep}, Q, T_{Al} (for 27th harmonics) and R_{Au} are 5.3×10^6, 1.6×10^{19}, 100, 0.1, 0.8 and 0.02 respectively. With those values, equation (9.2) gives 30,000 photons per laser shot at 55 Torr target pressure.

9.1 Detector Calibration

In order to identify what pixel number corresponds to which harmonics order, a 30fs, 1 kHz and 0.8 Watt Ti:Sapphire laser from the Kansas Light Source (KLS) was focused on the neon gas target to generate high order harmonics. Harmonics are spectrally resolved and imaged by the toroidal diffraction grating on the phosphor screen placed parallel to the imaging plane (HB1B2) of the grating (Fig.9.5). The reason for choosing neon gas and the long pulse for the calibration was its cutoff ($\sim$ 63 at 4×10^{14} and 30 fs) which extends way beyond aluminum cutoff ($\sim$43rd) and the harmonics which are sharp and clearly resolved. As the cutoff position remained unchanged while intensity was decreased to a certain value, evidently harmonics cutoff of neon gas extends longer than the Al cutoff edge over that intensity range. It is therefore obvious that the cutoff that has been observed on the phosphor screen is the Al cutoff, which provides a reference to identify other harmonic orders. The spectral range of this spectrometer can be tuned

a little by shifting the detector position; however, to minimize the imaging aberrations, the spectrometer was set ranging from 34eV to 72eV , which permits detecting HHG from 23rd order to 45th order. Harmonic spectra generated by focusing a 30 fs and 0.8 Watt laser the neon target are shown for 20 Torr pressure. As the position of the cutoff harmonics occurs at the pixel number 548 on the phosphor screen, it should correspond to either the 43rd or 45th harmonics order, which is the highest possible transmission set by the aluminum filter (Fig. 9.9).
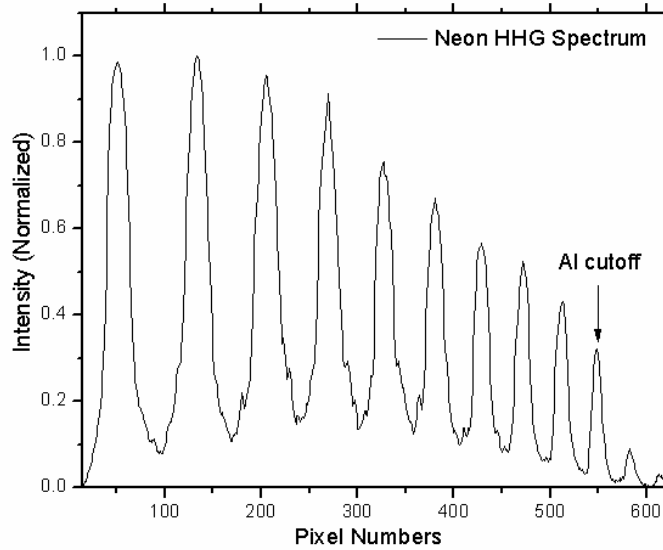
Fig 9.9 Harmonic spectra from neon generated by focusing 30 fs ,1kHz and 0.8W laser. Apparently, a sharp aluminum cutoff lies at the pixel number 548.

In order to identify exact cutoff order, calculation was done by assuming the grating to be flat, for which we can apply the general diffaction equation given by

$$m\lambda = a(Sin\gamma - Sin\alpha) \tag{9.3}$$

where m is an integer and α, γ and λ are the angle of incidence, angle of diffraction and the wavelength of the different harmonics order. The values of a and α for the grating used are 2.6×10-3 mm/lines and 86.2620 respectively. The distance from the center of the grating to H is 27 inches (Fig.9.10).The diffracted angle γ for a different harmonic can therefore be calculated by using the equation given by

$$\gamma = ArcSin\left[\frac{m\Lambda + aSin(-\alpha)}{a}\right] \qquad (9.4)$$

where, $\Lambda = \dfrac{\lambda}{2n+1}$ and n is an integer.
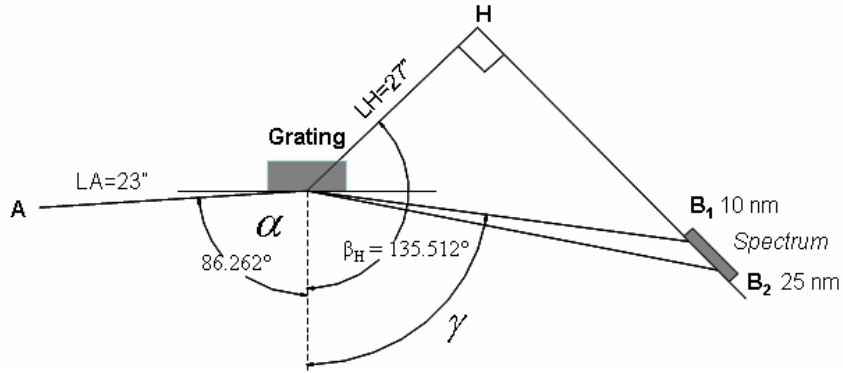
Fig 9.10 Grating optical layout. (Courtesy Yvon Horiba)
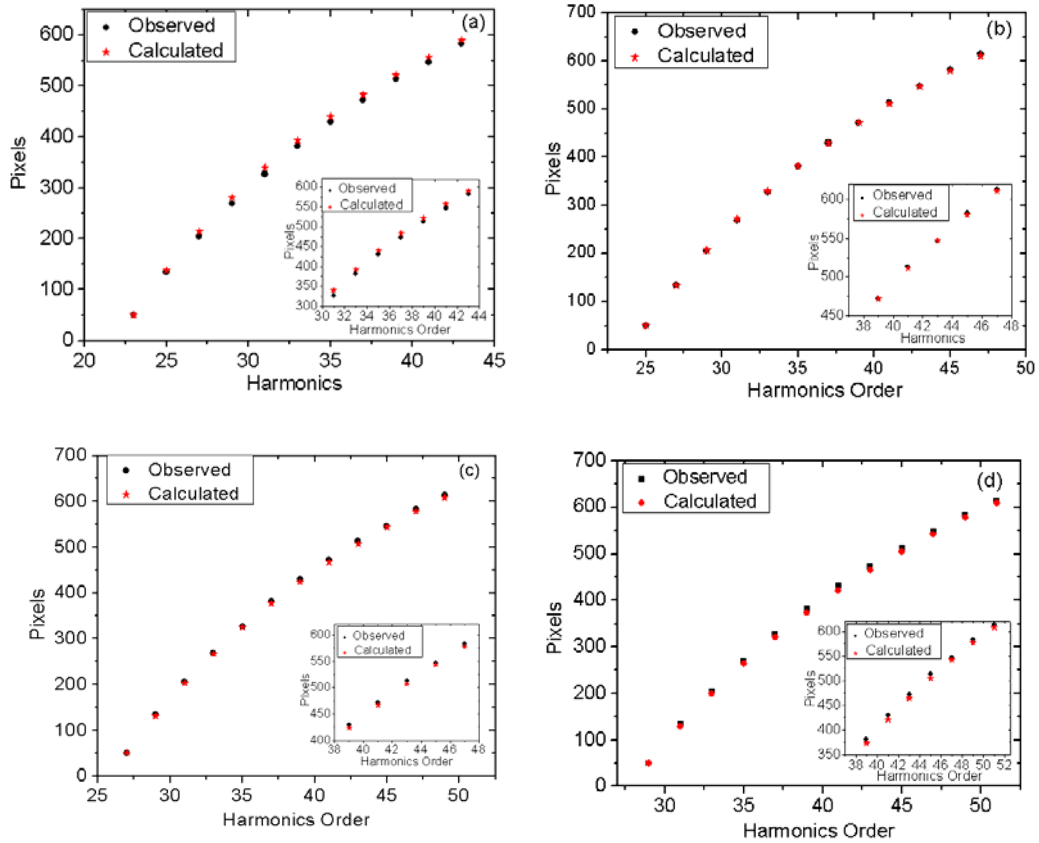
Fig 9.11 Calculated (red) and observed location of harmonics on phosphor screen when (a) 41st (b) 43rd (c) and (d) 47th harmonics were assumed to be Al cutoff in the Fig. 9.10. The inset shows the higher order harmonics of the corresponding figure with increased resolution.
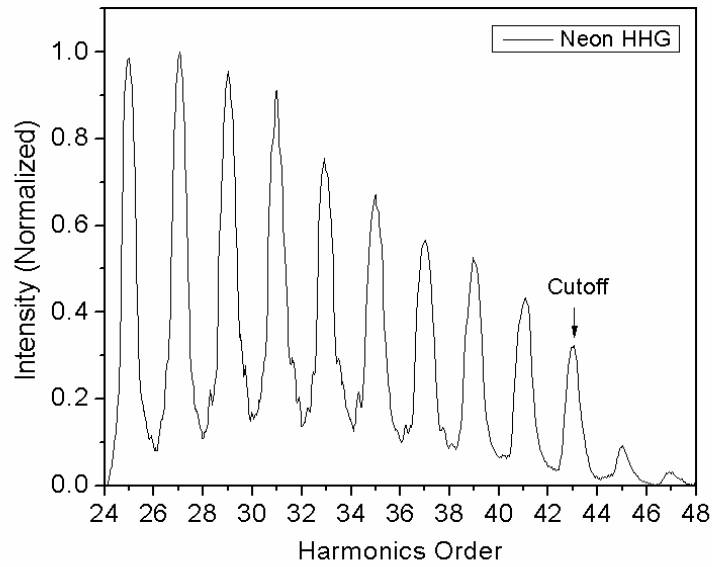
Fig 9.12 Calibrated neon harmonic signal of Fig. 9.9 in terms of harmonics order.
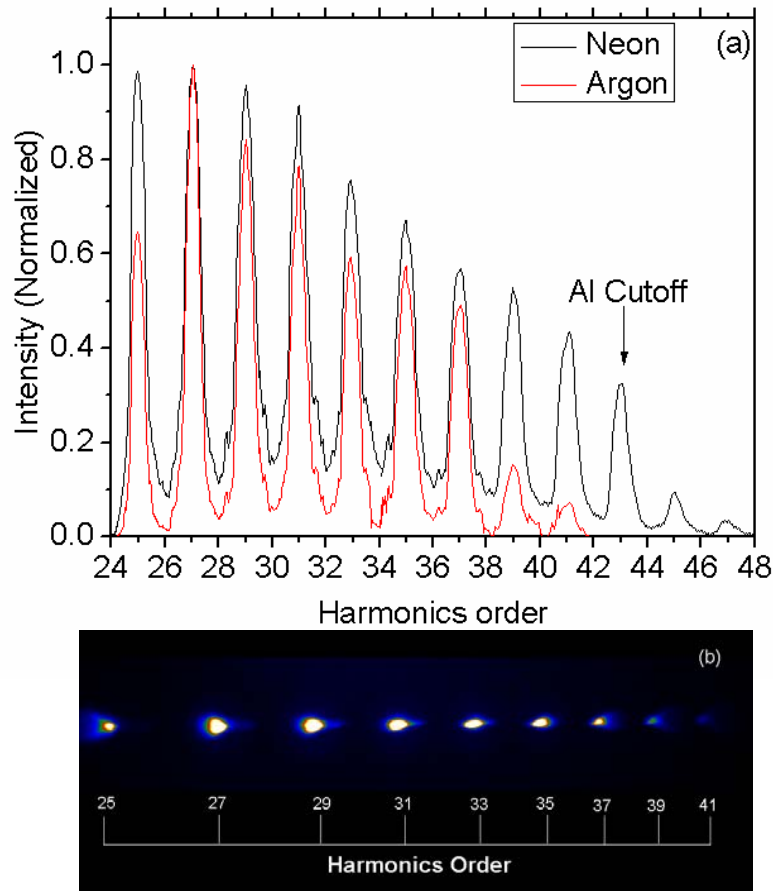
Fig 9.13 (a) Harmonics of argon fit into the harmonics of neon for calibration. (b) Calibrated harmonics image of argon with the help of (a).

Hence, the distance from H to the location of all the harmonics on the image plane and the separation between the consecutive harmonics can be calculated using the value obtained from the expression (9.4) with the value of pixel size per meter. Fitting of the calculated pixel position of the harmonics and the observed harmonics are shown in Fig.9.11 (a), (b), (c) and (d) when the cutoff transmission was assumed to be the 41st, 43rd, 45th and 47th harmonics respectively. It can clearly be seen that the calculated and observed peaks of the harmonics match the best when the 43rd harmonics was assumed to be the cutoff from the aluminum filter. Still, there exists small mismatching in the calculated and observed peaks in Fig.9.11 (b). This is not surprising as our calculation was based on the simplified assumption that the grating was flat, while the harmonics were resolved by a toroidal grating which is in fact not flat. Furthermore, error during the installation of the grating is very likely causing a difference in the real and input values in the calculation. However, from the fitting of the calculated and the observed values, it appears reasonably correct to choose 43rd harmonics as an Al cutoff. The cutoff harmonics on the other hand is a key for identifying the other harmonics peaks as depicted in Fig.9.12. As we used Ar gas as a nonlinear target for the harmonic generation process, calibration for the Ar harmonics spectrum was done with reference to the calibrated neon spectrum. Fig 9.13 (a) and (b) shows the localization of argon spectra with reference to the calibrated neon spectra of Fig.12. Harmonics were generated by focusing 30 fs , 1kHz and 0.8 watt laser onto the argon gas target with an off axis parabolic mirror of focal length 250 mm.

9.2 Single Shot Electronics Set-up

Although the technology of today can generate a laser pulse with a well-defined carrier frequency and envelope, the carrier envelope (CE) phase of those pulses is not stable. The CE phase is the measurement of the shift in the position of the peak of an electric field underneath the envelope with respect to the peak of the envelope. For a linearly polarized laser pulse, it is related by

$$\vec{E}(t) = \vec{E_0}A(t)\cos(\omega t + \phi_{CE}) \qquad (9.5)$$

where ϕ_{CE} is the CE phase of the pulse. $\vec{E_0}, \omega$ and $A(t)$ are the peak of the electric field, carrier frequency, and envelope of the pulse. The laser that we use in the lab with wavelength 800 nm has period per cycle 2.6 fs. The laser pulses with pulse duration greater than 10 fs therefore

consist of many optical cycles within the envelope. It can be seen from the expression (9.5) for the pulses with many cycles, change in the CE phase produces negligible change in the peak of the electric field. However, when the pulse becomes shorter, i.e. shorter than 10 fs, changes in the peak of the electric field due to change in the CE phase also become significant. Fig. 9.14 (a) and (b) shows a pulse with 4 fs pulse duration at CE phases $\phi_{CE} = 0$ and $\pi/2$ respectively.
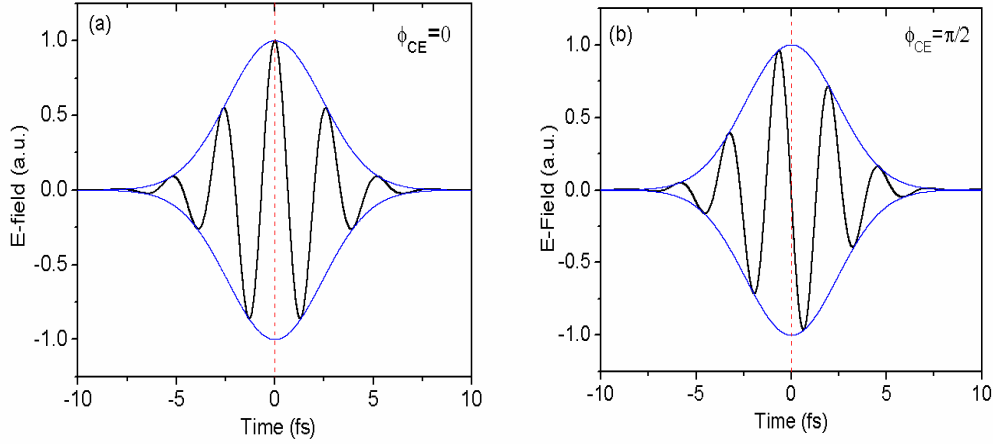
Fig 9.14 Laser electric field pulse of duration 4fs with CE phase (a) 0 (b) $\dfrac{\pi}{2}$

It can be observed from Fig.9.14 (b) when the CE phase is changed by $\pi/2$, the peak of the electric field also reduced by ~ 5% of the peak field at CE phase 0. It was predicted and later measured [48] this amount of change in the electric field due to change in the CE phase has quite significant consequences in highly nonlinear and strong field phenomena. Since output energy from the CE phase stabilized mode-locked laser oscillator is only tens of nJ, which is not high enough to stimulate strong field phenomena, the energy of the pulse has to be enhanced through the process of amplification. In the amplification process, a CE phase stabilized pulse from the oscillator has to pass through the dispersive media, which results in a random change in the peak of the electric field underneath the envelope with respect to the peak envelope in every amplified output laser pulse. In other words, the process of amplification of the pulses again introduces pulses with unstable CE phase. It is therefore very crucial also to stabilize the amplifier itself to generate intensified and stabilized output pulses in order to use them for triggering strong field phenomena. Current technology allows us to generate stabilized and intensified laser pulses to carry out the strong field experiment. After stabilization it is very important to measure the

absolute CE phase of the pulse. Although *f*-to-*2f* and phase meter based on above-threshold ionization [47] have been used to evaluate stability and measurement of the CE phase, the former cannot measure the absolute CE phase, while the latter has not yet been successful in measuring the shot-to-shot variation of the absolute CE phase. The reason for not being able to use the measurement of shot-to-shot change in the CE phase with Stereo-ATI is due to dominant space charge effect. If the shot-to-shot interaction of the laser field on the nonlinear medium in the study of strong field phenomena is required, measurement of the CE phase with the accumulation of several laser cycles will not give any information unless the CE phase of the laser is stabilized. As the XUV spectrum is highly sensitive to the pulse- to- pulse change in the CE phase, we take advantage of this co-relation in order to measure the absolute CE phase of the driving field. Fig. 9.15 illustrates our setup and method of capturing the shot-to-shot change in the XUV spectrum caused by the change in CE phase from the CE phase unstabilized amplifier and the oscillator. The phosphor screen was made to turn on once per 1000 laser pulses per sec and synchronized with a laser pulse from the Pockels cell. This is accomplished by a triggering pulse generator (565 Series BNC pulse generator). When one of the output channels of the BNC is in duty cycle mode, it will generate a continuous stream of pulses which can be made to oscillate on for "n" pulses and off for "m" pulses. By setting "n" to 1 and "m" to 999, one pulse
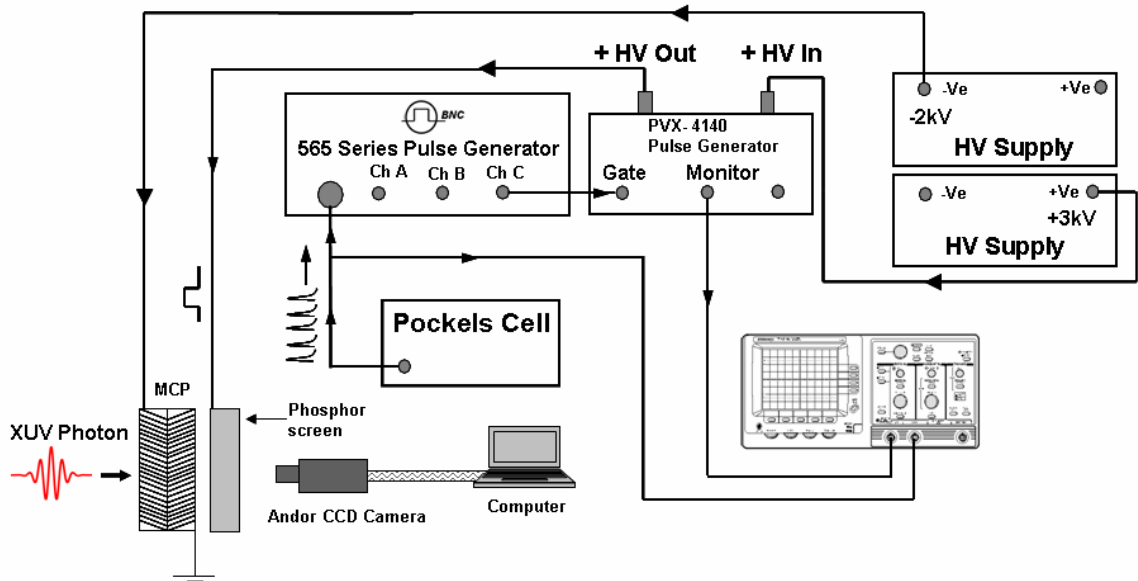
Fig 9.15 Schematic setup of the gated phosphor screen. Gate pulse of one pulse per second allows phosphor to image harmonics generated by a single laser pulse per second.

out of 1000 pulses per second from the Pockels cell, it will supply a gate signal per 1000 laser pulse to high voltage PVX-4140. As the PVX-4140 pulse generator is designed to produce high pulse voltage up to ± 3.5 kV with rise and fall time 25ns, with the settings mentioned above this
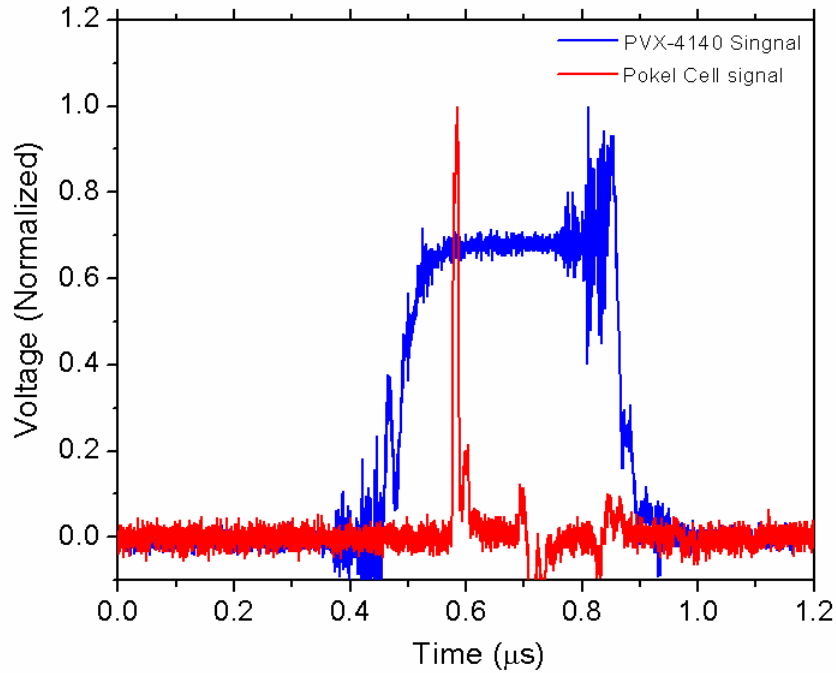
Fig 9.16 Output gate pulse (blue curve) from PVX-4140 synchronized with one of the pulses out of 1000 pulses/sec from the Pockels output. Since this laser is the driving field which generates harmonics, to study harmonics generation by single pulse per sec, all 999 pulses of the laser should be killed and trigger the gate of PVX-4140 from the single output pulse per sec from BNC. PVX-4140 then supplies a high voltage pulse synchronized with one of the laser pulses out of 1000 pulses/sec to the phosphor screen.
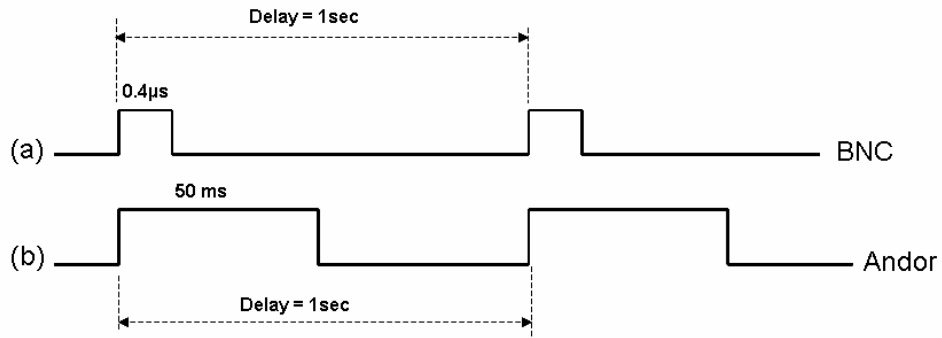
Fig 9.17 Optimized exposure time and delay between two pulses from (a) BNC pulse generator and Andor CCD camera to capture shot-to-shot change in XUV spectrum due to change in CE phase of the laser.

95

allows the phosphor screen of the MCP detector to turn on once per 1000 laser pulses/sec by a high DC voltage delivered by a high voltage power supply (Model PS350/5000V-25W). By adjusting the desired delay and the width of the pulse with BNC, an on-pulse can be synchronized to a pulse coming from the Pockels cell (Fig. 9.17). Once all those parameters have been set, an internally triggered Andor CCD camera set to the exposure time 50 ms and delay 1sec (Fig.9.17) captures the single shot XUV spectrum.

9.3. Hollow core fiber set-up and short pulse for single shot experiment

As our goal is to study the effect of the CE phase on XUV super-continuum, only one electron return and re-collision with the parent ion should be made possible. Single electron re-
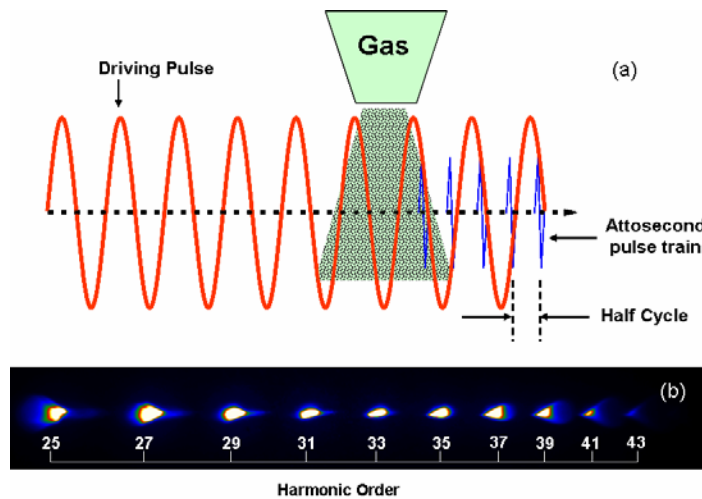
Fig 9.18 (a) Schematics to illustrate the burst of a train of attosecond pulse separated by half the optical cycle. (b) Harmonics from neon gas generated by a long laser pulse of duration 30 fs and 1kHz .

collision with the parent ion then produces a broad supercontinuum in the spectral domain, which corresponds to the emission of a single attosecond pulse. A laser pulse with many cycles (one optical cycle 2.6 fs) generates a train of attosecond pulses separated by half the optical cycles (Fig. 9.19), resulting in the generation of harmonics in the spectral domain. It then turns out that if we can allow only one electron to re-collide with the parent ion and prevent all the rest of the returning electrons from re-collision with the parent ion, it can produce a single attosecond

pulse which corresponds to the broad super-continuum. In order to have only one electron return and re-collide with the parent ion, the pulse duration of the driving field should be made less than half the optical cycle (τ<1.3), which is apparently not possible. However, if we look at the expression given by (8.30), the gate width T_G can be made less than one optical cycle by reducing the pulse duration τ of the laser pulse. The gate width T_G as we have defined earlier is the temporal width within which harmonic generation is possible. T_G less than half the optical cycle therefore should generate a super-continuum. in the spectral domain Now, the question is how short do we need the pulse duration to see the super continuum spectrum? This might quite well be answered by looking at Fig.8.18 (b), which tells us if we use a quartz plate of the thickness 0.5 mm, a short pulse of 7 fs second should be enough to synthesize a gate width less than half the optical cycle.

In order to achieve pulse duration as short as 7 fs, we use a pulse compression technique by using a hollow core fiber (Fig.9.19). A hollow glass waveguide of 90 cm long, 0.6 cm diameter,
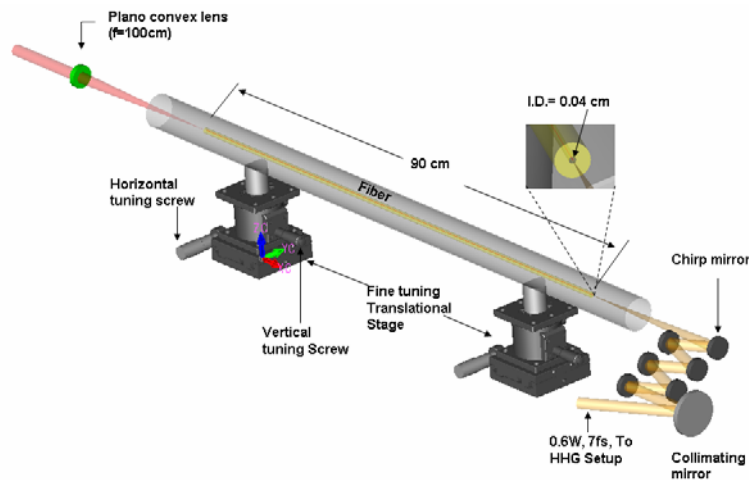
Fig 9.19 KLS hollow core argon fiber setup, which routinely produces 0.6W and 7fs pulse duration for the single shot measurement of XUV spectrum.

and 0.04 cm inner diameter hole along the longitudinal axis, was enclosed by a stainless steel tube of about 2.5 cm diameter. Two ends of the tube were closed by the 0.5 mm thick anti-reflection coated fused silica window. The whole setup is mounted on two translational stages placed 45 cm apart, which allows us to fine tune the fiber along the vertical and horizontal directions perpendicular to the direction of propagation of the beam. A plano-convex lens of focal length 100 cm focuses about 1.2 W laser from beam line 2 of the Kansas Light Source. The

focused beam should be coupled and aligned properly with the fiber with the help of a fine tuned translational stage. Proper alignment with the optimized pressure (~1bar) can generate coupling efficiency of ~80% with a good mode and broad spectrum.

The spectral broadening of the well optimized hollow core fiber is caused by Self-Phase Modulation (SPM). As it is clear from the name, the phase of an intense laser undergoes modification due to its own presence. The change in phase in fact is caused due to change in the refractive index when an intense laser pulse propagates in the nonlinear medium. The change in refractive index with intensity, known as the optical Kerr effect, can be expressed as:

$$n(I) = n_0 + n_2 \bullet I(t) \tag{9.6}$$

where, n_0 is the linear refractive index, and n_2 is the second-order nonlinear refractive index of the medium. If we assume time dependent intensity, which seems quite reasonable for the laser pulses as it is approximately Gaussian, we can modify relation (9.6) as

$$n(t) = n_0 + n_2 \bullet I(t) \tag{9.7}$$

This relation allows us to write the temporal phase $\phi(t)$ as

$$\phi(t) = -\frac{2\pi}{\lambda_0} n(t)L = -\frac{2\pi}{\lambda_0}[n_0 + n_2 I(t)]L \tag{9.8}$$

This leads to

$$\omega(t) = \frac{d\phi(t)}{dt} = -\frac{2\pi}{\lambda_0} n_2 L \frac{dI(t)}{dt} \tag{9.9}$$

where, $\omega(t)$ is the frequency and L is the length of the nonlinear medium along the laser propagation direction. For a Gaussian pulse, the time dependent intensity is given by

$$I(t) = I_0 e^{-2at^2} \tag{9.10}$$

where, $a_0 = \dfrac{2\ln(2)}{\tau^2}$ and τ is the pulse duration.

Using (9.10) in the expression (9.9) for the peak of the pulse, at $t \to 0$, boils down to the equation,

$$\omega(t) = \frac{8\pi\, a_0\, n_2\, I_0\, L}{\lambda_0} t = 2bt \tag{9.11}$$

where $b = \dfrac{4\pi a\, n_2\, I_0\, L}{\lambda_0}$ is the chirp parameter.

The frequency bandwidth due to SPM is related to the chirp parameter by

$$\Delta f_{spm} = \frac{\sqrt{2\ln(2)}}{\pi}\sqrt{a_0[1+\left(\frac{b}{a_0}\right)^2]} = \Delta f_{ini}\sqrt{[1+\left(\frac{b}{a_0}\right)^2]}$$

$$\therefore \frac{\Delta f_{spm}}{\Delta f_{ini}} = \sqrt{[1+\left(\frac{b}{a_0}\right)^2]} \tag{9.12}$$

For Ar gas [59], $n_2/p = 9.8\times10^{-20}$ cm^2/W-bar. Where p is the Ar gas pressure. A laser of 30 fs pulse duration790 nm and central wavelength as it propagates through the Ar gas of length 90 cm (non linear medium) at 1bar, $b \gg a_o$, therefore, from (9.12) spectral broadening factor $\Delta f_{spm}/\Delta f_{ini} \gg 1$. Hence, the output spectrum from the hollow core fiber becomes many times broader than the input spectrum.

Output from the argon hollow core fiber is then collimated with a concave spherical mirror of 1.5 m focal length. The beam after collimation is allowed to undergo 2 pairs reflection, each 50 fs^2 on the first pair, 2 pairs of reflections on the second and third pair of chirp mirrors, each 60 fs^2, giving total negative dispersion of -340 fs^2. This negative dispersion should be compensated by introducing material of positive dispersion on the beam path. The thickness of materials on its path, which is fixed, are 2 mm of quarter wave plate, 0.5 mm of quartz plate, 0.5 mm of the entrance window and 4 meters of air (~4mm of fused silica) giving a total of 7 mm of materials. However, in order to compensate -340 fs^2, the required thickness is 340/36 = 9.4 mm. So, by using a pair of finely tunable wedges, the required extra amount can be introduced in order to generate the shortest pulse possible.
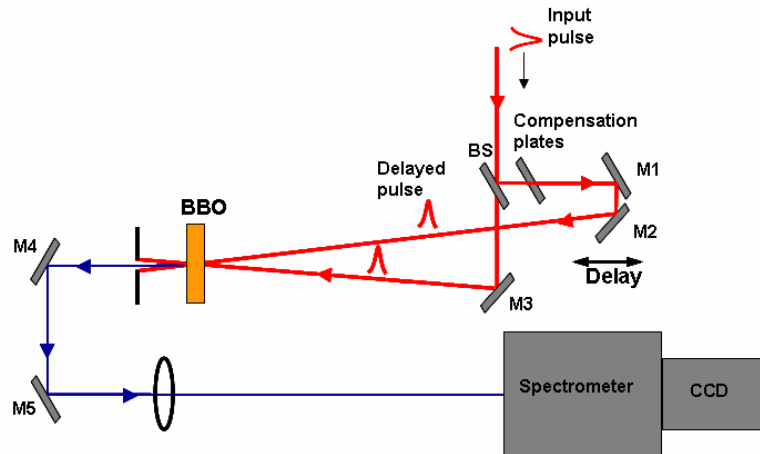
Fig 9.20. Schematics of KLS Frequency Resolved Optical Gating (FROG) to measure pulse duration of a few cycle pulses

The pulse duration was measured by a technique called Frequency Resolved Optical Gating (FROG). Schematics of the KLS FROG setup are shown in Fig. 9.20. A compressed pulse from the hollow core fiber was split by a 50/50 beam splitter (BS). A reflected beam, from the BS, first propagates through the compensation plate, and then undergoes further successive reflection through mirrors M1 and M2 of the delay stage. The other transmitted beam from BS
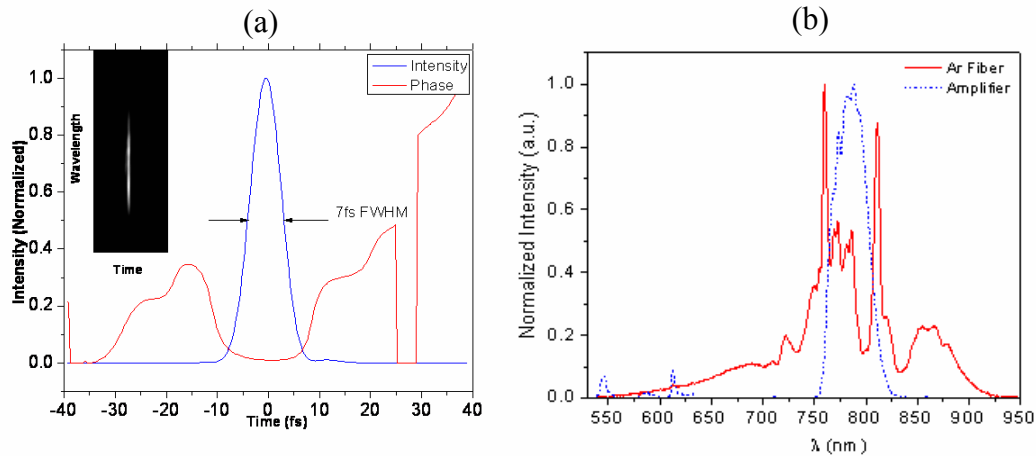
Fig 9.21(a) 7fs pulse output from the argon hollow core fiber measured with KLS SHG FROG. (b) Measured input spectrum (blue dashed curve) broaden by from argon filled hollow fiber (red curve). Hollow core fiber routinely produces 0.6 W and 7fs out put after chirp mirrors with the input of 1.1W and 25 fs.

was reflected through M3 and overlapped temporally and spatially with the beam reflected through M2 at a 10μm thick BBO crystal. The reason for using such a thin nonlinear crystal is that it has sufficient bandwidth, which is inversely proportional to the crystal thickness. This choice allows us to measure pulse duration less than 10 fs. A typical FROG trace of pulse output from an argon hollow core fiber routinely observed with the above mentioned optimizations is shown in Fig. 9.21(a).

9.4 Stabilizing the carrier-envelope phase of laser pulses

Had there been a cavity which had dispersive media fixed (mechanical vibration, temperature fluctuation, unfixed cavity length, air current fluctuation, laser intensity fluctuation, lasing medium etc.), the pulse train produced from the oscillator would not have different carrier envelope (CE) phase. In other words, the position of the peak of the carrier field with respect to the peak envelope in every pulse will not be at a different position. This is possible only if the

cavity can be isolated completely from external disturbances, which is of course not feasible practically. The pulse-to-pulse evolutions of the CE phase in the time domain can be observed in the frequency domain as a shift in frequency comb. If we assume $\Delta\Phi_{CE}$ to be the amount of shot-to-shot CE phase evolution, the shift of the frequency can be estimated by $f_0 = f_{rep}\Delta\Phi_{CE}/2\pi$, where f_{rep} is the separation between the two combs, and f_0 is the frequency offset due to the disturbances. Stabilization of the CE phase requires locking $\Delta\Phi_{CE}$ in the frequency domain, which consists of detecting f_0 and synthesizing the feedback signal from this to lock to a desired value. The simplest method of detecting f_0 is the method of so-called self–referencing [66, 67], which consist, of the octave-spanning spectrum described here.
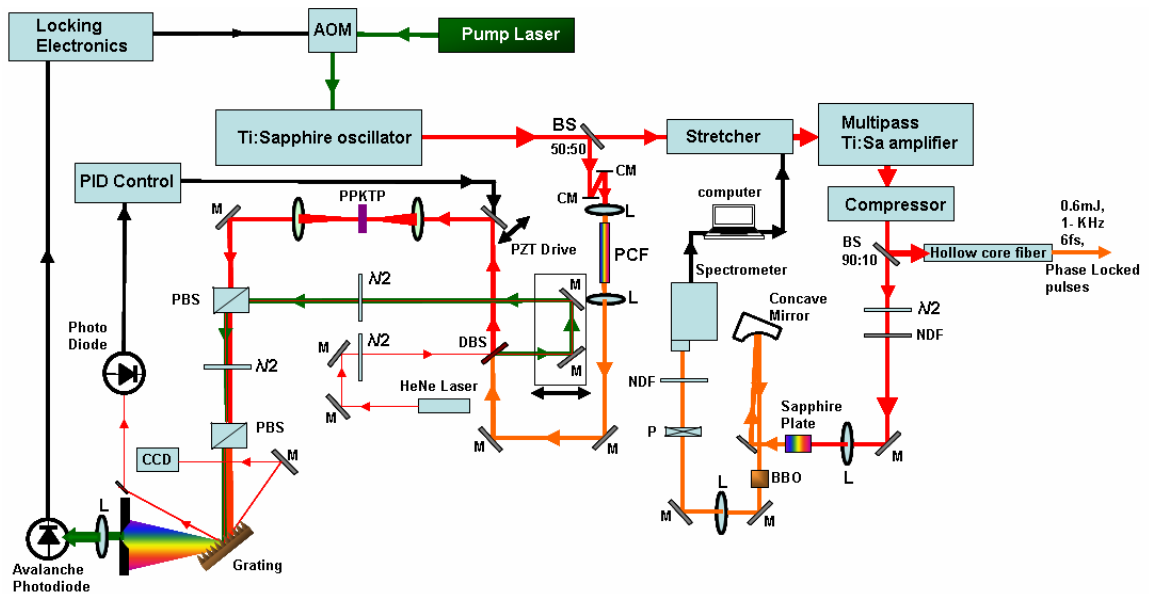
Fig 9.22 KLS System for stabilizing oscillator and amplifier. AOM, acousto-optic modulator; BS, Beam splitter; PBS, polarization beam splitter; PCF, photonic crystal fiber; CM, chirped mirror; PPKTP, periodic poled potassium titanyl phosphate; P, polarizer; L, lens; BBO, β-Barium Borate; M, silver mirror; DBS, dichroic beam splitter.

The Kansas Light Source has a Kerr-lens mode-locked Titanium:Sapphire laser oscillator delivering 12 fs pulses with an energy of about 2.6 nJ at a repetition rate of approximately 77 MHz (Appendix). A portion of the output beam from the Ti:Sapphire oscillator is split off and coupled into a photonic crystal fiber (PCF), which generates the octave-spanning spectrum that contains the long wavelength portion 1064 nm (f) and the short wavelength portion 532 nm

101

($2f$) components (Fig 9.23). A dichroic beam splitter separates the f and $2f$ components. An f component is frequency-doubled ($2f$') in a periodically poled potassium-titanyl phosphate (PPKTP) and temporally interfered with by the original shortwave length portion $2f$ in order to generate a beat frequency. Extraction of the beat frequency was done with a grating and then filtered with an aperture. The beat frequency which is in the MHz range can easily be detectable with an avalanche photodiode and electronic signal processing. A change of the value of beat frequency directly manifests the pulse-to-pulse phase shift. So, by stabilizing the beat frequency to a certain value one can produce a well-defined phase drift or no phase drift. This beat frequency can be used to synthesize a feedback signal to lock the CE phase drift. The feedback signal in combination with the locking electronics controls the acousto-optic modulator (AOM), which in turn changes the pump beam intensity. Since the CE phase of the oscillator depends on its pump beam intensity, this mechanism eventually stabilizes the CE phase. Since the CE phase stabilized oscillator output has very low intensity, in order to boost intensity, the output of the oscillator has to be amplified with the process called chirp pulse amplification (CPA). In this amplification process, the oscillator output seeds the multipass chirp pulse Ti:Sapphire amplifier. So the output pulses after amplification lose their phase stability as the pulse suffers phase drift inside the amplifier during the time of seeding. Corrections to the CE phase drift of the amplified pulses were made by sending 10% of the output from the amplifier to another *f*-to-*2f* interferometer. As the amplified laser has higher enough intensity to generate a non-linear effect, a thin sapphire plate can be used to broaden the spectrum. To broaden the spectrum, a sapphire plate was used as a non-linear medium. By introducing the frequency doubling crystal, SHG pulses were generated, and the interference pattern of $2f$ from the SHG pulse and that from the output of the sapphire plate can be observed through a grating spectrometer coupled with a CCD camera. Now our objective boils down to the stabilization of interference, which on the other hand corresponds to the stabilization of the CE phase of the amplified pulses. A shift of one fringe in the interferrogram is equivalent to a CE phase drift of 2π. A computer records the interference patterns and feeds back a signal to control the separation of the grating in the stretcher, which compensates the phase drift caused during the multipass amplification process.

9.5 Phase Matching Of HHG

The phase mismatch between harmonic waves emitted at the focus (z = 0) and z > 0 is caused by the difference between the phase velocities of the driving laser field and the high harmonic wave in the nonlinear medium. Phase velocities of the generated harmonics are barely affected, as the refractive index is almost unity for the XUV wavelength. Efficiency of the harmonic radiation strongly depends on the condition of the phase matching. In the course of propagation, the harmonics encounter three main contributions to the phase.

a) Geometrical phase shift in the focus of a Gaussian beam, the so-called Guoy phase shift. The Guoy phase shift is the result of the transition of a wavefront from a negative radius of curvature over a plane front to a positive radius of curvature. If the laser is focused to a waist at $z = 0$, the phase difference between the driving polarization at $q\omega$ and the q th-harmonic field is given by

$$\Delta\phi(z) = \Delta k_q z + (q-1) Tan^{-1}(2z/b) \tag{9.13}$$

where k is the propagation vector, b is the confocal parameter, and $\Delta k_q = k_q - qk_1$. k_q and k_1 are the propagation vector of the qth and the fundamental propagation vector. As the beam propagates, the phase difference accumulated between two planes z_2, z_1 is

$$\delta\Delta\phi(z) = \Delta\phi(z_2) - \Delta\phi(z_1) \tag{9.14}$$

Equation (9.14) can therefore be written as

$$\delta\Delta\phi(z_0) = \frac{d}{dz}\Delta\phi\Big|_{z=z_0} \Delta z_0 = \left[\Delta k_q + (q-1)\frac{2}{b}\frac{1}{1+(2z_0/b)^2}\right]\Delta z \tag{9.15}$$

If we assume that the refractive index of the qth harmonics n_q is equal to that of the fundamental n_1, which leads to $k_q = qk_1$, i.e. $\Delta k_q = 0$, expression (9.15) can be written as

$$\delta\Delta\phi(z_0)\Big|_{z=z_0} = (q-1)\frac{2}{b}\frac{\Delta z}{1+(2z_0/b)^2} \tag{9.16}$$

Now if we define the coherence length as a distance in which the driving field and the qth harmonics get out of phase by π radians, then we can replace $\Delta z = z_2 - z_1$ by L_g such that $|\delta\Delta\phi| = \pi$. The coherence length therefore can be written as

$$L_g = \frac{\pi b}{2(q-1)}\left[1 + (2z_0/b)^2\right] \tag{9.17}$$

So it is clear from expression (9.17) that the coherence length depends on the focusing geometry, i.e. confocal parameter b. For a fixed value of b, coherence length L_g can be increased by increasing the distance z_0 from the focus. This is in fact advantageous if one has sufficiently high intensity in order to generate harmonics with high efficiency. The reason will be clear to us if we derive intensity $I(z_0)$ in terms of the distance z_0 from the focus. Intensity of a Gaussian pulse at z_0 with power P and waist $w(z_0)$ can be expressed as

$$I = \frac{2P}{\pi\,w(z_0)^2} \tag{9.18}$$

where $w(z_0)$ is given by

$$w(z_0) = w(0)\sqrt{1 + (z_0/z_R)^2} = w(0)\sqrt{1 + (2z_0/2z_R)^2} = w(0)\sqrt{1 + (2z_0/b)^2} \tag{9.19}$$

We know that $z_R = \pi\,w(0)^2/\lambda$, which yields $w(0)^2 = \lambda z_R/\pi$. Using this in (9.18) gives

$$I = \frac{2P}{\pi\,\lambda z_R/\pi}\frac{1}{[1 + (2z_0/b)^2]} = \frac{4P}{\lambda(2z_R)}\frac{1}{[1 + (2z_0/b)^2]} \tag{9.19a}$$

$$\therefore I = \frac{4P}{\lambda b}\frac{1}{[1 + (2z_0/b)^2]} \tag{9.19 b}$$

Hence, from (9.19 b) it can be seen that intensity decreases with distance z_0. The confocal parameter is defined by the f-number f/D of the focusing optics (focal length f)

through $b = 2\pi\lambda[f/D]^2$. For Gaussian-beam focusing $D = \pi w$. In order to achieve longer confocal length, it is therefore obvious that either f or D should be changed. Space available in the lab constrains the flexibility in increasing the focal length f. As there is enough space for changing the position of the collimating mirror after the hollow fiber, D can be adjusted to increase b, which allows us to increase the efficiency of the high harmonic generation. This became very important to make the single-shot experiment possible.

b) Another parameter which affects the phase matching is the dispersion phase due to neutral atoms, free electrons and ions. Since recombination probabilities are less than the rate the electrons generate during ionization, during the process of ionization, more free electrons are generated than they contribute to the HHG generation. Since a free electron has a negative refractive index, it will affect the phase velocity of the fundamental beam. The dephasing length L_d due to this contribution can be written as

$$L_d = \frac{2\pi c\,\omega_0}{N\,\omega_p^2}$$

(9.20)

where $\omega_p = \sqrt{e^2 n_e/m\varepsilon_0}$ is the plasma frequency and n_e, ε_0, e and m is the electron density., permittivity in the free space and mass of an electron respectively. As the dispersion due to neutral atoms and the dispersion due to plasma have opposite signs, phase mismatching can be achieved by introducing neutral atoms into the targets i.e. by adjusting the pressure. Since phase matching can be achieved by adjusting the phase velocity of the fundamental and the harmonics radiation, phase matching bandwidth should be very broad comprising many harmonic orders. Due to this broad bandwidth for the phase matching, it is possible to achieve the phase matching condition even if the ionization undergoes rapid changing during a pulse. Once harmonics and fundamental are phase matched, the intensity of the harmonics scales quadratically with an increase in pressure. However, this enhancement of the intensity with pressure is limited by the ionization, called critical ionization [60]. As ionization increases, the dispersion due to the plasma also exceeds that due to the neutral atom, and phase matching by increasing the target pressure no longer exists.Shown in Fig 9.23 are the measured HHG signals from an argon target when the gas cell was located at two different positions. The result shows

the spatial dependence of the phase matching when the target was shifted in its relative positions. This kind of test was possible in our case because we used a thin gas cell (1.44 mm diameter) compared to the confocal parameter (6.8 mm). Estimation of the position of the cell with respect
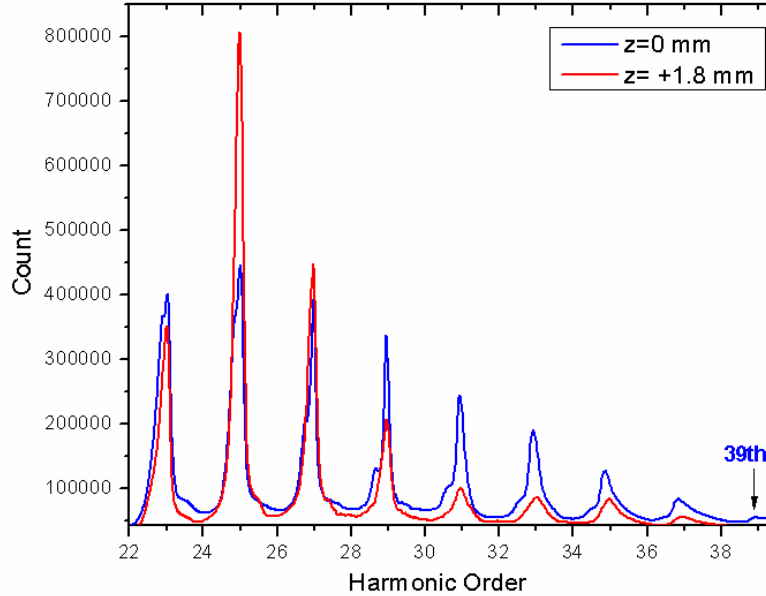
Fig 9.23 Measured HHG spectra in argon for a gas cell located in the focus (z = 0, red line) and after the focus (z = +1.8 mm, blue line). The difference in the spectrum is caused by the different phase matching conditions.

to the focus was possible since the gas fluorescence due to ionization was clearly visible. This allows us to adjust the position of the gas cell within the Raleigh range (confocal parameter = twice the Raleigh range). As the target pressure used during the time of observation was very low, i.e. 15 torr, the effect of dispersion can be neglected. It therefore turns out that the Gouy phases and atomic phases have played a crucial role in compensating each other. Two prominent features can be noted from Fig. 9.23: (a) higher HHG efficiency after the focus; (b) higher HHG extension at the focus but lower efficiency. Effects (a) and (b) are consistent with the theory. As the coherence length for the Guoy effect (9.17) becomes longer as the cell is moved away from the focus, effect (a) is obvious. Effect (b) is due to higher intensity at the focus ($h\omega_{cutoff} = 9.35 \times 10^{-14} I \lambda^2 + I_p$). This kind of measurement is very important if one does a single-shot experiment. If higher harmonic efficiency were used, that would generate better signal-to-noise ratio and good throughput in the spectrometer.

Shown in Fig. 9.24 are the polarization gated harmonics spectra at different target pressures taken over the integration of 500 laser shots. The average laser power from the hollow fiber was measured to be 0.6 Watt with the power fluctuation ~1%. The voltages on the microchannel plate and the phosphor screen were kept at -1.7kV and +2.5kV throughout the observation.
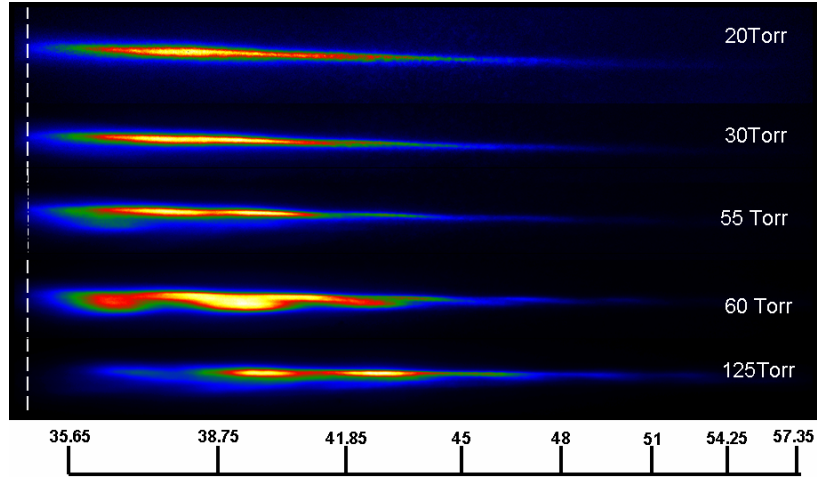
Fig 9.24 Polarization gated harmonics at different target pressures. The structure in the harmonic spectrum beyond the pressure 55 torr is due to the phase mismatching.
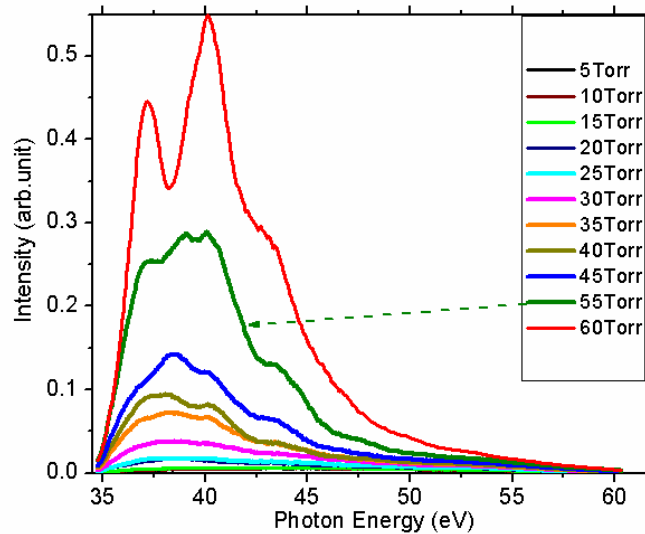
Fig 9.25 Polarization gated HHG spectrum at different pressures taken over 500 laser shots. The structure in the plot above 55 Torr is caused by phase mismatch.

The structures on the harmonics beyond pressure 55 Torr are caused by phase mismatch, as intensity no longer varies quadratically with pressure above this value. The gradual

disappearance of lower harmonics at the higher pressure is due to the absorption of the photon by argon gas. Fig.9.25 is the line out of the HHG spectrum at different pressures. As it can clearly be seen in the plot the less-curved structure modified into a curve with prominent structure as the pressure at the target was increased beyond 55 torr. For another test of the effect of gas pressure on the phase matching, we measured the normalized intensity of the polarization gated harmonics at different pressures as shown in Fig. 9.26. As we used a gas cell drilled by the laser itself about the size of the focal spot, the gas cell also provides the differential pressure system. This allowed us to study the effect of target pressure on the HHG signal intensity. The pressure can be varied from zero to 200 Torr with the pressure outside the gas cell less than 200 mT.
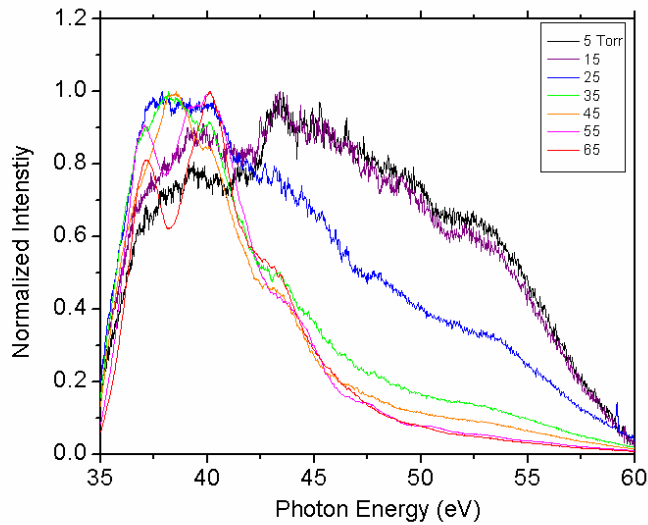
Fig 9.26 The dependence of the harmonic intensity on the target gas pressure. The continuum spectrum gradually becomes narrower as pressure is increased on the target due to plasma defocusing.

As we used 100 nm Al pressure, the chamber should be kept at less than 200 mT although our test shows that the aluminum filter can withstand over 300 mT of pressure. So, at a pressure of 60 Torr or beyond, the background pressure is less than 20 mT and quite small for the absorption of HHG photons on its path. The flat and broad spectrum at the low gas pressures in Fig. 9.26 provides better agreement in intensity. Since the addition of argon gas increases plasma density in the gas cell, which has negative refractive index, it creates negative lenses thereby defocusing the laser beam. Continuum spectrum gradually become narrower as pressure is increased on the target. Hence, at the higher pressure, the intensity at the focus therefore decreases causing flat portion of the XUV spectrum narrower.

9.6 Maximum Phase Matching Pressure and Experimental Result

The success of the single shot experiment depends on the ability to generate a sufficient number of photons per laser shot. As photons can easily be lost by several different processes mentioned above, careful investigation for finding the way to prevent this loss is a crucial part of this experiment. Every possible effort to boost the number of photons was carefully made when the apparatus was designed and built. Since our design has XUV divergence angle matched with the acceptance angle of the grating, throughput of this spectrometer cannot be poorer than any design claiming to have the best throughput, which does not have those two angles (divergence angle and acceptance angle) matched. Besides, the possibility of photon loss through absorption by the gas has almost been completely eliminated by keeping the pressure as low as 10^{-7} torr in the rest of the chamber. So any absorption can only take place in the interaction volume itself. Although it is necessary to have a design capable of preventing photon loss, it is not sufficient to expect good output signal from the single shot experiment unless sufficiently many photons are produced. It has been shown experimentally that the number of photons can be enhanced quadratically by increasing the pressure. However, we should not assume that harmonic
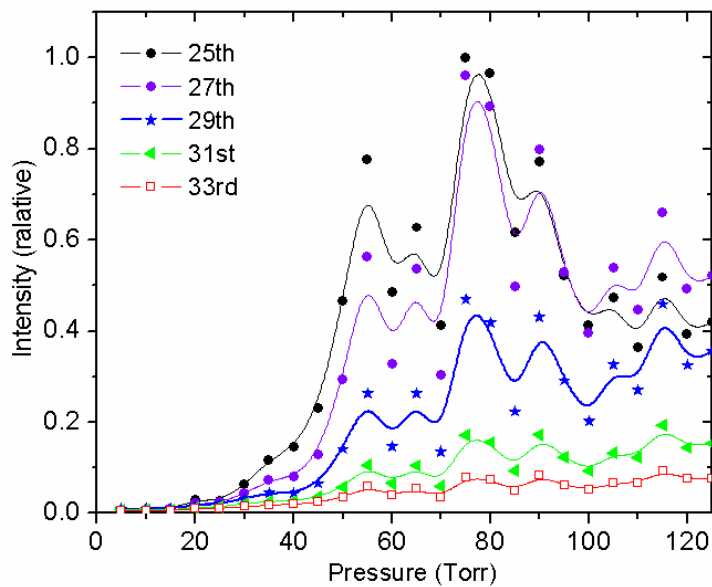
Fig 9.27 Variation in intensity of 25th, 27th, 29th, 31st and 33rd harmonics with pressure. Intensity scaled quadratically over pressure up to 55 Torr. Messy outlines beyond 55 torr indicate that phase matching no longer persists above this pressure.

efficiency can be increased as high as we want since the quadratic variation in intensity continues only up to certain value of pressure. As this value increases, harmonic efficiency degrades due to phase mismatching. It might therefore seem extremely important to find out the maximum pressure that can be used without losing the phase matching condition. As our design provides a knob to tune the pressure at the target, we took that advantage to measure the intensity of the harmonics at different target pressures. This leads us to the identification of the maximum pressure, which does not negatively affect the phase matching condition. Before the pressure scan was started, every optimization was made, which contributes to the better phase matching condition, such as locating the gas cell at 1.8 mm from z = 0 position, etc. Fig. 9.27 shows the measurement of the harmonic intensity with pressure. All the harmonics intensity scaled quadratically over the increase in pressure up to 55 torr. Beyond this value the variation is no longer quadratic. During the process of building up the coherent harmonics by the driving laser, both should travel with the same phase velocity over the extended propagation distance.
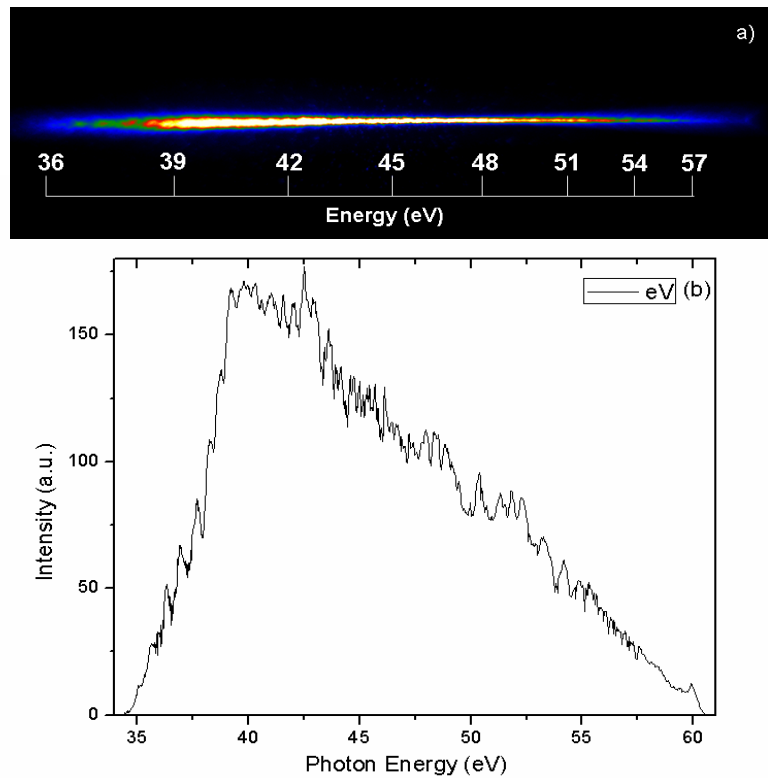
Fig 9.28 (a) Polarization gated XUV spectrum at maximum phase matching pressure 55 Torr (b) line out of (a) when gas cell is located at 1.8 mm and divergence angle of XUV matched with acceptance angle of the grating. Measured number of photons was 10^4 per laser shot.

When material is added to the medium, it will increase neutral atoms and plasma density. When the plasma density exceeds the neutral, atom density, this may cause the phase slip between harmonics and the fundamental, thereby decreasing the efficiency of harmonic generation. This phase slip may also become π out of phase, resulting in destructive interference. In this case the harmonic signal goes down to zero. This will however be true only when we assume the beam to be a point source. As the beam has finite size, two dimensional variations in intensity do not allow the harmonics signal to drop down to zero. The measured data in Fig. 9.27, with the absence of zero signals, intensity of harmonics agrees reasonably well with the explanation for the finite beam size. Fig. 9.28 is the polarization gated HHG spectrum when the target was located at 1.8 mm from the focus, with divergence angle matched with the acceptance angle and target pressure set to maximum phase matching pressure, i.e. 55 Torr. As our entire goal is to
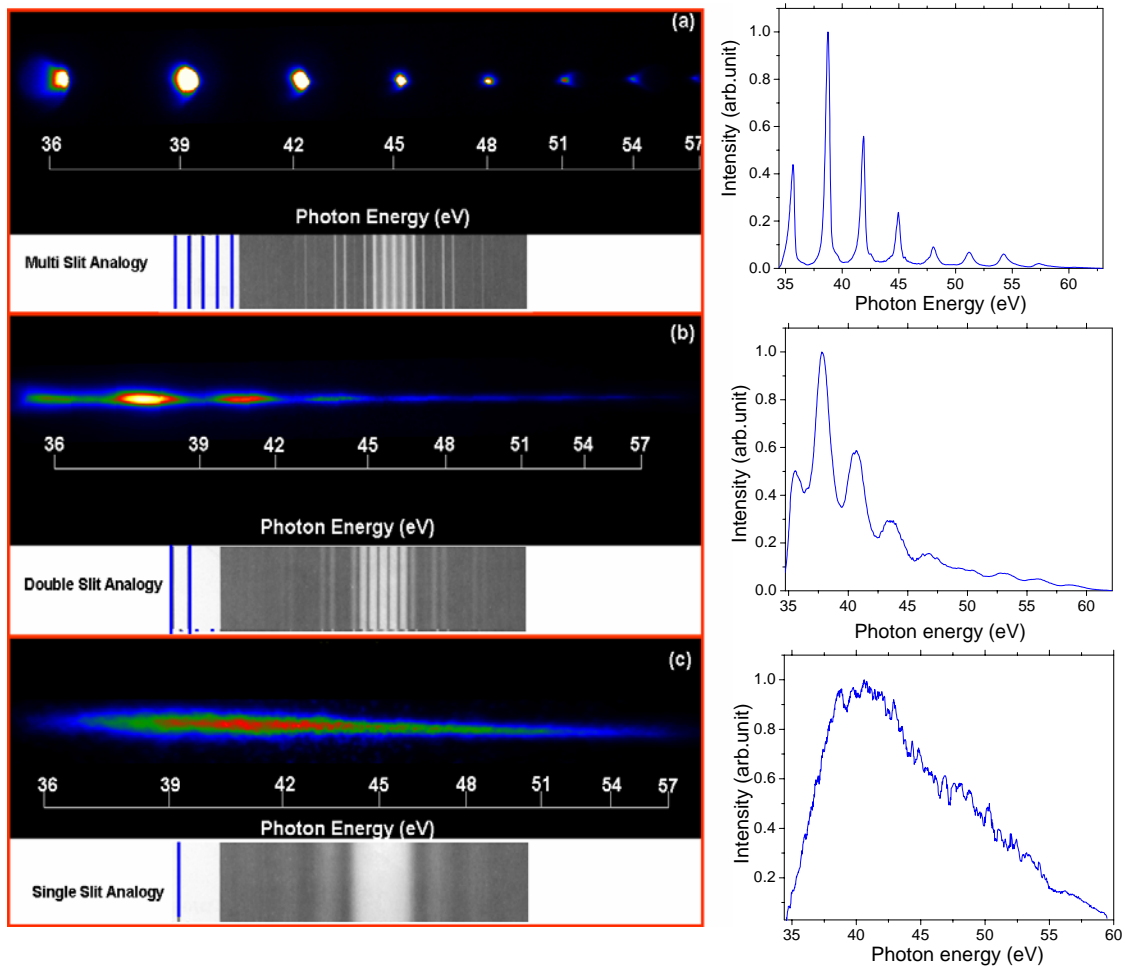
Fig 9.29 XUV spectra and its line out when input pulse is (a) 30 fs (b) 6fs and (c) polarization gated. The picture of diffraction of light from the different number of slits underneath the XUV spectra has been attached to show its analogy harmonic generation from laser pulse of different pulse duration.

study the effect of the carrier envelope phase (CE) on the XUV super-continuum generated by polarization gating, in order to see how the change in CE phase contributes to the XUV spectrum, we focus our effort to generate the XUV super-continuum from the polarization gating with the gate width as short as possible. Next, in an attempt to demonstrate the analogy of our experiment with the phenomenon of diffraction of light, we tried to compare the result of our experiment with the diffraction of light from different slits. In this regard, we first tested the evolution of the spectrum with the three different inputs:(a) linearly polarized long pulse of duration 30 fs , 1kHz and 0.8 W;(b) linearly polarized, compressed short pulse of duration 6fs,1kHz, and 0.6 W; (c) and finally the polarization gated pulse. In each step we tried to keep the polarization horizontal to the optical table as our toroidal grating gives highest efficiency when the polarization direction of the linear field is perpendicular to the grating lines.

Fig.9.29 (a), (b) and (c) on the left shows the XUV spectra generated from long pulse (~30fs), short pulse (~ 7fs) and polarization gated pulse. On the right is the corresponding line out of the spectrum. (a) and (b) are produced by integrating over 100 laser shots while (c) is the result of integration over 500 laser shots. It is evident that the requirement of increased laser shots to generate (c) is due to the contribution only from the narrow linear portion of the polarization gated pulse with the reduced intensity. The evolution of the XUV spectrum can clearly be seen with the change in the pulse duration, which complies with the phenomenon of diffraction of light from the slit. Harmonics generation with the long pulse corresponds to the interference of emission of radiation resulting from the re-collision of subsequently returning multiple electrons. The harmonics generation with the long pulse therefore resembles the diffraction of light from multiple slits where the pulse duration of the driving field serves here as slits. Reduction in the pulse duration corresponds to reduction in the slit number. So the result from (b) with the broader high harmonic spectrum agrees fairly well with the result of diffraction from the reduced slit. The broad spectrum with the absence of discrete harmonics in (c) can also be explained by diffraction theory. As in the single slit diffraction which constitutes the broad spectrum (figure underneath the HHG spectrum (c)), high order harmonics emission with polarization gating also takes place as a result of re-collision between either single or double electrons with the parent ion. Emission due to a single electron corresponds to the single slit. Hence, the spectrum appears as a super-continuum in the frequency domain. When emission is
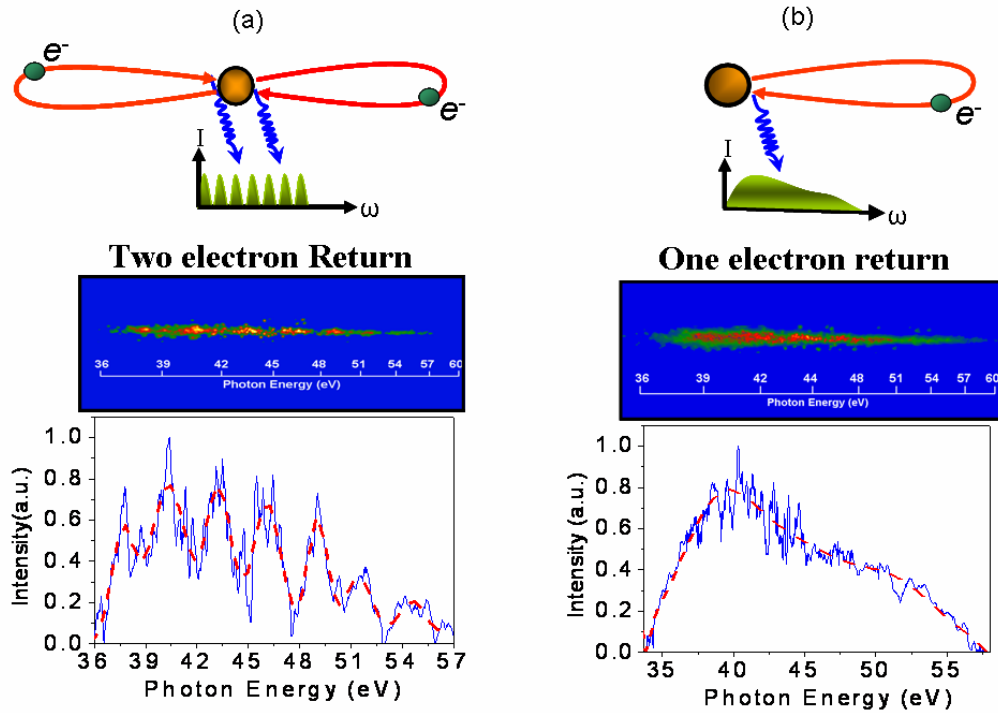
Fig 9.30 Single shot (a) discrete (b) supercontinuum XUV spectrum. Discrete spectrum and the super continuum are the result of driving field with CE phase 0 and π/2 respectively.
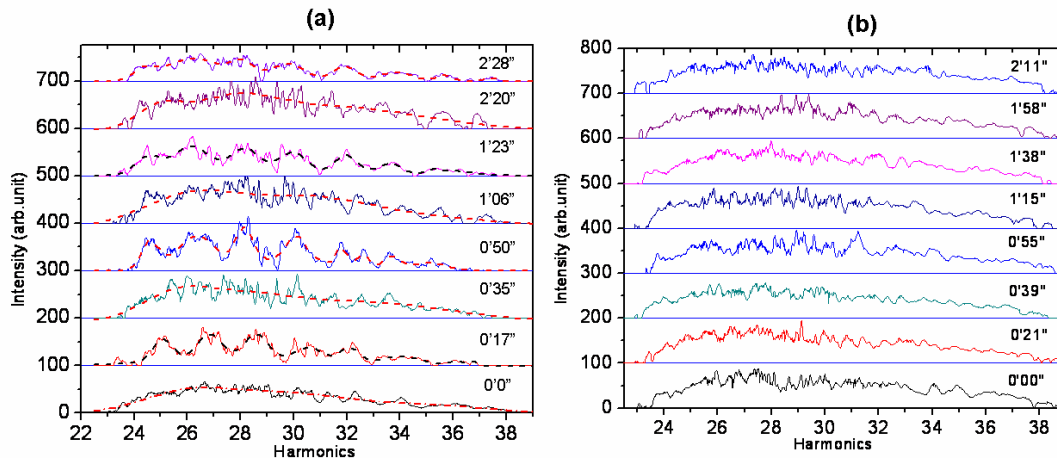
Fig 9.31 Single shot polarization gated XUV spectrum observed at maximum phase matched pressure when CE phase of the driving field was (a) unlocked (b) locked. The number of photons per laser shot was measured to be 10^4.

governed by the re-collision of double electron return, the spectrum should look like an interference pattern as in Young's double slit experiment. On the contrary, the XUV spectrum in the frequency domain does not appear discrete unless the spectrum is recorded with each lesser

shot. To resolve the spectrum into discrete harmonics taken over integration of multiple laser shots, the carrier envelope (CE) phase of the driving field should be locked (will be explained in detail shortly). The extreme sensitivity of the XUV spectrum to the carrier envelope phase of the driving laser field therefore provides a key for the measurement of the absolute CE phase. Fig. 9.30 (a) and (b) is the single shot discrete spectrum at the maximum phase matching pressure with all other parameters optimized to achieve better phase matching conditions. Obviously, Fig.9.30 (a) is the result of the interference of the emission of double electron return, which agrees well with the theory explained in section 8.5. We believe subsequent emission of two electron returns is due to the driving laser field which has CE phase ϕ_{CE} equal to zero. Fig.9.30 (b) is the super-continuum spectrum which is the result of the emission due to single electron return when the CE phase of the driving field changed to $\pi/2$. Shown in Fig.9.31 (a) and (b) are the single shot XUV spectrum when CE phase was unlocked and locked. When the CE phase was unlocked, XUV spectra for some shots are discrete harmonics and for other shots continuum. The data presented in Fig. 9.31 has been measured by using a laser pulse of duration 7fs from the compressed hollow core fiber and quartz plate of thickness 0.5 mm, which produces the delay between the two circularly polarized pulses of 15 fs and the gate width 0.96 fs. The continuum spectrum from some shots when the CE phase was unlocked can be attributable to the effect of the laser field with its CE phase $\pi/2$. This information therefore provides an important basis for the measurement of the absolute CE phase of the laser which does not have a CE phase locking system. Further evidence of the effect of the CE phase on the XUV spectrum has been observed when the CE phase was locked. Sequences of an observed XUV spectrum with near-absence of modulation in our recorded data over 2 minutes presented in Fig.9.31 (b) confirms that the shot-to-shot change in the XUV spectrum is purely due to the shot-to-shot change in the CE phase of the driving field. Since the number of photons available is limited and the signal-to-noise ratio is poor, statistical noise has been observed as fine structures on the top of the spectrum and of course not due to the effect of the CE phase of the driving laser field.

9.7. Experimental set-up to study effect of CE phase on polarization gated multi-shot XUV super-continuum.

As single shot data correlates with large statistical noise, detailed analysis of the shot-to-shot effect of the CE phase on XUV is very difficult to compare with the polarization gated high

harmonic spectra obtained by numerical simulations in Fig.8.20, although the effect of CE phase on the polarization gated super-continuum can be observed. In order to observe the effect of the carrier shift with respect to the envelope, there is no alternative method than to record the pulse-to-pulse evolution of the XUV spectrum generated by single or double electron ion re-collision, unless the CE phase of the driving laser field can be locked for a certain period of time. If the spectrum were produced by acquiring data over many pulses, it would not provide any information other than average effect of interaction with matter due to randomly varying CE phase with respect to the envelope. The problem of large statistical noise in the single shot experiment and the averaging effect in many cycle acquisitions can both be eliminated if the CE phase of the driving laser can be locked for a sufficiently long interval of time such that it allows control over the CE phase of the driving field by some means such as by introducing dispersive material on the beam path or by changing the grating separation of the compressor. To make the scheme practicable it therefore requires co-ordination between two systems with one system stabilizing the CE phase while the other generates and records the high order harmonics. Schematic of the experimental setup to study attosecond two slits controlled by the carrier envelope is shown in Fig. 9.32.
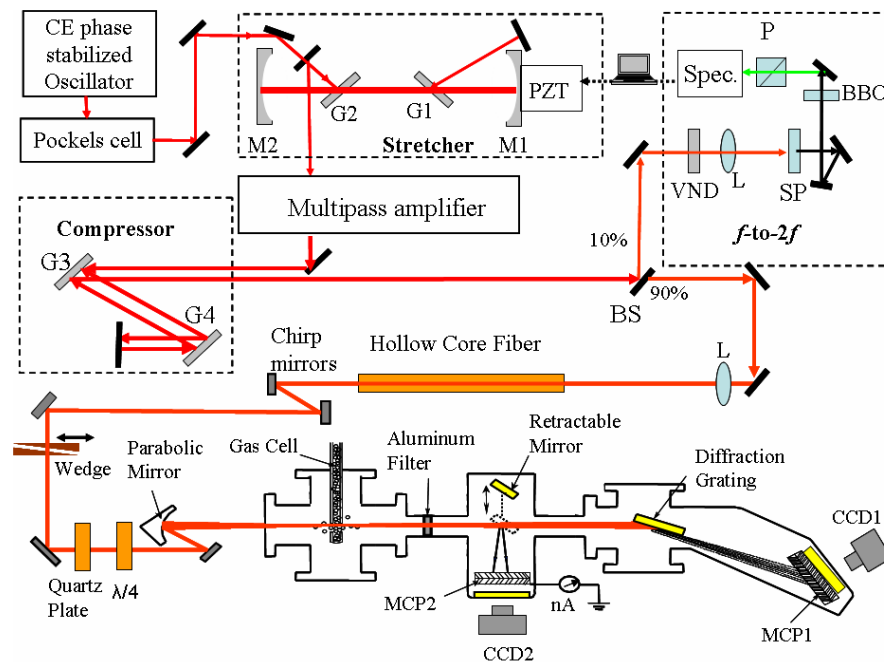
Fig 9.32 Schematics of CE phase stabilizing system of KLS and HHG spectrometer.

Our method of stabilizing the CE phase of the oscillator and amplifier has been explained in section 9.4. Since stabilized output from the oscillator subsequently seeds a multipass chirped-pulse Ti:Sapphire laser amplifier in order to intensify the pulse, it will accumulate phase noise inside the amplifier. Therefore, 10% of the compressed pulse after amplification is sent to the second f-to-2f interferometer with feedback loop to compensate these drifts. The beam undergoes nonlinear interaction with a thin sapphire plate which broadens the spectrum. A frequency doubling crystal (BBO in Fig.9.33) has been used to generate a frequency doubled spectrum. Due to a broad spectrum output from the sapphire plate, the *2f* portion of the fundamental spectrum and the *2f* portion of the frequency doubled spectrum spectrally overlap. In order to make frequency components co-linear, a polarizer (P in Fig 9.33) has been used. The final output then is the spectral interferences which are detected with a grating spectrograph (Spec. in Fig 9.33) and recorded with a computer that feeds back a signal to the piezoelectric transducer (PZT). One of the telescope mirrors (M1 in Fig.9.33) of the KLS has been mounted to the PZT driven stage. Feedback signal from the computer drives the PZT, thus controlling the effective distance between the two gratings [61-63]. This technique eliminates additional modulation that a second *f*-to-*2f* interferometer with its feedback looped to AOM would generate in the pump power, ensuring better precision for f_0 locking.

The CE phase stabilized intense output pulses of the KLS amplifier with 1kHz repetition rate have an energy of 2.5 mJ and duration 30 fs, which is too long to assume few cycle pulses (sub-ten femtosecond pulses). So about 1.2 mJ of pulses were passed through the hollow-fiber and then compressed by a chirp mirror which delivers 0.6 mJ with 7 fs duration. Two wedge plates (Wedge in Fig.9.33) mounted on a motorized stage after the hollow-fiber allow us to change the CE phase of the stabilized pulses. [Appendix for 58 μm≈2π] Introducing 58 μm thickness on the beam path gives rise to the change in CE phase of 2π radians, which corresponds to the 1.15 mm horizontal shift in the motorized stage. The quartz plate and the quarter wave plate generate the time-dependent ellipticity as described in section 8.5 which gates the XUV pulses generated by focusing the beam with an off-axis parabolic mirror onto the argon gas target. Argon gas is continuously supplied into the gas cell of inner diameter 1.44 mm which is drilled by the focused laser itself. A needle valve serves as a knob to fine tune the gas flow for achieving maximum phase matching pressure. The same aluminum filter, diffraction grating, and

116

microchannel plate were used to filter IR, to set the transmission band width, to diffract XUV, and to image the XUV spectrum respectively.
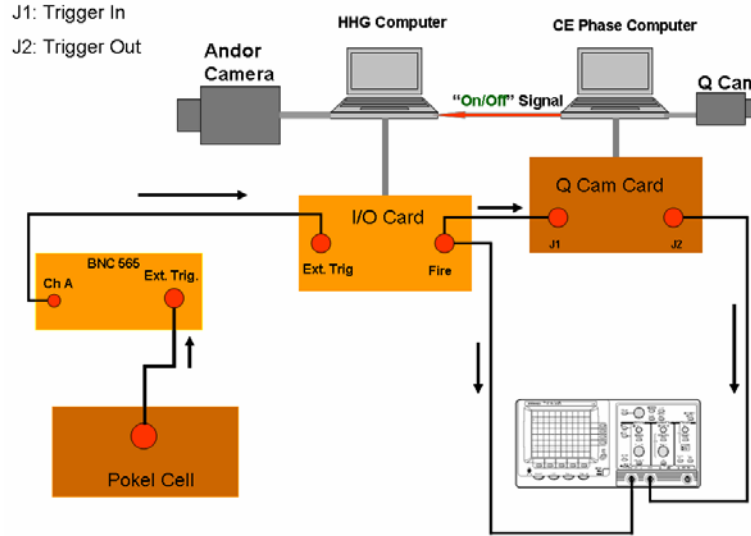
Fig 9.33 Schematics for synchronizing acquisition between Q-cam and Andor camera.
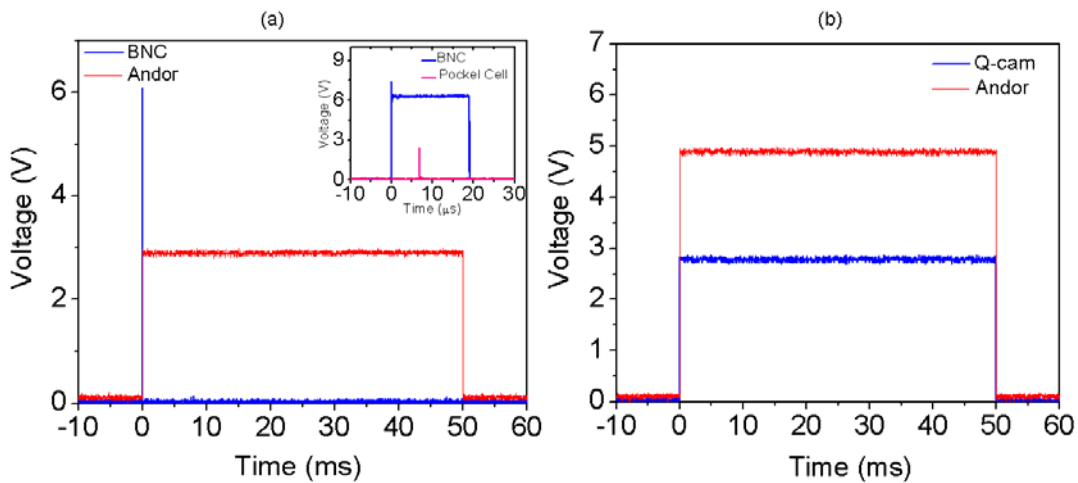
Fig 9.34 Synchronized signals between (a) BNC pulse and Andor CCD camera (b) Q-camera and Andor CCD camera seen on the oscilloscope ensure the synchronization of data acquisition within the precision of 100 μs. Inset in (a) shows the synchronization between triggering Pockels cell signal and BNC pulse.

Slight modification in the data acquisition system has been made to study the effect of the CE phase on the polarization gated multi-shot XUV supercontinuum. First, synchronization between the measurement of relative CE phase from the *f*-to-*2f* interferometer and acquisition of the

corresponding image of the XUV spectrum were necessary in order to compare the acquired data with the corresponding value of the relative CE phase measured from the *f*-to-*2f* interferometer. Since CCD cameras were used to capture the HHG spectrum and *f*-to-*2f* interferrogram, the exposure time of both the cameras were set to the same value (50ms) and synchronized. This allowed us to integrate the spectrum over several laser shots for each CE phase. Schematics of the setup for the purpose of studying the effect on the multishot XUV spectrum are illustrated in Fig. 9.33. The BNC 565 pulse generator was externally triggered by a Pokels Cell which generates 1000 pulses per minute in synchronization with the laser pulses. One of the output channels(Ch A in Fig. 9.34) of the BNC sends those pulses to trigger the Andor CCD camera. The Andor camera then sends the trigger signal to the Q Cam to startacquiring CE phase data. Control over both the CCD cameras was done via the LabVIEW program. As the LabVIEW programs of both the computers (HHG computer and CE phase computers in Fig. 9.33) were turned on, the HHG computer turns on the Andor CCD camera as soon as it receives the start signal from the CE phase computer. The Andor camera then triggers the Q camera and both the cameras, then start recording data simultaneously unless it completes the acquisition period set on the LabVIEW routine of the CE phase computer. Subsequently, after the HHG LabView routine is stopped by the stop signal of CE phase computer, acquisition from the Andor Camera also stops. Data acquisition from the Andor starts earlier and stops a little later since the Andor has to trigger the Q-camera to start, and the HHG LabView should be stopped by the stop signal of the CE phase LabView. We therefore should not expect a perfect synchronization of the data acquisition. However, exposure time of the both the cameras (Andor camera and Q-camera both set to 50 ms during the experiment) which can be monitored on the oscilloscope (Fig.9.34 (b)) shows our method of synchronization lies within the precision of 100 μs. As this value is negligibly smaller than the time between the two laser pulses, it is still reasonably well to compare acquired HHG data and acquired CE phase data from the Andor camera and the Q-camera respectively. In order to confirm the effect observed on the XUV spectrum purely due to change in the CE phase of the driving field, other influences that could cause similar effects to appear as the effect due to the CE phase should be isolated. For example, a change in intensity of the laser can also produce a similar effect in the XUV spectrum as the change in CE phase does. So, for the effect observed on the XUV spectrum, it should be proved that the data were recorded when the intensity of the laser was stable. This can be done by recording beam pointing stability

and the power fluctuation simultaneously while the XUV data and CE phase data are being acquired. The pointing stability of the input to the fiber was monitored in the lab by capturing a thin slice of the fiber output with the CCD coupled to the LabView program. This allows us to scan the horizontal and vertical shift of the fiber mode. In the meantime a LabView routine which was developed to monitor power fluctuation of a small portion of the beam (~10%) after the compressor provides the status of the laser power stability before it enters the fiber. Hence, only the data which were not affected by those two parameters has been considered worthy for studying the effect due to the CE phase of the driving laser field.

9.8 Results and discussion

In Fig.9.35 we show the fiber mode, f-to-2f interferrogram, XUV spectrum, and the laser power before it enters the fiber observed in the LabView routine. Those data were recorded in order to test our precision of synchronization in the data acquisitions. It was tested by blocking the beam twice, first just after it begins taking data and second just before it stops taking data. Two thin lines indicating missing data in the figure were observed at almost the same time in all intensity graphs. This ensures all the acquired data (fiber mode, *f*-to-*2f* interferometer, and XUV spectrum and laser power) were synchronized. The discrete straight vertical and well resolved interference patterns observed in the *f*-to-*2f* intensity plot indicate that the CE phase of the amplifier
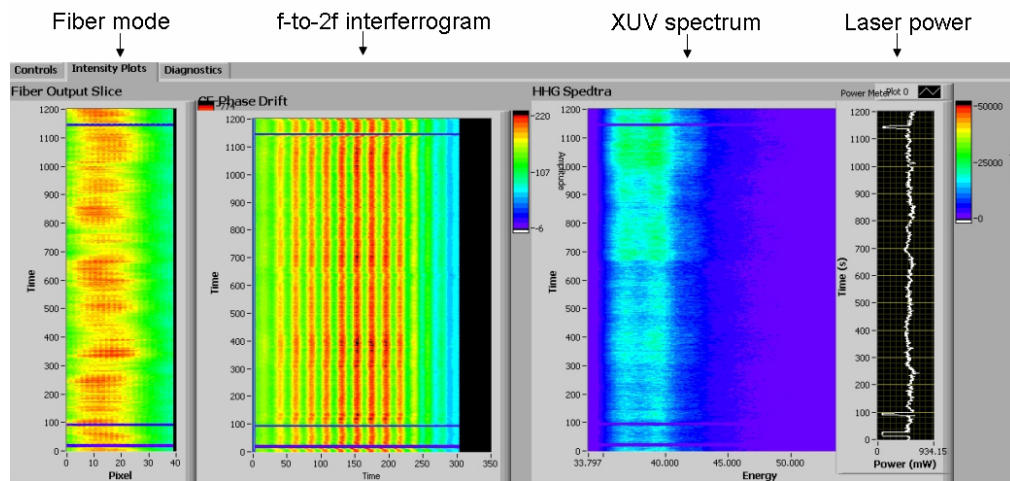
Fig 9.35 Evidence for synchronized acquisition of Fiber mode, f-to-2f, XUV spectrum and laser power.

and the oscillator were well locked. Randomly shifted image of fiber mode with alternatively light and dark yellow color shows that mode pointing is not stable and power fluctuation is high.

119

Two sharp decreases in power when the laser was blocked can be observed in the power meter data. Laser power before it enters the fiber does not seem to be unstable. It can therefore be concluded that intensity fluctuation in the fiber mode output was caused by the pointing instability.
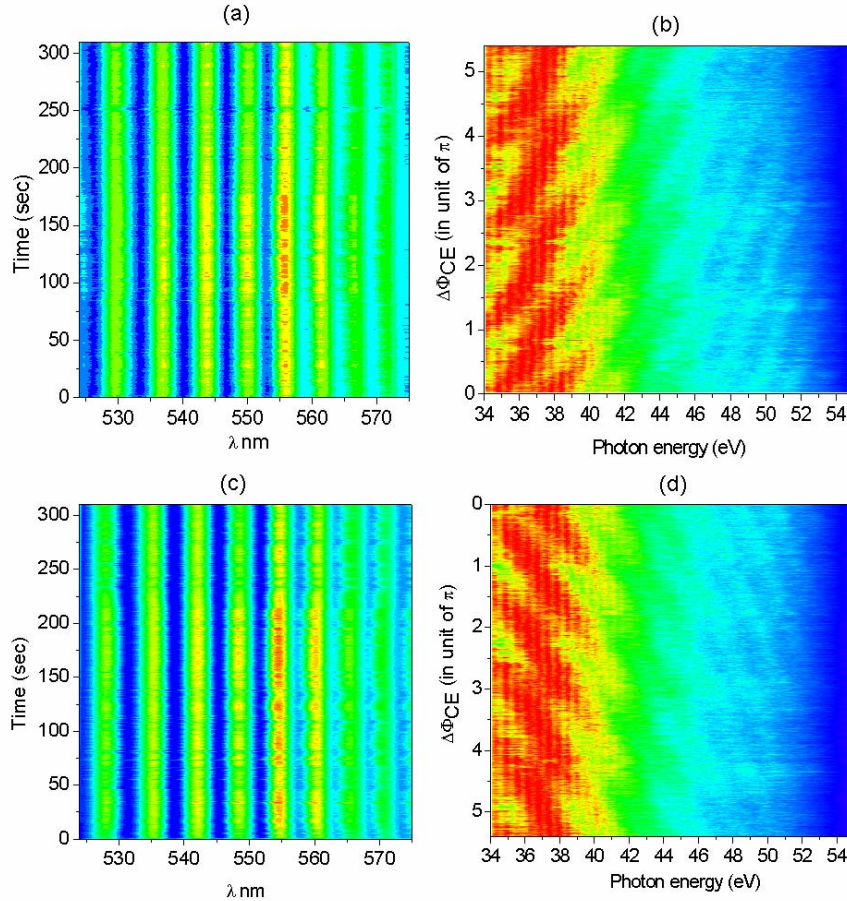
Fig 9.36 Shift in XUV spectrum as a function of the change in CE phase. Well resolved vertical interference pattern on the left is the f-to-2f interferrogram which provides evidence for CE phase of amplifier and oscillator locked. Vertical strips on the left (Fig 9.37 (a) and (c)) show that the CE phase of the amplifier and the oscillator were locked.

Shown in Fig. 9.37 (b) and (d) are the measured polarization gated high harmonic spectrum as a function of the change in CE phase of the driving field. Time dependent ellipticity was generated by using a 0.33 mm quartz plate in the polarization gating setup described in section 8.5. The pulse duration of the compressed pulse from the hollow fiber was measured to be 7 fs with output power after the chirp mirrors (Femto Laser: 9 bounces total) 0.5W. So the gate width (narrow region with negligibly small ellipticity) defined by $T_G \approx 0.3 * \tau^2 / T_d$ is 1.4 fs.

This is the temporal window where harmonic generation can take place. As the window is greater than a half optical cycle (1.3 fs), emission of two attosecond pulses within that interval generates interference fringes of the XUV spectrum in the frequency domain. A pair of wedges
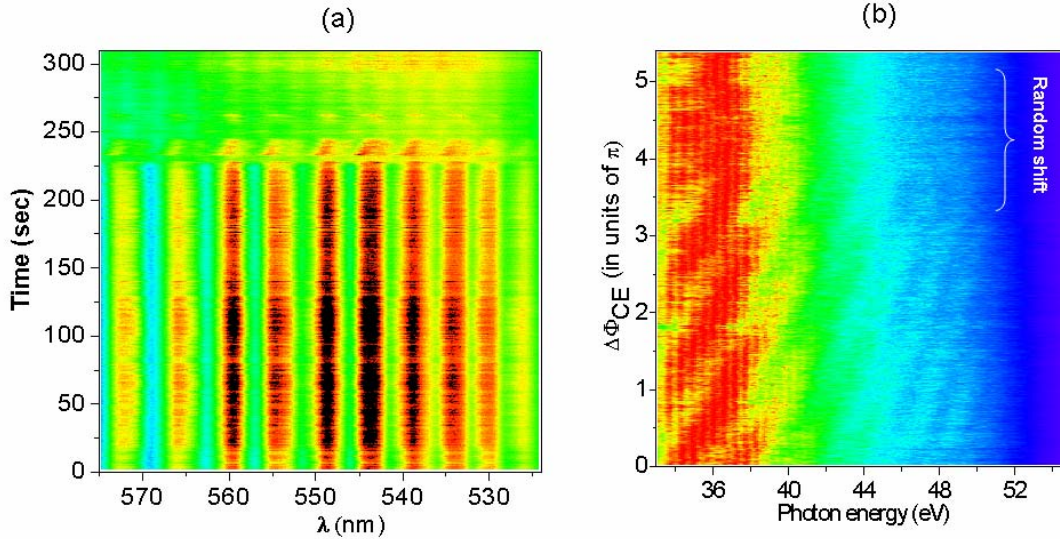
Fig 9.37 (a) f-to-2f interferrogram (b) XUV spectrum when CE phase was locked and un locked.

mounted on a motorized stage introduces a thickness of fused silica on the beam path at the rate of 0.5μm/sec giving 2π changes in the CE phase of the driving field in 115 second. The observed shift in the XUV spectrum due to the change in CE phase therefore provides the evidence for its sensitivity to the carrier shift of the driving laser pulse with respect to the envelope. When a few cycle optical pulses were used to generate the time dependent ellipticity from the polarization gating, only up to two emission processes contribute to the generation due to re-collision of either two or one electron return within the interval defined by the polarization gate window. Since, intensities of the pulse within the gate (Fig.8.20) are different; an electron released from the atom by higher intensity would follow a longer path than that released from the atom by the lower intensity. So the emissions by the two consecutive returning electrons return have two different phases Φ_1 and Φ_2 and phase difference $\Delta\Phi$. The interference of the two emissions due to the two consecutive returns is determined by $\Delta\Phi = \Phi_1 - \Phi_2$, which is proportional to $Cos\Delta\Phi$ through the relation of interference term $I_{12} = 2\sqrt{I_1 I_2} Cos\Delta\Phi$ [64]. As the intensity modulation of the spectrum is proportional to $Cos\Delta\Phi$, the harmonic spectrum is determined by $\Delta\Phi = \Phi_1 - \Phi_2$. However, $\Delta\Phi$ increases almost linearly with frequency, giving

$\Delta\Phi = a\omega$ [8]. Separation of the harmonic peak is therefore related by $\Delta\omega = 2\pi/a$, where a is the slope of the line defined by $\Delta\Phi = a\omega$ and depends on the cutoff harmonic q_c of the returning electron. Since the change in CE phase of the pulse changes the intensity of the driving field, it also changes the trajectory of the returning electrons, thereby resulting in the change in $\Delta\Phi$. It therefore turns out that slope a and therefore $\Delta\omega$ are functions of the intensity of the driving pulse, which is in turn a function of the CE phase. Hence, for a different CE phase, the $\Delta\Phi$ curve is different, which result, in the shift in the harmonic spectrum as a function of the CE phase of the driving field as observed in Fig.9.36 (b) and (d). It is also straight forward to see the quadratic relation in the phases Φ_1 and Φ_2 with the harmonic order q emitted by the interferences of consecutive re-collisions. In the case of few-optical-cycle pulses input for the polarization gating, only at most two emission processes contribute to the generation process in the cutoff region when the short quantum path is considered. Nevertheless, both returning electrons emitted by two different intensities within the gate width have approximately the same return time equal to half the optical period $T/2$. This leads to the phase $\Phi = \omega\tau = q\,\omega_0 * [q/q_c] * T/2 = [\omega_0 T/2q_c] * q^2$, where, q_c, ω_0 and ω are the cutoff harmonics, fundamental frequency and the frequency of the q th harmonic. For the two electrons returning via two different trajectories, q_c (proportional to the intensity of the driving electric field within the gate) is different which leads to two parabolic curves in the plot of phase Φ as a function of harmonics order q. So the same harmonic order q generated by those two returning electrons have phase difference $\Delta\Phi$, leading to the interference due to the cosine factor stated earlier. Further evidence for its sensitivity to the CE phase of the driving field has been depicted in Fig.9.37 (b). A shift in HHG spectrum was observed until the CE phase of the amplifier and oscillator was locked, and the CE phase of the driving laser was changed by introducing fused silica plates 0.5 μm/sec on the beam path. The shift was no longer observed as the CE phase of the amplifier and oscillator were unlocked. The random shift in the CE phase of the driving laser causes the HHG spectrum to shift in the random direction, giving rise to the averaging effect. This effect is pictorially observed as a washed-out continuum in the intensity map of the XUV spectrum. What is most interesting is that high order harmonics are even sensitive enough to detect slow drift in the CE phase of the driving field. Contrary to our expectation, when the CE phase of the amplifier and oscillator were locked and fused silica were no longer added, the shift

in the high harmonic spectrum was still obvious in Fig. 9.38(b). This is an obvious evidence that XUV spectrum serves as a tool to judge how perfectly the system can lock CE phase of the laser. For this reason, we focused our effort to measure the CE phase of the few cycle pulses as precisely as possible by investigating experimental conditions that would further enhance sensitivity of polarization gated XUV to the change in CE phase of the laser..
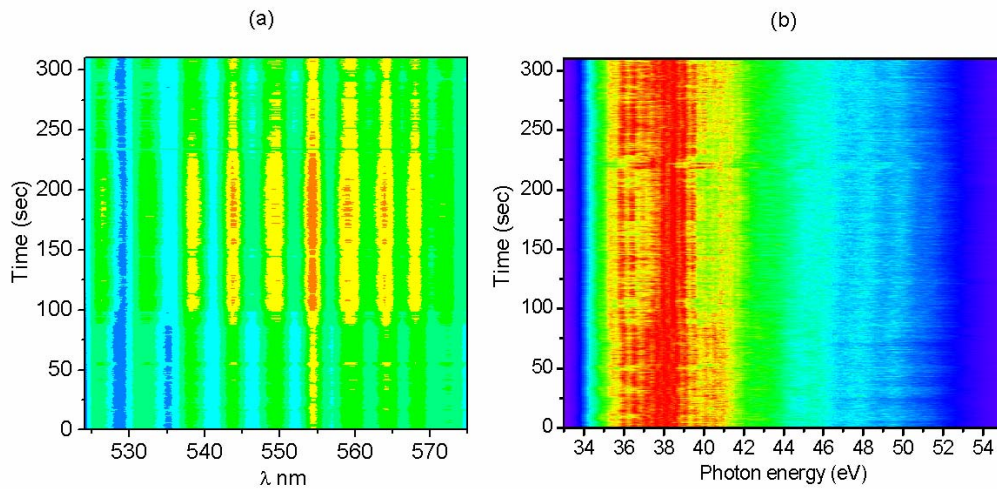
Fig 9.38 (a) CE phase locked *f*-to-*2f* interferrogram (b) Synchronized acquisition of XUV spectrum when thickness of the fused silica was stopped changing.
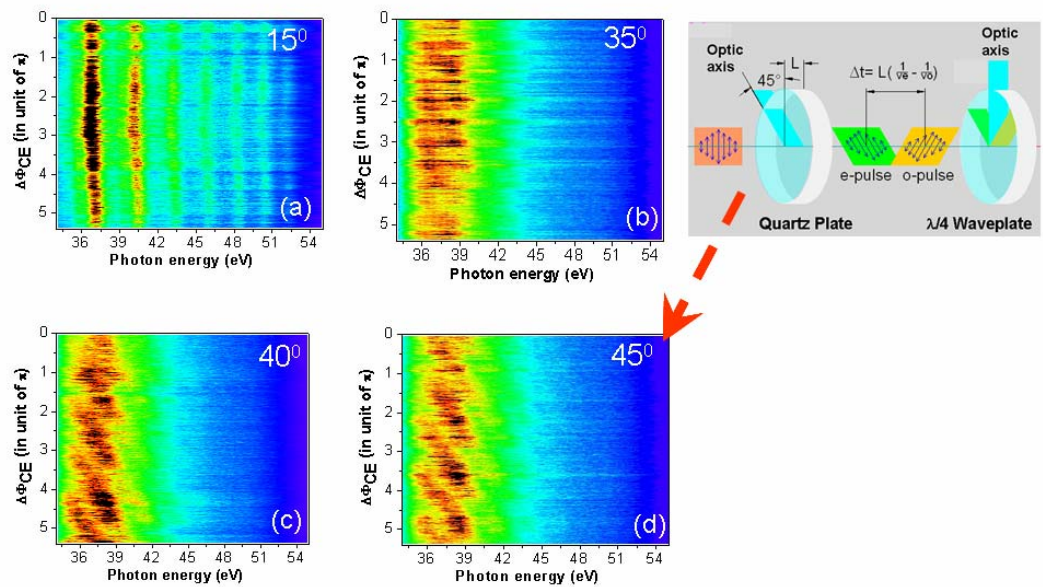
Fig 9.39 Scanned XUV spectrum when optics axis of quartz plate is rotated (a) 15^0 (b) 35^0 (c) 40^0 and (d) 45^0.

Rotation of the optics axis of the quartz plate by 15^0, 30^0, 35^0 and 45^0 to the optics axis of the quartz plate as shown in Fig.9.39 (a),(b),(c) and (d) respectively shows that the effect of the CE phase on the XUV spectrum was the strongest when polarization of the electric field of the laser makes an angle 45^0 to the optics axis of the quartz plate. When the optics axis is parallel to the direction of the electric field of the driving laser, the XUV spectrum seems insensitive to the change in the CE phase of the field. This is not surprising because, in this case, the harmonics are not polarization gated and the pulse is linear and long. As the optics axis is rotated, ellipticity of the pulse increases, and time-dependent ellipticity begins to gate the train of attosecond pulses. As the rotation angle was increased, the effect of the CE phase on the XUV became more distinct. The effect appeared most prominent (Fig. 9.39 (d)) when the rotation of the optics axis reached a 45^0 angle. The observed effect is quite consistent with the theory explained in section 8.5 at which the gate width becomes minimum and the two delayed pulses become symmetrically circular on either side of the narrow quasi-linear region.
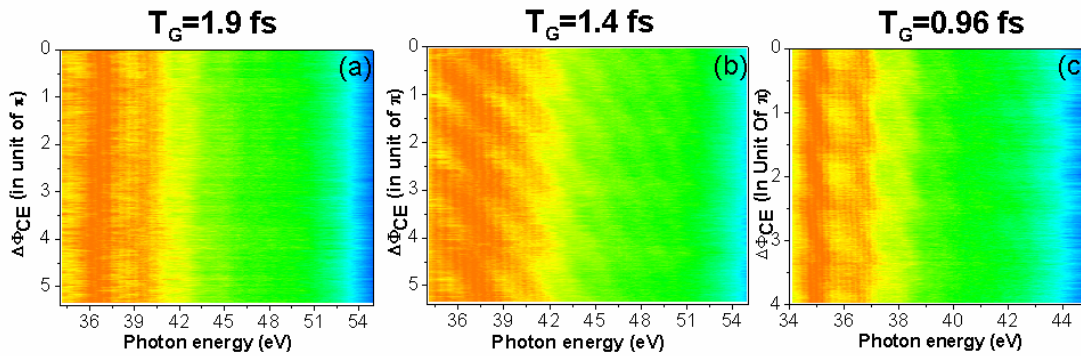
Fig 9.40 Effect of polarization gate width T_G on XUV, when quartz plates of thickness (a) 0.25 mm (b) 0.33 and (c) 0.5 mm were used. Measured laser pulse duration was 7 fs with 0.5 W output.

Our observation shows that the effect of the CE phase on the XUV spectrum increased as the gate width was made narrow. Although, the gate width can be made narrow either by reducing pulse duration or by increasing the thickness of the quartz plate, the former is preferable because the width is directly proportional to the square of it and eliminates the risk of depletion of the ground state population of the atom, as it might if the large thickness of the quartz plate were used. Nevertheless, routinely available pulse durations in KLS, which is typically ~7fs, prevent us from using a pulse shorter than that. Hence, by setting the pulse duration as short as possible, we measured the change in the strength of the effect on the XUV spectrum due to change in the gate width by using a quartz plate of different thickness. Shown in Fig. 9.40 (a), (b) and (c) are

the XUV traces recorded by using quartz plates of thicknesses 0.25 mm, 0.33 mm and 0.5 mm, which synthesize temporal polarization gate windows of 1.9 fs, 1.46 fs and 0.96 fs respectively. What is interesting in that spectrum is that the effect of the CE phase is extremely weak when the gate width was 1.9 fs. This is the effect that we first began to observe during the course of reducing the gate width. We never observed the effect of CE phase when the gate width was made wider than one optical cycle (2.6 fs). Quite interestingly, as the polarization gate width was made narrower, the strength of the influence of the CE phase change became stronger and stronger. Repeatedly, observed XUV traces with 0.33 mm quartz plate, which corresponds to 1.46 fs gate width, show a shift of the XUV spectrum with the absence of any traces of continuum (Fig. 9.40(b)). Since the gate width is wider than half the optical cycle, interference of emission due to two re-collisions dominates in this range, which corresponds to two attosecond pulses in the time domain (Fig. 8.19 (a)). When the gate width reached 0.96 fs, which is less than half an optical cycle, the XUV spectrum was modified with the periodical appearance of the continuum at the spacing of π radian phase as shown in Fig. 9.40 (c). Evolution of harmonics into the continuum at this range is the signature of single and double attosecond generation in which the continuum is the remarkable manifestation of a single attosecond pulse and the harmonic that of double attosecond pulses.

As for a further test to confirm the attosecond burst in the polarization gating, we scanned the CE phase over 5π and integrated the spectrum over 50 laser shots for each value of the CE phase, but this time without introducing the thickness of the fused silica plates. What we did instead was a novel technique to change the CE phase of the amplifier by changing the effective distance of the grating in the stretcher. The advantage of using this method over the method of introducing the fused silica on the beam path is that it never introduces material dispersion to the few cycle pulse as it does when wedge plates are used. Besides, it also eliminates the problem of beam pointing instability at the interaction region caused by the addition of material thickness on the beam path. This is very important because pointing instability can fluctuate intensity in the interaction region, which in turn can add a kind of effect similar to that which a change in CE phase does in the XUV spectrum.

Fig.9.41 (a) and (c) shows the interferrogram taken from the *f*-to-*2f* interferometer when the effective grating separation was varied to change the CE phase from 0 to π and back to 0 in (a) and 0-π-2π and back to 0 in (b). Corresponding XUV traces due to those changes are shown
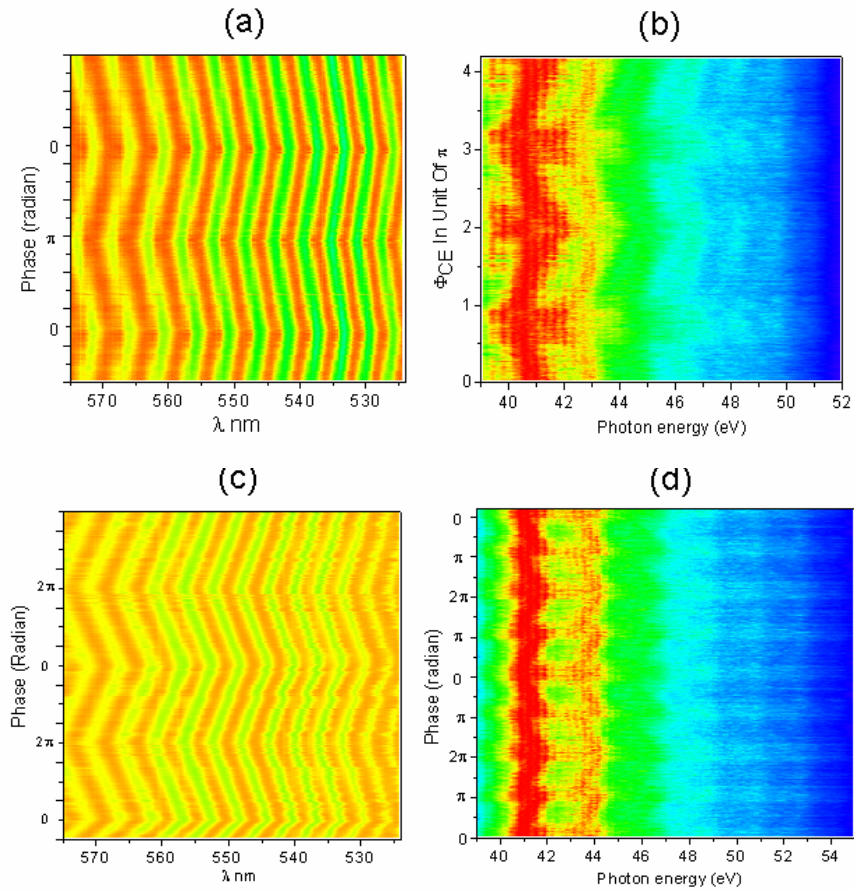
Fig 9.41 *f*-to-*2f* interferrogram on the left and corresponding effect on XUV spectrum on the right when effective grating separation was varied to change CE phase by (a) 0-π-0 (b) 0-π-2 π-π-0.
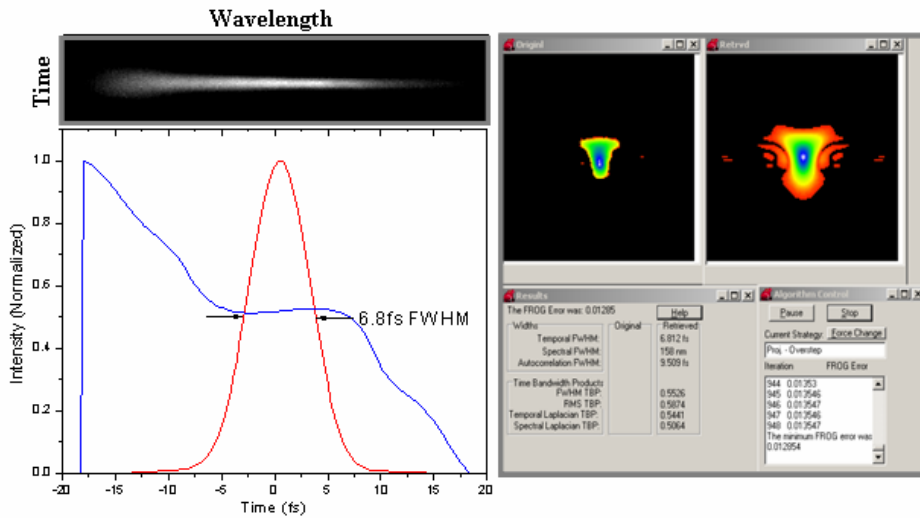
Fig 9.42 FROG traces of ~7 fs pulse from the hollow-fiber measured just after the observations depicted in Fig.9.41.

in Fig. 9.41 (b) and (d) respectively. In either case, continuum spectra are separated by π radians and the direction that the high harmonic spectrum shifted was inconsistent with that observed when wedge plates were used. Both the results of the measurement give better agreement in the periodicity with which the continuum appeared in the plot when the quartz plate of thickness 0.5 mm was used, which corresponds to the gate width 0.96 fs. Fig. 9.42 shows the FROG trace
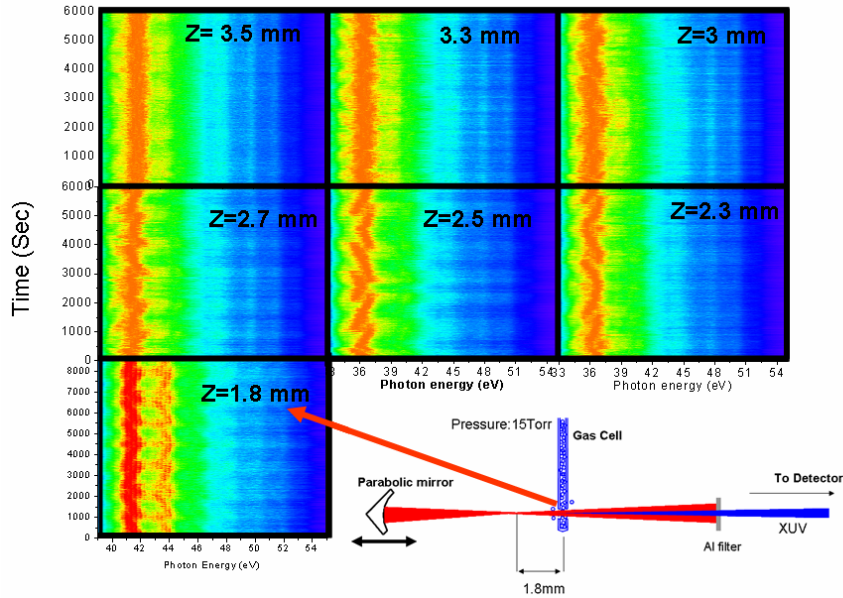
Fig 9.43 Effect of relative position of the target from the focus in the measurement of CE phase effect on polarization gated XUV super-continuum.

observed immediately after those observations which measured pulse duration from the hollow fiber ~7 fs. In both cases the effect of the CE phase appeared comparatively strong when the polarization gate width was made smaller.Other sets of our investigation show that sensitivity to the change in CE phases also depends on the relative position of the target from the focus. Our measured data shows that the effect of the CE phase appeared clearer as the target was moved closer to the focus, which is shown in Fig.9.44. Harmonic spectra with alternative continuum stripes were observed when the target approached 1.8 mm away from the focus. Although, we could not measure the XUV spectrum by placing the target at a different location before the focus due to technical problems in the laser that arose during the time of measurement , the effect observed after the focus is due to the phase matching of the harmonics by the cancellation of the phase mismatch due to plasma dispersion and the Guoy phase shift by the variation of the

harmonics phase due to a decrease of the laser intensity and the electron density in the laser propagation direction. Therefore, by optimizing four different parameters (gas pressure, polarization gate width, rotation of the quartz plate and the focal position) sensitivity of change
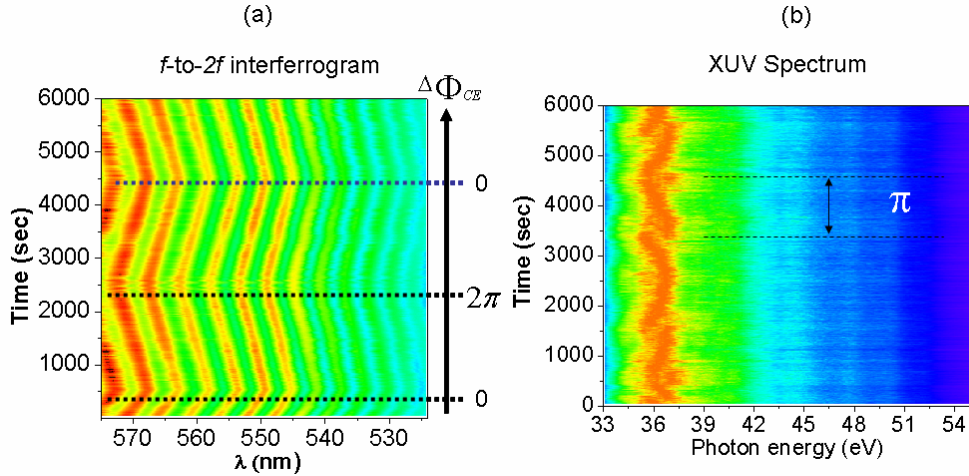
Fig 9.44 Measured CE phase effect on XUV by changing relative CE phase by known amount.

in CE phase to the XUV can be enhanced,which is important in order to design a good XUV phase meter. One neat example which might lead to a powerful phase meter has been depicted in Fig. 9.44. In this case we varied the CE phase by the known values by changing the effective distance between the grating pair of the stretcher and obtained the XUV traces under the best optimization of the critical parameters. The XUV spectrum appeared with the continuum with a separation of π radians. As the continuum is the result of the laser field with CE phase $\pi/2$, this method therefore can be used to measure the CE phase of the laser system.

CHAPTER 10 - Conclusions

This work has demonstrated the use of a polarization gating technique to produce a super-continuum extending up to 60 eV photon energy. This has now been possible due to the availability of a high-power, short-pulse optical pump laser and excellent pulse compression technique with a hollow-fiber routinely delivering 6-7fs pulse duration at the output power of 600mW. In order to demonstrate the shot-to-shot effect of CE phase change in the few cycle pulse on single shot XUV supercontinuum we have designed a novel XUV spectrometer. We used an aluminum filter both for blocking infra-red pulses and for shielding the flow of gas from the interaction chamber to the detection chamber. This is necessary because our detector consists of a microchannel plate which can be operated safely at a pressure 10^{-6} Torr or less. Another advantage of using an aluminum filter as a shield is that it minimizes the absorption of photons by gas in the detector chamber. The aluminum filter was prevented from rupturing by using a gas cell which is drilled by the laser focus itself. So a gas cell with hole diameter as big as the focal spot size serves to provide a differential pumping system as well as region for laser-matter interaction. As the space surrounding the gas cell has never been observed to reach more than 200 mT when pressure inside the gas cell was raised to 200 T, the risk of breaking the aluminum filter even at such a high pressure is highly unlikely. So the design can be used for a wide range of pressure to study the high harmonics efficiency as a function of pressure. In fact this is one of the reasons that a single shot measurement of the effect of CE phase on XUV has become possible with this design. Maximum phase matching pressure was measured to be 55 Torr. This was identified by locating pressure threshold beyond which quadratic variation in intensity with pressure ceases to show up. This limit to the maximum usable pressure can be attributable to the mismatch between the phase velocity of the laser pulse in the ionizing gas and the phase velocity of the harmonics. We believe that at a pressure of 55 torr the phase matching was achieved by the cancellation of the phase mismatch due to the plasma dispersion and the Guoy phase shift by the variation of the harmonics phase due to a decrease of the laser intensity and the electron density in the laser propagation direction. We also measured the maximum number of photons

per laser shot at this pressure to be ~ 10^4, which was enough to do the single-shot experiment. Measurement of the number of photons was made possible by the use of a second microchannel plate. The same microchannel plate was also used to measure the divergence angle of the XUV, which was 3.5 mrad. This value became very important to compare with the acceptance angle of the grating in order to take feedback information for the necessary adjustment to enhance throughput of the spectrometer.

Improving the number of the photon count is not a sufficient condition to do the single - shot experiment. In order to observe the effect of CE phase on the XUV spectrum by polarization gating, the polarization gate width should also be made less than one optical cycle. There are two ways to control the gate width. One is by reducing the pulse duration, and the other by increasing the delay between the two circularly polarized pulses. However, the former is limited by the limit of the currently available system to generate the shortest pulse. In the latter case, the gate width cannot be reduced by the large increase in delay as it reduces the intensity of the quasi-linear portion. So the leading edge of the pulse in that case can deplete the ground state electrons reducing the efficiency of the harmonic generation. However, we have been able to make the gate width as short as 0.96 fs by introducing a 0.5 mm quartz plate for which the gate width was sufficiently narrow and intensity was moderately high, to observe continuum for some shot and discrete harmonics for the other shots. It can be interpreted that the continuum is the result of emission due to single electron ion re-collision with the parent ion, and the harmonics is the result of interference of the emission due to double electron and ion re-collision. The double electrons in the polarization gating are released when the CE phase becomes zero. At $\pi/2$ phase, only single electron emission is possible, thereby generating super-continuum harmonics. Therefore our study can lead to the design of a phase meter for those whose laser does not have a CE phase locking system.

As only limited numbers of photons are available in the single-shot experiment, the result obtained has large statistical noise. If numbers of shots are increased to enhance the signal-to-noise ratio, the result would give nothing more than an averaging effect due to randomly varying intensity caused by random change in the CE phase. So to increase the integration time of signal acquisition, the CE phase of the laser system should be locked. Since our system can routinely lock CE phase over 10 minutes, the XUV spectrum can be integrated over several laser shots for each CE phase. We observed a shift in the high harmonic spectrum as a result of change in the

CE phase when the gate width approached less than one optical cycle. We believe that the shift in the position of the spectral peak was caused by the change of the path of the returning electrons as a result of the change in the CE phase. We also demonstrated polarization gated high harmonics with periodic continuum separated by π radians and shifted spectral peak when the gate width was made less than half the optical cycle.

Additional evidence for the effect of the CE phase on the polarization gated XUV spectrum was provided by the appearance of a similar effect when the effective separation of the grating was changed instead of using wedge plates to change the CE phase. The advantage of using this technique over using a wedge is that it does not introduce material dispersion. Hence, this method isolates other effects on XUV similar to the effect of the CE phase. The effect of the CE phase was found to be prominent at the narrow gate width formed by the rotation of the optics axis of the quartz plate at an angle 45^0. A new technique developed in KLS allowed us to set the relative CE phase of the driving pulse to several different known values. In association with this technique, study of the CE phase effect on XUV and its measurement of absolute CE phase have become possible. This study therefore leads to the design of an XUV phase meter capable of measuring absolute CE phase, which would greatly benefit other CE phase dependent laser experiments using a laser whose CE phase is unlocked.

Bibliography

[1] Maiman, T. H**.**,Stimulated optical radiation in ruby. *Nature* 1960. **187:** 493-494.

[2] Herman, J. W. and Elsayedali, H. E**.**, time-resolved study of surface disordering of PB(110). *Phys. Rev. Lett.* 1992. **68:** 2952-2955.

[3] Lindenberg, A. M., Kang, I., Johnson, S. L., Missalla, T., Heimann, P. A., Chang, Z., Larsson, J., Bucksbaum, P. H., Kapteyn, H. C., Padmore, H. A., *et al*, Time-resolved X-ray diffraction from coherent phonons during a laser-induced phase transition. *Phys. Rev. Lett.* 2000. **84:** 111-114.

[4] Gai, F., Hasson, K. C., McDonald, J. C. and Anfinrud, P. A**.**, Chemical dynamics in proteins: The photoisomerization of retinal in bacteriorhodopsin. *Science* 1998. **279:** 1886-1891.

[5] Chang, Z., Rundquist, A., Zhou, J., Murnane, M. M., Kapteyn, H. C., Liu, X., Shan, B., Liu, J., Niu, L., Gong, M. and Zhang**, X.**, Demonstration of a sub-picosecond x-ray streak camera. *Appl. Phys. Lett.* 1996. **69:** 133-135.

[6] Liu, J. Y., Wang, J., Shan, B., Wang, C. and Chang, Z. H**.**, An accumulative x-ray streak camera with sub-600-fs temporal resolution and 50-fs timing jitter. *Appl. Phys. Lett.* 2003. **82:** 3553-3555.

[7] Corkum, P. B**.**,Plasma perspective on strong-field multiphoton ionization. *Phys. Rev. Lett.* 1993. **71:** 1994-1997.

[8] Baltuska, A., Uiberacker, M., Goulielmakis, E., Kienberger, R., Yakovlev, V. S., Udem, T., Hansch, T. W. and Krausz, F**.**, Phase-controlled amplification of few-cycle laser pulses. *Ieee Journal of Selected Topics in Quantum Electronics* 2003. **9:** 972-989.

[9] Paulus, G. G., Lindner, F., Walther, H., Baltuska, A., Goulielmakis, E., Lezius, M. and Krausz, F**.**, Measurement of the phase of few-cycle laser pulses. *Phys. Rev. Lett.* 2003. **91:** 253004.

[10] Baltuska, A., Udem, T., Uiberacker, M., Hentschel, M., Goulielmakis, E., Gohle, C., Holzwarth, R., Yakoviev, V. S., Scrinzi, A., Hansch, T. W. and Krausz, F**.**, Attosecond control of electronic processes by intense light fields. *Nature* 2003. **421:** 611-615.

[11] Budil, K. S., Salieres, P., Lhuillier, A., Ditmire, T. and Perry, M. D**.**, Influence of ellipticity on harmonic-generation. *Physical Review a* 1993. **48:** R3437-R3440.

[12] Corkum, P. B., Burnett, N. H. and Ivanov, M. Y**.**,Subfemtosecon pulses. *Opt. Lett.* 1994. **19:** 1870-1872.

[13] Sansone, G., Benedetti, E., Calegari, F., Vozzi, C., Avaldi, L., Flammini, R., Poletto, L., Villoresi, P., Altucci, C., Velotta, R., *et al*, Isolated single-cycle attosecond pulses. *Science* 2006. **314:** 443-446.

[14] Chang, Z. H**.**, Single attosecond pulse and xuv supercontinuum in the high-order harmonic plateau. *Physical Review a* 2004. **70:** 043802.

[15] Chang, Z. H**.**, Chirp of the single attosecond pulse generated by a polarization gating. *Physical Review a* 2005. **71:** 023813.

[16] Shan, B., Ghimire, S. and Chang, Z**.**, Generation of the attosecond extreme ultraviolet supercontinuum by a polarization. *Journal of Modern Optics* 2005. **52:** 277-283.

[17] Hecht E**.**, *Optics.* Addison Wesley, 2001.

[18] Qian, B. L. and Elsayed-Ali, H. E., Electron pulse broadening due to space charge effects in a photoelectron gun for electron diffraction and streak camera systems. *J. Appl. Phys.* 2002. **91:** 462-468.

[19] Bradley, D. J., Roddie, A. G., Sibbett, W., Key, M. H., Lamb, M. J., Lewis, C. L. S. and Sachsenmaier, P**.**,Picosecond x-ray chronoscopy. *Opt. Commun.* 1975. **15:** 231-236.

[20] Chang, Z., Rundquist, A., Wang, H., Murnane, M. M., Kapteyn, H. C., Liu, X., Shan, B., Liu, J., Niu, L., Gong, M., *et a*l, Demonstration of a 0.54-ps x-ray streak camera. 1997. **- 2869:** - 976.

[21] Henke, B. L., Liesegang, J. and Smith, S. D.,Soft-x-ray-induced secondary-electron emission from semiconductors and insulators models and measurements. *Physical Review B* 1979. **19:** 3004-3021.

[22] Jiang, X., Berglund, C. N., Bell, A. E. and Mackie**, W. A.**, OS3: Photoemission from gold thin films for application in multiphotocathode arrays for electron beam lithography. 1998. **- 16:** - 3379.

[23] Maksimchuk, A., Kim, M., Workman, J., Korn, G., Squier, J., Du, D., Umstadter, D., Mourou, G. and Bouvier, M**.**, Signal averaging x-ray streak camera with picosecond jitter. *Rev. Sci. Instrum.* 1996. **67:** 697-699.

[24] Liu, J. Y., Wang, J., Shan, B., Wang, C. and Chang, Z. H., An accumulative x-ray streak camera with sub-600-fs temporal resolution and 50-fs timing jitter. *Appl. Phys. Lett.* 2003. **82:** 3553-3555.

[25] Jaanimagi, P. A., Breaking the 100-fs barrier with a streak camera. 2004. **- 5194:** - 182.

[26] Jiang, X., Berglund, C. N., Bell, A. E. and Mackie, W. A**.**, OS3: Photoemission from gold thin films for application in multiphotocathode arrays for electron beam lithography. 1998. - **16:** - 3379.

[27] Syms, R. R. A., Tate, T. J., Ahmad, M. M. and Taylor, S., Design of a microengineered electrostatic quadrupole lens. *IEEE Trans. Electron Devices* 1998. **45:** 2304-2311.

[28] Okayama, S. and Kawakatsu, H., Line-focusing by means of a quadrupole lens.*Journal of Physics E-Scientific Instruments* 1983. **16:** 166-170.

[29**]** Denison, D. R.,Operating parameters of a quadrupole in a grounded cylindrical housing.. *Journal of Vacuum Science & Technology* 1971. **8:** 266-&.

[30] Liu, J., Liu, C., MacPhee, A. G., Shan, B., Chang, Z. and Wang, J., New approach to jitter reduction of an x-ray streak camera in accumulation mode. 2003. - **4796:** - 188.

[31] Denison, D. R.,Operating parameters of a quadrupole in a grounded cylindrical housing. *Journal of Vacuum Science & Technology* 1971. **8:** 266-&.

[32] Shakya, M. M. and Chang, Z**.**, An accumulative x-ray streak camera with 280-fs resolution. 2004. - **5534:** - 131.

[33] Shakya, M. M. and Chang, Z. H**.**, Achieving 280 fs resolution with a streak camera by reducing the deflection dispersion. *Appl. Phys. Lett.* 2005. **87:** 041103.

[34] Lindenberg, A. M., Kang, I., Johnson, S. L., Missalla, T., Heimann, P. A., Chang, Z., Larsson, J., Bucksbaum, P. H., Kapteyn, H. C., Padmore, H. A., et al, Time-resolved X-ray diffraction from coherent phonons during a laser-induced phase transition. *Phys. Rev. Lett.* 2000. 84: 111-114.

[35] Wang, Y., Granados, E., Larotonda, M. A., Berrill, M., Luther, B. M., Patel, D., Menoni, C. S. and Rocca**,** J. J., High-brightness injection-seeded soft-x-ray-laser amplifier using a solid target. *Phys. Rev. Lett.* 2006. **97:** 123901.

[36] Nickles, P. V., Shlyaptsev, V. N., Kalachnikov, M., Schnurer, M., Will, I. and Sandner, W., Short pulse x-ray laser 32.6 nm based on transient gain in ne-like titanium. *Phys. Rev. Lett.* 1997. **78:** 2748-2751.

[37] Dunn, J., Osterheld, A. L., Shepherd, R., White, W. E., Shlyaptsev, V. N. and Stewart, R. E., Demonstration of x-ray amplification in transient gain nickel-like palladium scheme. *Phys. Rev. Lett.* 1998. **80:** 2825-2828.

[38] Yu V Afanas'ev and V N Shlyaptsev, Formation of a population inversion of transitions in ne-like ions in steady-state and transient plasmas. 1989. **19 (12):** .

[39] Rocca, J. J**.**, Table-top soft x-ray lasers. *Rev. Sci. Instrum.* 1999. **70:** 3799-3827.

[40] Rocca, J. J., Wang, Y., Larotonda, M. A., Luther, B. M., Berrill, M. and Alessi, D**.**, Saturated 13.2 nm high-repetition-rate laser in nickellike cadmium. *Opt. Lett.* 2005. **30:** 2581-2583.

[41] Luther, B. M., Wang, Y., Larotonda, M. A., Alessi, D., Berrill, M., Marconi, M. C., Rocca, J. J. and Shlyaptsev, V. N., Saturated high-repetition-rate 18.9-nm tabletop laser in nickellike molybdenum. *Opt. Lett.* 2005. 30: 165-167.

[42] Wang, Y., Larotonda, M. A., Luther, B. M., Alessi, D., Berrill, M., Shlyaptsev, V. N. and Rocca, J. J., Demonstration of high-repetition-rate tabletop soft-x-ray lasers with saturated output at wavelengths down to 13.9 nm and gain down to 10.9 nm. *Physical Review a* 2005. **72:** 053807.

[43] Flettner, A., Konig, J., Mason, M. B., Pfeifer, T., Weichmann, U., Duren, R. and Gerber, G**.**, Ellipticity dependence of atomic and molecular high harmonic generation. *European Physical Journal D* 2002. **21:** 115-119.

[44] Liang, Y., Augst, S., Ammosov, M. V., Lazarescu, S. and Chin, S. L., Experimental investigation of the ellipticity dependence of high-harmonic generation and ionization in argon in the multiphoton regime. *Journal of Physics B-Atomic Molecular and Optical Physics* 1995. **28:** 2757-2764.

[45] Hentschel, M., Kienberger, R., Spielmann, C., Reider, G. A., Milosevic, N., Brabec, T., Corkum**,** P., Heinzmann, U., Drescher, M. and Krausz, F**.**, Attosecond metrology. 2001. **414:** 513.

[46] Platonenko, V. T. and Strelkov, V. V., Single attosecond soft-x-ray pulse generated with a limited laser beam. *Journal of the Optical Society of America B-Optical Physics* 1999. **16:** 435-440.

[47] Paulus, G. G., Lindner, F., Walther, H., Baltuska, A., Goulielmakis, E., Lezius, M. and Krausz, F**.**, Measurement of the phase of few-cycle laser pulses. *Phys. Rev. Lett.* 2003. **91:** 253004.

[48] Harris, S. E**.**, Generation of vacuum ultraviolet and soft-X-ray radiation using high-order nonlinear optical polarizabilities. *Phys. Rev. Lett.* 1973. **31:** 341-344.

[49] Mcpherson, A., Gibson, G., Jara, H., Johann, U., Luk, T. S., Mcintyre, I. A., Boyer, K. and Rhodes, C. K**.**, Studies of multiphoton production of vacuum ultraviolet-radiation in the rare-gases. *Journal of the Optical Society of America B-Optical Physics* 1987. **4:** 595-601.

[50] Ferray M and A L'Huillier, X F Li, L A Lompre, G Mainfray and C Manus, Multiple-harmonic conversion of 1064 nm radiation in rare gases. 1988. **21:** L31-L35.

[51] Keldysh, L. V**.**, Ionization in field of a strong electromagnetic wave. *Soviet Physics Jetp-Ussr* 1965. **20:** 1307-&.

[52] Augst, S., Strickland, D., Meyerhofer, D. D., Chin, S. L. and Eberly, J. H.,Tunneling ionization of noble gases in a high-intensity laser field.. *Phys. Rev. Lett.* 1989. **63:** 2212-2215.

[53] Corkum, P. B**.**,Plasma perspective on strong-field –multiphoton ionization.. *Phys. Rev. Lett.* 1993. **71:** 1994-1997.

[54] Krause, J. L., Schafer, K. J. and Kulander, K. C., High-order harmonic-generation from atoms and ions in the high-intensity regime. *Phys. Rev. Lett.* 1992. **68:** 3535-3538.

[55] Becker, W., Long, S. and Mciver, J. K., Modeling harmonic-generation by a zero-range potential. *Physical Review a* 1994. **50:** 1540-1560.

[56] Antoine, P., LHuillier, A., Lewenstein, M., Salieres, P. and Carre, B., Theory of high-order harmonic generation by an elliptically polarized laser field. *Physical Review a* 1996. **53:** 1725-1745.

[57] Burnett, N. H., Kan, C. and Corkum, P. B**.**, Ellipticity and polarization effects in harmonic-generation in ionizing neon. *Physical Review a* 1995. **51:** R3418-R3421.

[58] Baltuska, A., Udem, T., Uiberacker, M., Hentschel, M., Goulielmakis, E., Gohle, C., Holzwarth, R., Yakovlev, V. S., Scrinzi, A., Hansch, T. W. and Krausz, F., Attosecond control of electronic processes by intense light fields (vol 421, pg 611, 2003). *Nature* 2003. **422:** 189-189.

[59] Nisoli M.and S.De Silvestri, and O. Svelto, Generation of high energy 10 fs pulses by a new pulse compressiontechnique.1996. **68:** 2793-2795.

[60] Rundquist, A**.**, Phase-matched generation of coherent, ultrafast x-rays using high harmonics. 1998.

[61] Chengquan Li and Eric Moon, and Zenghu Chang, Carrier-envelope phase shift caused by variation of grating separation. 2006. **31:** 3113-3115.

[62] Chengquan Li and Eric Moon, Hiroki Mashiko, Christopher M. Nakamura, Predrag Ranitovic, Chakra M. Maharjan, C. Lewis Cocke, Zenghu Chang, Gerhard G. Paulus, Precision control of carrier-envelope phase in grating based chirped pulse amplifiers. 2006. **14:** 11468-11476.

[63] Chang, Z. H**.**, Carrier-envelope phase shift caused by grating-based stretchers and compressors. *Appl. Opt.* 2006. **45:** 8350-8353.

[64] Nisoli M. and G. Sansone, S. Stagira, S. De Silvestri, C. Vozzi, M. Pascolini, L. Poletto, P. Villoresi, and G. Tondello, Effects of carrier-envelope phase differences of few-optical-cycle light pulses in single-shot high-order-harmonic spectra. 2003. **91:** 213905.

[65] M.V. Ammosov, N.B. Delone, and V.Krainov, Zh. Eksp. Teor.Fiz.91**,**2008 (1986) [Sov.Phys.JETP **64**,1191 (1986)].

[66] H. R. Telle, G. Steinmeyer, A. E. Dunlop, J. Stenger, D. H. Sutter, U. Keller, "Carrier-envelope offset phase control: A novel concept for absolute optical frequency measurement and ultrashort pulse generation," *Appl. Phys. B,* vol. **69**, pp. 327-332, 1999

[67] D. J. Jones et al. "Carrier-Envelope Phase Control of Femtosecond Mode-Locked Lasers and Direct Optical Frequency Synthesis" Science, Apr. 28, 2000, vol. **228**, pp. 635-639.

Appendix A - ADK ionization Calculation

```
c = 0.3; (*speed of light in μm/fs*)
λ = 0.8; (*Wavelenght in μm*)
T = λ/c; (*Time period in fs*)
ω = 2 * Pi * 1/T; (*Angular frequency*)
τp = 25; (*Pulse width FWHM in fs*)
I01 = 4 * 10^14; (*Intensity in W/cm^2*)
Ip = 15.76; (*Ionization Potential of Ar in eV*)
z = 1; (*Ionization State*)
φ = Ip/27.212; (*Ionization potential in atomic unit*)
ns = z/√(2*φ); (*Effective principle quantum number*)
no = ns;
l = 1; (* Orbital quantum number for Ar for Pz electron*)
m = 0;
ls = no - 1; (*Effective orbital quantum number*)
Cnl = 2^(2*ns) / (ns * (Gamma[ns + ls + 1]) * (Gamma[ns - ls])); (*ADK coefficient*)
Glm = ((2*l+1) * (1 + Abs[m]) !)/((2^Abs[m]) * Abs[m] ! * (1 - Abs[m]) !); (*ADK coefficient*)
Rc = (Cnl * φ * Glm)/(2.4189 * 10^-2); (*ADK coefficient*)
x = 2 * ns - Abs[m] - 1;
Ft1 = (√(I01 * 2 * 376) * 10^-8)/51.42 * (Exp[-2 * Log[2] * (t/τp)^2] * Cos[ω * t]); (*Electric Field*)

ξ1 = Rc * (2 * (2 * φ)^(3/2) / Abs[Ft1])^x * Exp[- (2 * (2 * φ)^(3/2))/(3 * Abs[Ft1])]; (*Rate of Ionization*)

P1 = 1 - Exp[-NIntegrate[ξ1, {t, -30, α}]]; (*Probability of Ionization*)
Tabledata1 = Table[{α, P1}, {α, -15, 15, 0.01}];
ListPlot[Tabledata1, PlotRange → All]
Tabledata2 = Table[{t, Ft1}, {t, -30, 30, 0.01}];
ListPlot[Tabledata2, PlotRange → All]
Tabledata3 = Table[{t, ξ1}, {t, -20, 20, 0.01}];
ListPlot[Tabledata3, PlotRange → All]
```

Appendix B - ADK Calculation

```
m = 0;
l = 1;
Ip = 15.76 / 27.2 ;
z = 1;
Cλ = 2.586 ;
κ = √(2 * Ip) ;

Q = (-1)^m * √( ((2 * l + 1) * (1 + Abs [m]) !) / (2 * (1 - Abs [m]) !) ) ;

B = Q * Cλ;
Tau = 2.4 * 10 ^ -17 ;
Td = 15 * 10 ^ -15 ; (*sec*)
τ = 7 * 10 ^ -15 ; (*sec*)
Γ = Td / Tau ; (*au*)
τau = τ / Tau ; (*au*)
Et1 =
 √( ( (0.39 * (Exp [-2 * Log [2] * ((t - Γ/2) / τau)^2] + Exp [-2 * Log [2] * ((t + Γ/2) / τau)^2]) ) * Cos [0.056 * t + Pi/2] )^2 +
    ( (0.39 * (Exp [-2 * Log [2] * ((t - Γ/2) / τau)^2] - Exp [-2 * Log [2] * ((t + Γ/2) / τau)^2]) ) * Sin [0.056 * t + Pi/2] )^2 );

F1 = Abs [Et1] ;

Wsat1 = B^2 / (2^Abs[m] * (Abs [m]) !) * 1 / κ^(2*z/κ -1) * (2 * κ^3 / F1)^(2*z/κ - Abs[m] -1) * Exp [-2 * κ^3 / (3 * F1) ];

W1 = FullSimplify [ Expand [ √(3 * F1 / (π * κ^3)) * Wsat1 ] ];

Tabledata1 = Table [{x, 1 - Exp [-NIntegrate [W1, {t, -1000, x}]]}, {x, -2000, 2000, 0.1}];
Tabledata2 = Table [{t, Et1}, {t, -2000, 2000, 0.1}];
g1 = ListPlot [Tabledata1 , DisplayFunction → Identity , PlotStyle →RGBColor [1, 0, 0]];
g2 = ListPlot [Tabledata2 , DisplayFunction → Identity , PlotStyle →RGBColor [0, 0, 1]];
Show [g1, g2, DisplayFunction → $DisplayFunction ]
```

Appendix C - Calculation of the thickness of fused silica to change CE phase by 2π

$$d\,\varphi_{CE} = \frac{\omega l_0}{c}[n_g - n]$$

$$= \omega l_0 [\frac{n_g}{c} - \frac{n}{c}]$$

$$= \omega l_0 [\frac{1}{v_g} - \frac{n}{c}] = \omega l_0 [\frac{dk}{d\omega} - \frac{n}{c}]$$

$$= \omega l_0 [\frac{n}{c} + \frac{\omega}{c}\frac{dn}{d\omega} - \frac{n}{c}]$$

$$= \frac{\omega^2 l_0}{c}\frac{dn}{d\lambda}\frac{d\lambda}{d\omega} = \frac{\omega^2 l_0}{c} \times \frac{-2\pi d}{\omega^2}\frac{dn}{d\lambda}$$

$$\Rightarrow d\,\varphi_{CE} = -2\pi l_0 \frac{dn}{d\lambda}$$

For 2π phase shift

$$2\pi = -2\pi l_0 \frac{dn}{d\lambda}$$

We know from Sellmeier Equation,

$$\frac{dn}{d\lambda} = 0.01729$$

$$\Rightarrow l_0 = 58\,\mu m$$

Appendix D - Kansas Light Source Laser System
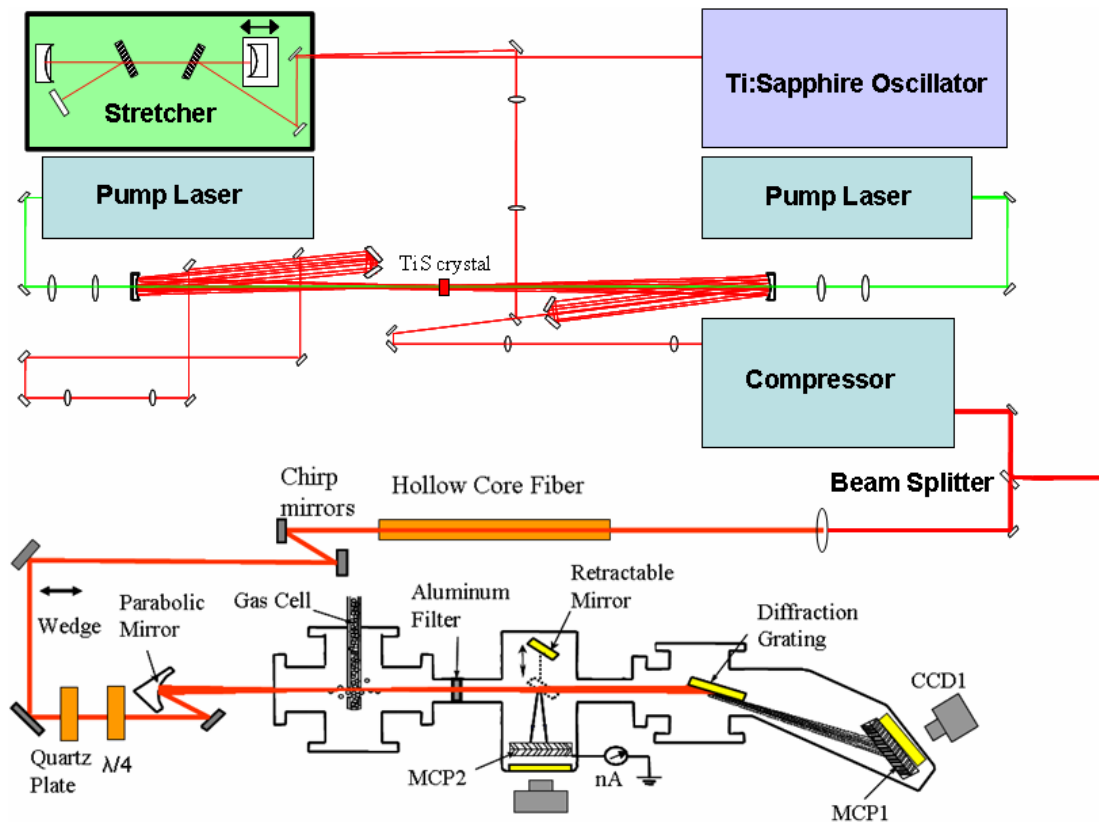
Fig. B1.Schematics of KLS laser Ti:Sapphire laser system.and XUV spectrometer.

KLS Ti:sapphire laser system consist of a mode-locked oscillator and single stage multi-pass chirped-pulse amplification. 2.6 nJ, 12fs and ~77MHz is generated from the oscillator by pumping with 4W and 532nm continuous wave laser. Pokel's cell is used to convert 77 MHz into a 1 kHz. It is then stretched temporally to 80 ps by a pair of gratings. The stretched pulses are subsequently amplified by a single stage 14 passes through a Ti: sapphire crystal cooled by liquid nitrogen. The amplifier is pumped by ~30 W of doubled Nd:YLF laser 532-nm radiation

pulsed at 1kHz. Amplified spontaneous emission (ASE) is reduced by adjusting the focal volume and using Pokel-cell after seven pass. Amplified pulses are recompressed temporally to 25fs by using a negative dispersion grating pair. The compressed short pulse has energy 2.5 mJ at a repetition rate 1 kHz.

Appendix E - Time of Flight (TOF) Spectrometer

Time of flight (TOF) has recently been designed in order to estimate and measure the pulse duration of the laser electric field during the experiment. The method of measurement is very easy, quick and straight forward. Since, high harmonics spectrum and hence experiments associated with the high harmonics depend on the pulse duration of the driving laser field, precision
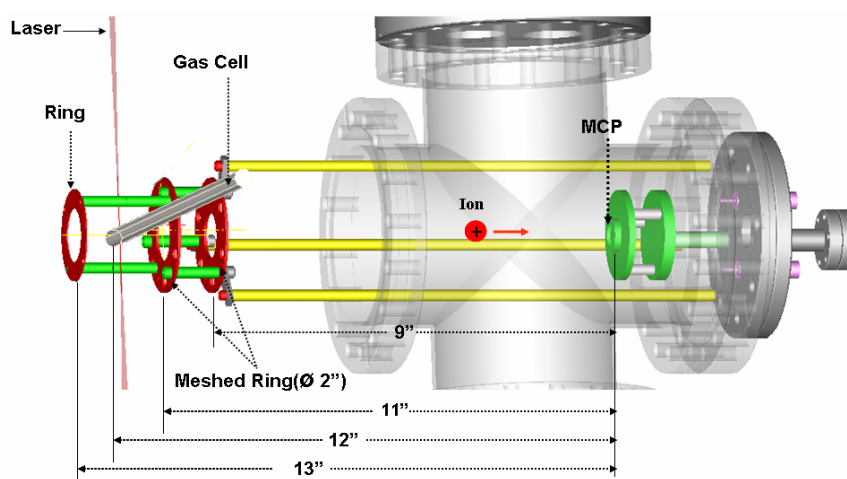
Fig A1 Time of Flight spectrometer design
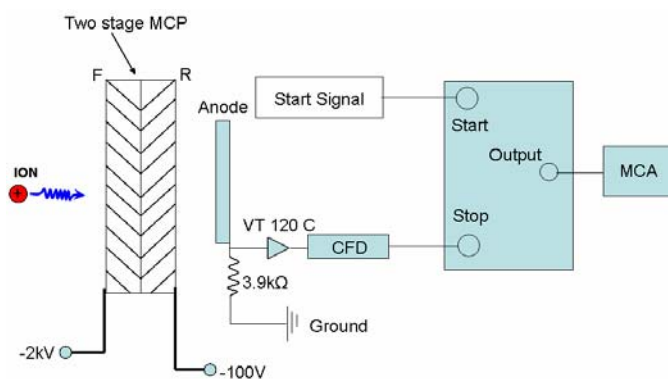
Fig A2 Schematics of Hamamatsu MCP wiring to measure pulse duration of the driving pulses.

of the experimental result requires an estimation of pulse duration in the time of data acquisition. Timely information on the pulse duration is also imperative to use the data in making critical decision quickly during the time of the experiment. Day to day performance of the laser and its pulse duration is reasonably reproducible in KLS, but shot-to-shot control over its pulse duration is very difficult.

Since, measurement of the pulse duration with the FROG takes much work for the alignment due to its location from our work station; we hope our new approach of introducing TOF spectrometer would eliminate these difficulties by permitting us to estimate pulse duration of the laser in every few hours. Furthermore, it will help us to use the time efficiently during limited access to the beam time schedule in future.

Fig.A1 shows our basic design. The design consists of a couple of 2 inch meshed brass ring with internal diameter 1.7 inch separated 1 inch apart. The first mesh is at 2 inch and the second one is at 3 inch distance from the location of an unmeshed ring of the same I.D and O.D. as the meshed one. The gas cell is located between first meshed and unmeshed ring. Michrochannel plate is located at a distance 13 inch from the unmeshed brass ring. Fig.A2 illustrates the detail of the wiring of Hamamatsu MCP for measuring the pulse duration of the driving field. Front and the back of the two stages MCP is supplied with -2kV and -100 V while anode is grounded. The stop of time to analog converter (TAC) connects output of the constant fraction discriminator (in Fig.A2: CFD). Input of CFD connects to the amplifier VT120c which
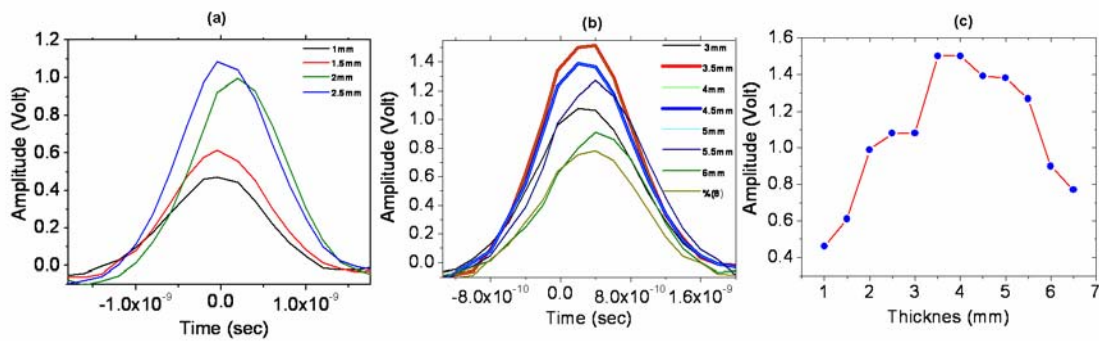
Fig.A3. Amplitude as a function of time when when fused silica thickness is varied from (a) 1mm to 2.5mm (b) 3mm to 6.5 mm (c) the plot of amplitude as a function of fused silica thickness.

amplifies the signal coming from the anode connected to its input. Start signal is the signal from the Pokels cell which sends 1000 pulses per sec synchronized with the laser pulses. Eventually the timing difference is monitored in multiple channel analyzers (MCA). Observed increase in intensity at target due to shortening of the pulse duration when compensating plates of different thickness were adjusted is shown in the Fig. A3. Shortest pulse duration was observed when the thickness reached 3.5 mm at which signal was observed highest.

Appendix F - Simion Geometry File

```
;================================================================================
=
; SIMION geometry file for the simulation of the TOF experiment in Laser Room of JRML.
;      Version 2.0                    25th July 2007,KSU
;                       Mahendra Shakya
;================================================================================
;
pa_define(56,56,200,p,n,e,100)

;
locate(0,0,0,1,0,0,0)
   {
   e(1)
     {
     fill
      {
       within
         {cylinder(28,28,10,25,25,1)}
                      Notin
                        {cylinder(28,28,10,15,15,1)}
      }
     }
   }
;
locate(0,0,0,1,0,0,0)
   {
   e(2)
     {
     fill
      {
       within
         {cylinder(28,28,61,20,20,0)}

      }
     }
   }
;
locate(0,0,0,1,0,0,0)
   {
   e(3)
```

```
       {
      fill
       {
       within
         {cylinder(28,28,89,20,20,0)}


       }
       }
      }
;
locate(0,0,0,1,0,0,0)
    {
     e(4)
       {
      fill
       {
       within
         {cylinder(28,28,199,5,5,4)}


       }
       }
      }
;
Locate(7,28,61,1,10,0,0)
    {
     e(0)
       {
      fill
        {
Locate(0,0,0,1,45,0,0)
  {
      within
        {cylinder(0,0,0,5,5,2)}
       }


      }
      }
     }
```
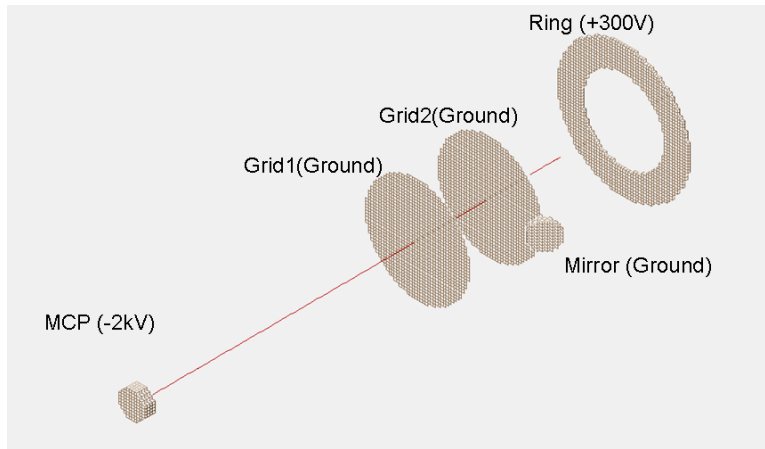
Fig.A4. Ion trace (red line) observed in Simion program when mirror and grids grounded and ring was set to +300V.